Development of semi-automated steady state exogenous contrast cerebral blood volume mapping

Frank Anthony Provenzano

Submitted in partial fulfillment of the
requirements for the degree of
Doctor of Philosophy
in the Graduate School of Arts and Sciences

COLUMBIA UNIVERSITY

2016

ABSTRACT

Development of semi-automated steady state exogenous contrast cerebral blood volume mapping

Frank Anthony Provenzano

Functional magnetic resonance imaging (fMRI) as it exists, in its many forms and variants, has revolutionized the fields of neurology and psychology by revealing functional differences non-invasively. Although blood oxygenation level dependent (BOLD) fMRI is used interchangeably with fMRI, it measures one single difference in a physiological measurement using a set sequence. As such, there are other established changes in the brain that relate to blood movement and capacity that can also be measured using MRI. One measure, exogenous steady state cerebral blood volume, uses a bolus routine contrast agent administered intravenously alongside a pair of high resolution 'structural-like' MRI images to provide detailed information within small cortical and subcortical structures.

In this thesis I design a semi-automated algorithm to generate maps of steady state exogenous cerebral blood volume magnetic resonance imaging datasets. To do this I developed an algorithm and tested it on existing MRI scanning protocols. A series of automated pre-processing steps are developed and tested, including automated scan flagging for artifacts and requisite vascular segmentation. Then, a methodology is developed to create cerebral blood volume (CBV) region of interest (ROI) masks

that can then be applied on an existing database to test known CBV dysfunction in a group of patients at high risk for psychosis. Finally, we develop an experiment to see if template based cerebral blood alterations co-registered with class segmentation maps have any positive predictive value in determining disease state in a well characterized cohort of five age-matched groups in an Alzheimer's disease neuroimaging study.

Contents

List Of Figures vi

List Of Tables xxi

List of Abbreviations xxii

Acknowledgements xxv

1 Introduction **1**

1.1 Motivations 1

1.2 Specific aims 8

1.2.1 Specific aim 1: Develop software to generate CBV images with *a priori* anatomic segmentations 9

1.2.2 Specific Aim 2: Using extant literature and findings support CBV findings by examining hippocampal dysfunction in schizophrenia 10

1.2.3 Specific aim 3: Use *a priori* CBV maps in template space and determine whether functional imaging changes in small areas of the hippocampus are predictive of structural changes as measured by standard MRI sequences 11

1.3 Innovation 12
1.4 Background 12
1.4.1 CBV fMRI and Metabolism 12
1.4.2 Statistical analysis and template atlas generation 15
1.4.3 Semi-automated analysis and error-metrics 16
1.4.4 Parameterization and delineation of template ROIs in suspect groups 18

2 Specific Aim 1: Cerebral Blood Volume Toolkit Development 19

2.1 Examine pre and post contrast MRI images for uptake and processability 19
2.1.1 Introduction and study design 19
2.1.2 Methods 25
2.1.3 Results 27
2.1.4 Conclusion 30
2.2 Identify region of pure blood in the superior sagittal sinus 30
2.2.1 Introduction and study design 30
2.2.2 Methods 31
2.2.3 Results 38
2.2.4 Conclusions 40
2.3 Identification and elimation of epicortical vessels in ROI analysis . . . 40
2.3.1 Introduction and study design 40
2.3.2 Methods 41
2.3.3 Results 43

2.3.4 Conclusions 43
2.4 Examination of the effects of bias field 45
2.4.1 Introduction and study design 45
2.4.2 Methods 45
2.4.3 Results 47
2.4.4 Conclusion 48

3 Apply CBV techniques on high-risk for conversion to psychosis dataset 51

3.1 Create a broad based population template onto which we can isolate and identify anatomical and canonical defined regions 51
3.1.1 Introduction and study design 51
3.1.2 Methods 53
3.1.3 Results 54
3.1.4 Conclusions 55
3.2 Test forward application and accuracy of template to functional CBV images 55
3.2.1 Introduction and study design 55
3.2.2 Methods 57
3.3 Demonstrate CBV changes in humans in a new prodromal psychosis population with forward application of CBV ROI 58
3.3.1 Introduction and study design 58
3.3.2 Methods 59
3.3.3 Results 60

3.3.4 Conclusions 61

4 Examining utlility of functionally derived results on structural images 63

4.1 Examine CBV and volume in Alzheimer's disease 63

4.1.1 Introduction and study design 63

4.1.2 Methods 67

4.1.3 Results 68

4.1.4 Conclusion 69

4.2 Test the postitive predictive value of forward-applied functionally derived metabolic atlases in early-stage structural MRI disease states . 74

4.2.1 Introduction and study design 74

4.2.2 Methods 74

4.2.3 Results 75

4.2.4 Conclusion 75

5 Discussion and conclusion 76

5.1 Discussion 76

5.1.1 Specific Aim 1 76

5.1.2 Specific Aim 2 78

5.1.3 Specific Aim 3 79

5.2 Conclusion 80

Bibliography 82

Appendix **92**

Appendix A: Determination of vascular thresholding **103**

A.1 Background 103

A.2 Methods 105

A.3 Results 106

A.4 Conclusion 107

Appendix B: Evaluation of SSS segmentation to manual segmentation **109**

B.1 Methods 109

B.2 Results 112

B.3 Conclusion 112

List of Figures

1-1 This figure shows an example of a neuron's relationship to blood supply. Although neurons do not continue to develop in adulthood (with the exception of the dentate gyrus, olfactory bulb and the subventricular zone[43]), there is synaptic and angiogenic reorganization that occurs during the aging process.[32] 2

1-2 A graphic representation and interpretation of Angelo Mosso's 'First' Neuroimaging experiment. A farmer named Michele Bertino had experienced a skull injury, exposing his cerebrum under the skull. Dr. Mosso attached a sensor that compressed a cylinder upon measurable cerebral pulsatile changes. Additionally, a sensor was placed on the forearm to act as a control. (left) Several experiments were performed (right) while the awake patient was connected to the apparatus (a), including a resting experiment demonstrating resting state pulsatility(top), the subject hearing church bells (*) and the patient being asked to perform a calculation of two numbers (**) and providing a response (***). Although this experiment is thought to have captured an analog of CBF, the change in pulsatility can be considered to be a change in intra-session cerebral blood volume[60] 3

1-3 This figure reflects the neuropathology revealed by the Braak's in Alzheimer's disease staging.[9] Starting at stage I, one can see pathology that begins with isolated NFT in the pre-α layer the trans entorhinal cortex of the medial temporal lobe. MTL volume loss is known to occur in late stage diseases, less so in preclinical stages. A tool with resolution able to interrogate submillimeter resolution may be able to detect these histology changes as metabolic signatures prior to volume changes. 6

1-4 Flowchart of specific aims 8

1-5 CBV findings in preclinical Alzheimer's disease as shown by Khan et al.[44] 10

1-6 A diagram coupling neurovascular activity, metabolites, oxygen blood flow and volume[52] 14

1-7 A diagram showing joined CBV maps used to generate CBV values for voxel level analysis 16

1-8 A schematic representation of how anatomically based CBV images can be used for direct statistical analyses. The left pane represents n subject images that get co-registered into a standard space of continuous values, middle, which are then used to generate voxel by voxel statistics. Since there are no time series or other corrections in place besides the initial template co-registration, any result, right, is based only on the raw subtracted and normalized signal value. 17

2-1 A diagram showing CBV analytic stream to generate both canonical region of interest analyses as well as voxel based analysis. Since the method of CBV generation outlied uses a pair of anisometric gradient echo images, we can use either unbiased voxel by voxel statistical measures or identify a canonical or archetypical region and co-register that region with a greated degree of certainy and fewer partial voluming effects than if it were a lower resolution EPI fMRI study or other functional image. 20

2-2 Simulated TR values for tissue classes alongside GBCA injection . . . 21

2-3 (Two variations of chelated gadolinium contrast agent. Chelation is a process by which elemental or ionic gadolinium is bound to an inert substance that remains in the vasculature without passing the blood brain barrier of a healthy individual and is eventually excreted. (a) shows gadodiamide marketed as *Omniscan* and (b) shows Gadobutrol marketed as *Gadovist* 22

2-4 Instance of contrast enhanced signal change mapped on orthogonal projections of the brain[7] 23

2-5 Levenberg-Marquart concentration time curve of the change in ΔR2 ($\propto 1/\Delta$T2)as a function of bolus detection of GBCA injection. Both β and K are inherent functions of the curve fitting procedure, T_a is the time at which the bolus is injected and 't' is the time.[50] 23

2-6 Comparison of exogenous, at multiple injection doses, and endogenous contrast agents in both gradient and spin echo MR sequences. Note ordinate is log-transformed.[66] 24

2-7 Non-zero histogram distribution for tissue classes using a standard class segmentation protocol.[2] 27

2-8 A dual histogram analysis panel: The top panel refers to non-zero histogram bins of 100 for the pre-contrast image in red and the post contrast image in blue. The lower panel refers to the subtracted histogram difference. 28

2-9 A set of four pairs of dual histogram analysis panels. TL, TR, BL all refer to patients who have had adequate contrast uptake an little movement. BR shows a patient with poor contrast uptake (often when the administration of i.v. GBCA bolus of GBCA does not enter the venous system). The bottom histogram difference can be seen to be reversed, whereas the previous bimodal distributions are clearly - and +, the bottom is reversed. Sometimes, if not revered, the fit is below a particular R^2 value when the function is minimized. 29

2-10 A modified 2-degree gaussian distribution 29

2-11 Sample time of flight (TOF) MRA with a 1.5 T MRI field strength acquisition (a) and a 3.0 T MRI field strength acquisition. [1] 32

2-12 Form of the Hessian matrix 32

2-13 Ratio component for the blob likelihood. 32

2-14 Ratio component for structures that range from flat circle to line structures. 33

2-15 The 'structureness' component 33

2-16 All components joined together to produce final grayscale invariant vesselness equation. 33

2-17 A sample image shown in A upon which an edge detection B is performed and a "Ridge" detection is performed. One can see the identifiable areas in the edge detection bound the area contained between those points, adding to difficulty for a multiple voxel boundary, or in the event an edge contains features between the abutting areas. A "Ridge" detection in C isolates the local points of infection by discretizing and modeling as a 2^{nd} degree polynomial, identifying only areas of inflection, making it ideal for vessels larger than two voxels length. . . 33

2-18 The raw vesselness map generated from a random subject's post gadolinium scan. TL is oblique coronal to the long axis of the hippocampus, TR is sagittal anisotropic and BL is axial anisotropic. One can make out several structures including the bulk of bilateral hemispheric WM. We are only interested in the isolated region located medial and superior to both of those regions. 35

2-19 The same vesselness map in 2-18 with a connected component algorithm applied with false color. Each color reflects a masked region of contiguous voxels in n-dimensional space. The area we wish to identify is indicated with an arrow. 36

2-20 Here, a n-dimensional image (where n=2), img is eroded with structuring element b. For our analyses, kernels were cubic 3x3x3. 36

2-21 Here we wish to determine a vessel value from $\hat{z}$, from the total connected components V $\in k$, as a function of the existing atlas mask, A, and voxels in a potential mask. 36

2-22 Eigenvalue shape descriptions based on the hessian matrix of a sphere (or 'blob' structure), plate-like and tube-like structure. Tubular structures can be identified by adjusting values of the prescribed eigenvalue amounts 37

2-23 Diagram of how the vesselness atlas is created. Although we have used an aforementioned 3.0T MRI vesselness mask as our primary atlas, this explains the framework for both the creation of new vessel atlas and the application of said atlas to any new image which has had vesselness operated on it. 37

2-24 relative CBV is calculated from tissue, T, in a voxel in the post and pre contrast image divided by the mean value of blood as calculated from the superior sagittal sinus (SSS) in the post and pre contrast images. The denominator for each voxel in the subtracted tissue image is identical. 38

2-25 Vesselness maps with the following characterstics: α=0.05, β=20, c=30. For the scanner on which most of the pre and post contrast MRI pairs have been acquired, these are the values which have been shown to be most useful in generating reliable SSS extraction maps. 38

2-26 Rendering of an averaged and thresholded joint magnetic resonance angiography from a sample of co-registered vesselness maps. Note the clearly defined superior sagittal sinus on the top of the image as well as other 39

2-27 Anatomical representation of the main cavernous outflow (shown with a texture) and inflow (shown with a bold line) within the vasculature of the brain. 40

2-28 Sample MTL section of a non-brain extracted subtracted image (TL) The subtracted image. Outlined expanded below in BL. (TM) Freesurfer cortical segmentation mask (where each color represents a unique different region) overlaid onto the co-registered subtracted image. Some vasculature revealed by the subtracted image is present in the masked labels, however much is still claimed as regions since most GRE sequences Freesurfer suggests and for which it is optimized do not have any sort of vascular delineation. Outlined expanded below in BM. (TR) This section represents the cortical mask (CM) excluding any voxels which fall outside of the GMM in the vessel mask (VM) (*i.e.* CM $\wedge \neg$VM). Outlined expanded below in BL. 42

2-29 The collection of scripts are shown in the final CBV program container, written for Matlab. This program requires the input of a structural T1 weighted image and a pair of pre and post contrast gadolinium images and will generate all necessary images for ROI or VBA analysis. . . . 44

2-30 An example of bias field artifacts are shown here. Note the upper left corner of the top figure, and the left side of the bottom figure. One can easily see the dampening in signal intensity that can be potentially problematic in both clinical and research uses. 46

2-31 Artifactual errors seen due to high signal in the eye, indicative of a PE artifact in the left-right direction. It is possible that non-visible artifacts may artificially dampen or increase signal elsewhere parallel to the plane of the PE direction, and as such, represents an image that would most likely be excluded from CBV analysis.[61] 47

2-32 This image represents orthogonal views of the bias fields generated from both the post contrast image and the pre contrast image. The brain has been extracted prior to both of these analyses.[103] (a,b,c) Sagittal, coronal and axial view of the post-contrast image bias field maps and the (d,e,f) pre-contrast image field maps. 49

2-33 Brain extracted CBV image is shown in three orthogonal planes. The marked brightness occurs in regions with large macrovasculature. . . 50

2-34 The subtracted bias field image (of *post* - *pre*) is shown overlaid with a 60% opacity on a subtracted image 50

3-1 An example of disease progression as a function of impairment on the cellular level in schizophrenia[83] 53

3-2 An example of a functional template brain and the region of interest we wish to test, specifically the left anterior CA1 of the hippocampus 54

3-3 Drawing of the hippocampus as edited from Santiago Ramon y Cajal which delineates subregions[73] 57

3-4 Findings from a paper which used a manual/per slice region of interest analysis [17] 60

3-5 Preliminary results from CBV ROI study. Independent samples t-test is significant at p<0.005 not assuming equal variances. 61

3-6 (Left anterior (a) dentate gyrus (b) CA3 and (c) subiculum mean CBV value in a group of controls and age-matched patients at high risk for psychosis. Independent samples t-test is not significant at p<0.05 not assuming equal variances. 62

4-1 Established athologies in AD along with the biomarkers that can be used to discriminate between the various blood, neuropsych and imaging markers.[18] 64

4-2 VBM analysis of age-matched controls and AD patients in the ADNI dataset. Voxel-level significance at p<0.001 reveals several clusters, many of which pass cluster level significance statistical threshold. . . 65

4-3 VBM analysis of age-matched controls and controls who convert to AD within 36 months in the ADNI dataset. Voxel-level significance at p<0.001 reveals one small cluster that does not pass cluster-level significance. 66

4-4 Shown in white is a sample gray matter segmented image co-registered to template space. The red arrows point to ares of red that reflect the thresholded binarized mask co-registered to the space of the image. . 69

4-5 Gray matter volume in the MTRC in the five age-matched ADNI groups. One way ANOVA and pair-wise students t-test are not significant at p<0.05. 70

4-6 Linear regression of five age-matched ADNI groups in increasing order of potential clinical risk. 1) Healthy Controls 2) Healthy Controls who convert to AD within 3 years 3) MCI who do not convert to AD in 3 years 4) MCI who do convert to AD within 3 years 5) AD. R^2=0.017, F=2.8, p<0.096 71

4-7 The entorhinal cortex volume (in mm^3 of five groups of subjects in the ADNI study. All subject groups were age matched. *** indicates two-tailed t-test significance. For the HC compared to AD, t=6.467 p<0.001, for the HC compared to MCI who convert to AD, t=4.067 p<0.001. The demographic and population information are in 6-9 . . 72

4-8 Left pane reflects predicted EC CBV value differences in preclinical AD compared to healthy controls whereas right pane reflects predicted EC volume differences in the same group 73

4-9 An example of a expected variance for age in a specific age group with CBV, taken from studies related to hippocampal volume changes[10] . 75

5-1 The addressed specific aims of this project. The first two aims were executed successfully, since the toolkit has been able to semi-automate the development of exogenous steady state cerebral blood volume maps, and we were able to show dysfunction specific and sensitive the region previously shown to exhibit dysfunction in patients who progress to psychosis. The applied CBV region, however, did not have a higher positive predictive value than a known area of dysfunction in diagnosis or predicting disease states. 77

6-1 The demographics of the prodromal psychosis data-set. 93

6-2 Vesselness maps with the following characterstics: α=0.2, β=20, c=30 94

6-3 Vesselness maps with the following characterstics: α=0.05, β=50, c=30 94

6-4 Vesselness maps with the following characterstics: α=0.05, β=50, c=1 95

6-5 Vesselness maps with the following characterstics: α=0.2, β=20, c=100 95

6-6 Vesselness maps with the following characterstics: α=0.01, β=20, c=30 96

6-7 Vesselness maps with the following characterstics: α=0.01, β=1, c=30 96

6-8 ADNI study demographics. 97

6-9 ADNI study demographics. 98

6-10 Pulse sequence diagram of an rf spoiled gradient echo image, as is used in the antecedent pre and post contrast MRI images. The top line reflects the rf pulse from the magnet, that both applies the prepulse and alternating phased pulses to cancel transverse magnetizations. 'Gs' reflects the slice lobe, 'Gr' reflects the read lobe, 'Gp' the phase lobe and 'Signal' contains just that. Gradient spoiling can occur by means of either just the 'Gs' or with the 'Gr' applying a varying, sometimes random pulse. 99

6-11 This shows how we derive functional ROI from voxel based approaches. To do this we generate CBV results on a template brain which is derived from pre-contrast T1 weighted images. These images contain adequate structural data for diffeomorphic co-registration algorithms to co-register smaller features than EPI sequences. We binarize (i.e. threshold the resultant map at the t or f level of significance) the mask at the lowest statistical level and save that separate from the generated template 100

6-12 For a new patient to be analyzed, we acquire a new patient scan (isometric/isotropic structural T1 weighted image) and segment that into tissue classes. The middle panel shows the joined GM and WM tissue class segmentations joined (in red and yellow, respectively) and separated into grey and white, respectively, in the next two panes. The GM mask is then co-registered into the template space in which the statistical binarized mask. This uses the structural T1 image as the basis for transformation and applies that forward transformation to the GM mask. 101

6-13 The intersection of the binarized mask and the gray matter mask is calculated. Although voxel size differences may occur, all images being in the same space indicate that all measures of volume are standardized by co-registering. 102

A-1 This is an example of an image displaying the PV problems and window sampling limitations in both non and contrast enhanced MRI. The fraction of an isotropic pixel (or voxel) of size k will capture at most $.25\pi$ or approximately 78 percent of a 2 or 3 dimensional vessel space, assuming the path of the vessel is orthogonal to the plane of the voxel. 104

A-2 Shown is a coronal slice. The left hippocampus is indicated by a blue "x" and the venous system is indicated by a red "+". Voxels were chosen in one slice near the middle of the hippocampal formation. 105

A-3 Here, s is the coefficient that measures overlap between manually labeled tissue, X_l and tissue preserved (not masked) during masking, X_{nm} 106

A-4 Here is a histogram of 12 subject's CBV mean values. The mean and variance of these CBV values are within physiological limits, and can be used as a *post-hoc* exclusionary criteria for subjects that might have intravascular abnormalities or BBB breakage. 108

B-1 This is an orthogonal section of a subtracted subject scan showing the venous structure elucidated from injection of a GBCA compared to the non-contrast image. 110

B-2 This image shows a representative coronal slice onto which four voxels within the SSS have their intensities measured and the mean calculated. 111

B-3 Here is the distributions of voxel values from both the standard vessel extracted mean value (from the top 10% of vessel voxel values) and the mean of four independently chosen brightest voxel values in the coronal plane of an anterior slice of several images derived from subtracting pre-contrast MRI scans from post-contrast MRI scans. The ordinate is arbitrary MRI units, and the abcissa is different subjects. The mean of the four values as well as lines indicating standard deviation are reflected with blue circles, and the standard vessel extracted in red squares. 113

List of Tables

6.1 T1 relaxation values of known tissue types 92

6.2 Eigenvalue shape characteristics in three dimensions based on the 1^{st}, 2^{nd} and 3^{rd} eigenvalues[27] 93

6.3 Voxel and cluster based results from VBM analysis 93

A.1 Overlap ratios for several subjects manually chosen values. 106

B.1 Table of individual voxel values and mean segmented voxel values . . 113

List of Abbreviations

Aβ Beta-amyloid

AD Alzheimer's Disease

AIF Arterial Input Function

AUC Area under curve

BBB blood brain barrier

BF Bias Field

BOLD Blood Oxygen Level Dependent

BVR Basal vein of Rosenthal

CBF Cerebral Blood Flow

CBV Cerebral Blood Volume

$CMRO_2$ Cerebral Metabolic rate of oxygen

DCE Dynamic Contrast Enhancement

DeOHb Deoxyhemoglobin

EPI Echo Planar Imaging

FFE Fast Field Echo

FLAIR Fluid-attenuated inversion recovery

GBCA Gadolinium Based Contrast Agent

GM Gray Matter

GMM Gaussian Mixture Model

GRE Gradient echo

Hb Hemoglobin

HC Healthy controls

ICV Intracranial volume

ICVe Internal cerebral vein

INFss Inferior sagittal sinus

MCI Mild cognitive impairment

MPRAGE Magnetization prepared rapid acquisition gradient echo

MRI Magnetic Resonance Imaging

MTRC Medial Transrhinal Cortex

nf Neurofibrillary Tangles

PET Positron Emission Tomography

PiB Pittsburgh Compound-B

ROI Region of Interest

SNR Signal to Noise Ratio

SPGR Spoiled Gradient Echo

SSi Straight Sinus

ss Steady State

ssCBV Steady State Cerebral Blood Volume

T1 Spin-lattice relaxation time

T2 Spin-spin relaxation time

T2* T2* decay

TR Repetition Time

VASO Vascular Space Occupancy

VBA Voxel Based Analysis

VBM Voxel Based Morphometry

WM White Matter

WMH White Matter Hyperintensities

Acknowledgments

I am proud to call myself a Columbia "Townie", and have fostered relationships with wonderful friends and colleagues for over nine years as a result. I have nothing but gratitude for the projects that I have been privileged to work on. I am also honored to be part of the continuing relationship between both Biomedical Engineering and Neurology.

I would first like to thank Mr. Walter Muller, Drs. Andreas Hielscher, Masanori Ichise, Ronald Tikofsky and Cigdem Akman for providing me guidance in the beginning of my research career.

From there I meandered without direction, but like a hydrogen nuclei in $\mathbf{B_0}$ after a $\frac{\pi}{2}$ pulse has been applied, I eventually precesssed and found myself once again aligned with Columbia University, this time working with Dr. Adam Brickman. Adam's friendship, guidance, character, humor and candor is one of the main reasons why I continue to call Columbia a home, and the university is richer for having him. I am also thankful to have had Irene Meier as a friend and bounce-of-ideas-off-of for helping me keep my head above water and listening to her stories of international intrigue, gossip and microbleeds.

The office of CTV has been quite helpful in my career, specifically Donna See, Cindy Lang and Jerry Kokoshka, who have personally guided me in the legal and patent underpinnings that could potentially allow me to apply what I've written and tested on patients whom may directly benefit.

I have had the privilege to know several talented and brilliant students in BME with whom I have had fruitful discussions, including Gesthimani Samiotaki, and Jordan Muraskin, who was instrumental in helping me with various code, projects and other endeavors.

I am thankful for the members of my BME lab, specifically Dr. Yrjo Hame, Guillaume David, Dr. Elsa Angelini, Dr. Jack Po, and Viktor Gamarnik, with all of whom I have had fruitful, interesting, weird or otherwise enriching discussions.

I am also thankful for members of the Small lab, specifically Andrea Urban, Jia Guo, Usman Khan, Xinyang Feng and especially Hannah Sigmon, who has been able to decode my unique brand of cursing, unix commands and hand gestures as decipherable medical image analysis instructions.

I would also like to thank the members of my dissertation committee, Drs. Paul Sajda and Elisa Konofagou, whom I have known since my undergraduate years, for their advice, support and input into this project.

Dr. Ray Razlighi has also been an essential source of information over the years, and has helped me understand larger problems as an engineer would, which is how all problems should be approached, honestly. Additionally, he has a small sectional couch in his office.

I want to extend a heartfelt thanks to Dr. Andrew Laine for not only sponsoring, guiding and mentoring this thesis, but for the continued honest advice he has had for me in my career not just as a PhD, but in academia and the university.

However, I am incredibly grateful for Dr. Scott Small, who has been a diligent, rigorous and attentive mentor during this thesis. I was only too happy to have spent

the last four years in his lab, and am excited for what future collaborations we may have together.

On a personal note, I wish to thank my friends and family, the Provenzanos, the Gobers and the Hsus, all of whom are frankly a little sick and tired of hearing about the hippocampus. But most of all, I would like to thank my loving wife Sarah and our dog Max who have been with me through this process, and are deserving of at least an honorary PhD and Masters, respectively.

Chapter 1

Introduction

1.1 Motivations

Historically, there has always been a significant chasm between the detection of brain function as measured in vivo, and disease state. Some early experiments set the framework for the detection of *in vivo* cerebral function, looking at both human and canine models in an attempt to couple observed increased neuronal "activity" with an observable and detectable change. [35, 77, 60] The underlying principle that governs this relationship is referred to as "neurovascular coupling". This idea states that the metabolic need of neurons is coupled to the flow and volume of blood. Although modern testing paradigms seek to exploit this relationship to detect dynamic changes (e.g. resting for 30 seconds followed by looking at faces for 30 seconds [42]), one may extend the temporal frame to look at changes on the order of months or years, as one would see with slow progressing neurodegenerative diseases. Figure 1-1 demonstrates this relationship on the capillary level.

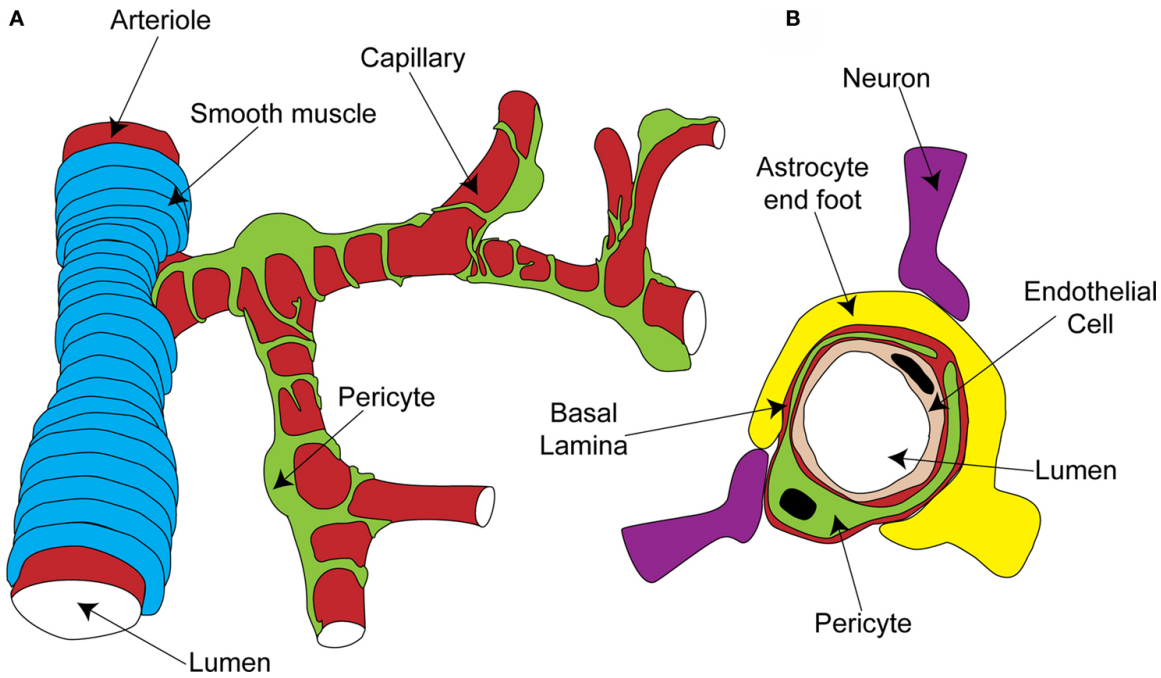

Figure 1-1: This figure shows an example of a neuron's relationship to blood supply. Although neurons do not continue to develop in adulthood (with the exception of the dentate gyrus, olfactory bulb and the subventricular zone[43]), there is synaptic and angiogenic reorganization that occurs during the aging process.[32]

Magnetic Resonance Imaging (MRI) provides a relatively safe and non-invasive measurement technique exploiting the physical properties of different tissues, while providing high spatial resolution and not subjecting a subject to radiation like computed tomography (CT) or positron emission tomography (PET). Additionally, newer technologies permit for increasingly better temporal and spatial scanning and a variety of pulse sequences to provide greater information to distinguish between tissue types [62]. There are several variants of fMRI, including Blood oxygenation level dependent fMRI (BOLD), while the most recognized variation of fMRI, suffers from relatively poor spatial resolution compared to structural MRI.[64]

One reason to do MRI in patients with neurological conditions is established as a tennet of modern neurology training.[8] A set of pulse sequences to determine struc-

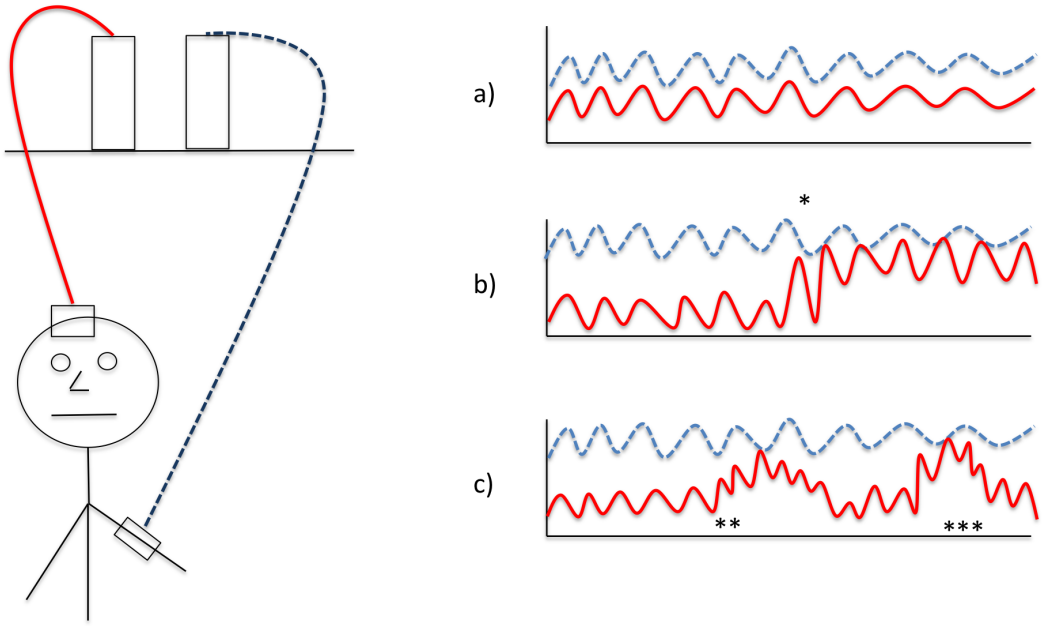

Figure 1-2: A graphic representation and interpretation of Angelo Mosso's 'First' Neuroimaging experiment. A farmer named Michele Bertino had experienced a skull injury, exposing his cerebrum under the skull. Dr. Mosso attached a sensor that compressed a cylinder upon measurable cerebral pulsatile changes. Additionally, a sensor was placed on the forearm to act as a control. (left) Several experiments were performed (right) while the awake patient was connected to the apparatus (a), including a resting experiment demonstrating resting state pulsatility(top), the subject hearing church bells (*) and the patient being asked to perform a calculation of two numbers (**) and providing a response (***). Although this experiment is thought to have captured an analog of CBF, the change in pulsatility can be considered to be a change in intra-session cerebral blood volume[60]

tural abnormalities are generally unique a prescribing physician or center, but used to determine specific tissue or vascular findings. For a patient presenting with a small stroke, MRI may be used alongside CT to determine timing of bleeds, or an MRA used to identify large cerebrovasculature aneurysms or malformations. These findings tend to be 'structural' in presentation, in that cell volume or neuronal loss is identified in imaging as measurable atrophy or volume change. Observable variations in brain function, through indirect measures of metabolism or activity, have been associated with dysfunction in neurological and psychiatric disorders.[82]

For disease etiologies where the anatomic region impairment is focal and clearly defined within several millimeters of either canonical or anatomical space, steady state exogenous contrast ssCBV offers resolution comparable with structural imaging while revealing a metric (relative CBV) not otherwise resolvable in of either T1, T2, T2* or proton density (PD) weighting.[51, 58] Additionally, ssCBV is an inherently quantitative measurement. Comparatively, BOLD fMRI is, in its practice, not frequently measured in a quantitative analysis due to several limitations relating to sequence parameters and deoxygenation factors, though feasible.[37] Thousands of studies have successfully used fMRI BOLD imaging to demonstrate changes in regions in response to an activation paradigm or from functional connectivity present in resting state scans. However, a significant limitation in doing per-patient analysis is the significance gleaned from group data statistics. Knowing that functional changes are present in many disease states, ssCBV may offer a protocol-insensitive quantitative measurement of brain metabolism.

CBV itself can be measured several ways *in vivo* using imaging measures. Bolus

tracking MRI can measure the AUC and changes in transverse relaxation rate (δR2), vascular space occupancy (VASO) can apply a signal nulling by manipulating sequence inversion times, and CBV can also be indirectly extracted from CBF measures by relating the MTT. Concordance between steady state and dynamic approaches, as well as dynamic and PET approaches have been studied to examine the various effects of reliability and reproducibility.[50, 29]

Predominantly, the most common uses of CBV and other blood based metrics of MRI imaging are applied in determining the extent of both tumor growth and stroke.[21, 76, 98] Since these areas frequently have drastic changes in contrast accumulation and perfusion compared to normal appearing tissue. One of the underlying assumptions of contrast enhanced MRI is the presupposition of an intact BBB—one that is frequently violated in oncologic and infarct cases. A challenge of this modality is the reliable generation of functional CBV maps across scanners and sites. Exogenous steady state CBV has been calculated at a range of scan sites, however the values for CBV vary significantly based on MRI noise or other user required parameters [39, 90, 45]. The hippocampus, which has a volume roughly 4 cc located bilaterally in the medial temporal lobe (MTL), is an area implicated in many diseases.[83] ssCBV amongst subject and control studies have revealed voxel based and regional differences in several neurologic disorders. [44, 80, 83, 84, 90]

Alzheimer's disease is a neurodegenerative disease that afflicts millions of older adults around the world. Roughly one in three seniors will get some form of dementia, and AD accounts for more than 60% of all dementias. AD is characterized by a constellation of changes that occur within the brain of an affected individual.

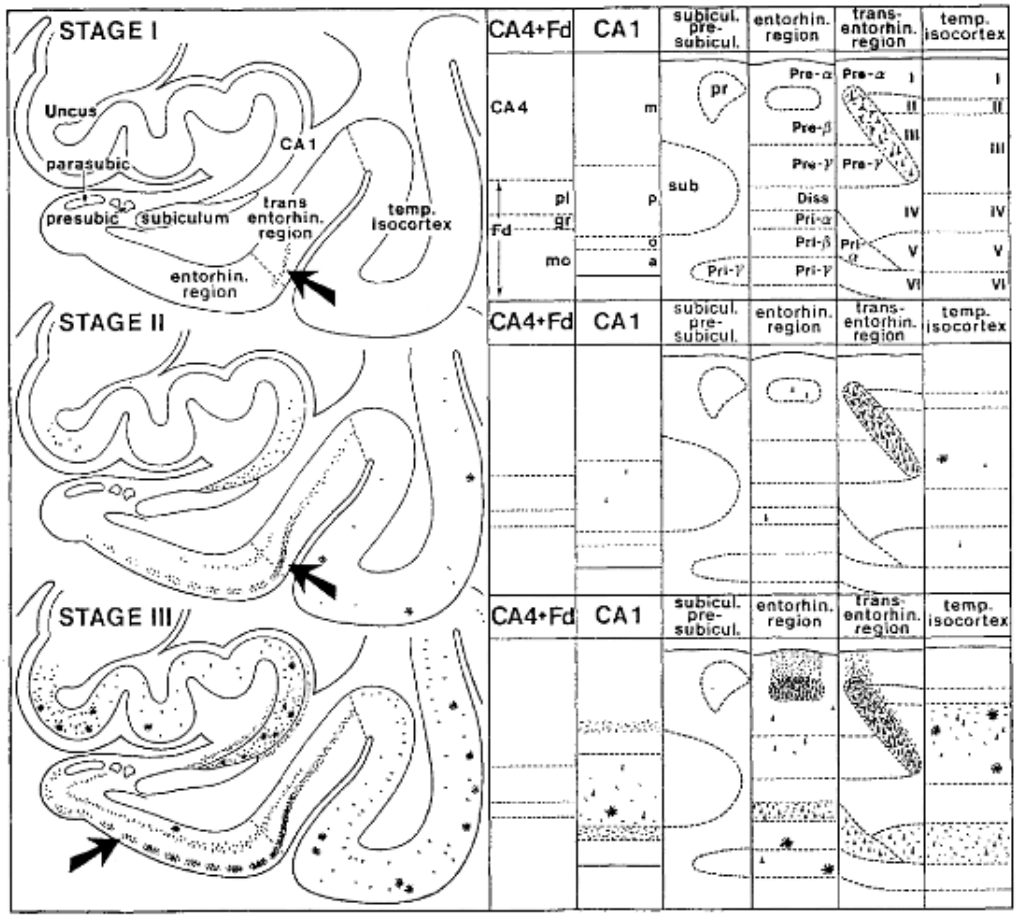

Figure 1-3: This figure reflects the neuropathology revealed by the Braak's in Alzheimer's disease staging.[9] Starting at stage I, one can see pathology that begins with isolated NFT in the pre-α layer the trans entorhinal cortex of the medial temporal lobe. MTL volume loss is known to occur in late stage diseases, less so in preclinical stages. A tool with resolution able to interrogate submillimeter resolution may be able to detect these histology changes as metabolic signatures prior to volume changes.

Two noted neuropathological correlates of AD are deposition of insoluble amyloid and buildups of hyperphosphorylated tau proteins. Figure 1-3 demonstrates one of these changes as seen with NFT staining in the transrhinal region of the EC before any other region has noted changes.[9] The end result of chronic changes is noted atrophy throughout several key areas of the brain, including the cortical mantle as well as the MTL. Some functional imaging studies have focused on ligands that bind to some of these deposits, such as PiB for amyloid deposition, or functional or activation changes in patients with AD. Subtle functional changes may not be detected if the detection sampling size is too large. As such, a method that can reliably interrogate this small area may be of value in early detection of this disease. In addition to neurological disorders, many psychiatric diseases have noted changes with imaging. Schizophrenia is a form of psychosis afflicting 1% of the US adult population. It was classically shown to be a disorder of dopamine, detectable by PET scans targeting dopamine receptor activity in the frontal lobe.[65] However, an amendment to that theory is that glutamate, and glutamanergic dysfunction by means of extracellular glutamate, may also trace and elucidate severity of schizophrenia, specifically the progression into advanced state from an at-risk state.[57] Studies from our and outside labs have found elevated CBV in the CA1 subregion of the hippocampus to indicate dysfunction in schizophrenia patients.[80, 90, 104] The ability to classify and calculate CA1 hippocampal CBV may aid in drug discovery, drug efficacy and potentially earlier diagnosis. The goal of this dissertation is to develop and test a framework for the generation of CBV images using routine scanner sequences, protocols and experimental constructs, as well as to define a system whereby new regions of interest

(ROI) may be applied and adapted for disease assessment and tracking. In addition to particular schizophrenia regions of interest, our lab has also discovered an area of the hippocampal formation, revealed by CBV mapping, which can be helpful in the earliest stages of Alzheimer's disease.[44] This region was defined using a generative group template to which patient MRI images were co-registered and statistical analyses performed.[3, 78] Additionally, we wish to establish criteria for "processability" of images, as well streamline the automated and accurate generation of CBV images for further analytical studies.

1.2 Specific aims

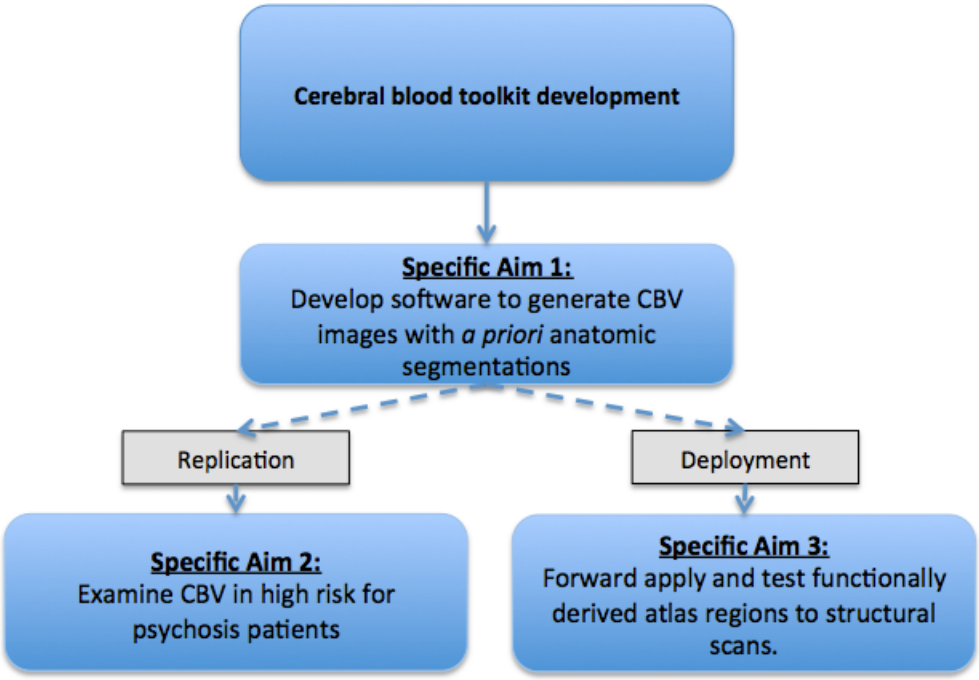

Figure 1-4: Flowchart of specific aims

1.2.1 Specific aim 1: Develop software to generate CBV images with *a priori* anatomic segmentations

For this aim, a software package is to be written that can reliably generate cerebral blood volume maps from routine structural T1 weighted MRI images (TE=3.1, TR=6.7, spoiled gradient echo) acquired prior to and after a bolus injection of a gadolinium based contrast agent (GBCA) [62]. The images need to be converted, organized, and error measures and checks will be written to ensure adequate clinical perfusion and image quality. Analysis of anatomical segmentation would be written into the algorithm, to allow for standard anatomical masks. [25] Systems would be tested and coded to ensure reproducibility. The programming environment would be programmed using Matlab (Mathworks Software, Natick MA USA) programming interface along with new and existing Unix shell software, with a specific goal for repository considerations and eventual software deployment for other users and sites.

The end goal of the software would be not only CBV map generation, but also the organization of the necessary files to allow for group-level analysis (specifically templates for disease and control groups), and the application of parametric results generated from group level analysis such that it can be applied on an individual patient's CBV map in the future. The most common statistical measure of these maps would be mean value of a region or regions in a group template space. [23]

1.2.2 Specific Aim 2: Using extant literature and findings support CBV findings by examining hippocampal dysfunction in schizophrenia

For this aim, we apply the previous method to generate CBV maps, and examine potential metabolic dyshomeostasis as measured using the steady state exogenous contrast CBV. Similar work has been demonstrated by our lab and confirmed by others to be associated with both early and late stage neurologic disease states.[84]Small et al. discussed alterations in the framework of the hippocampus in several disorders, including Alzheimer's disease, schizophrenia, depression and temporal lobe epilepsy, to name a few.

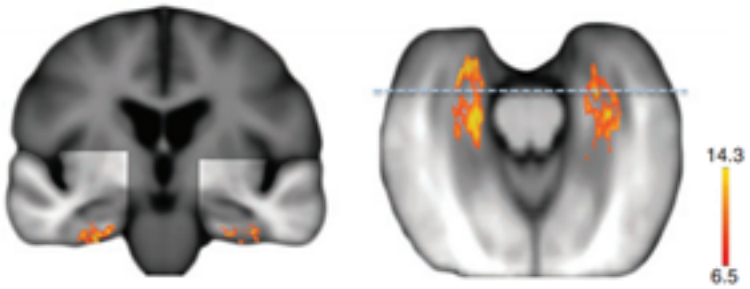

Figure 1-5: CBV findings in preclinical Alzheimer's disease as shown by Khan et al.[44]

Figure 1-5 demonstrates a parametrically defined region of reduced relative CBV within an area of the MTL and hippocampal formation called the entorhinal cortex (EC), specifically the lateral aspect. The CBV maps of these regions were taken from a single scanner over the course of several years, and processed and curated in-house.[19] We would seek to demonstrate a similar finding, concordant with current literature, in an affected region of the brain in a diseased or prodromal state, ideally

in prodromal psychosis and schizophrenia. We wish to apply this method to a new dataset to prove the validity of the CBV maps generated.

1.2.3 Specific aim 3: Use *a priori* CBV maps in template space and determine whether functional imaging changes in small areas of the hippocampus are predictive of structural changes as measured by standard MRI sequences

For this aim, we examine structural MRI images with class segmentation and morphometric techniques to determine if regions identified functionally in groupwise data can have a greater positive predictive value in the structural domain than existing structural image software and methodology.[53, 54] Although structural changes have been clearly identified in patients with advanced disease, evidence shows that functional deficits would be apparent prior to structural change which indicates cellular loss.[83]

Additionally, we want to be able to test the acquisition and processing components of this algorithm at different locations and on different servers, as similar software techniques have done before.[33] Due to the nature of the individual processing components and potential for neuroimaging diagnostics, the ability to accurately and repeatedly get appreciably similar results is crucial. As such, several methods will be examined to see which yields the best results.

1.3 Innovation

The work proposed could potentially be applied to aid in the diagnosis of neurologic and psychiatric disorders. MRI post-processing techniques have been used to chart hippocampal volume changes in the ageing brain, a known biomarker of dementia risk. The software, Neuroquant, uses a proprietary version of a cortical and subcortical segmentation algorithm based on a widely used toolkit (Freesurfer) to measure hippocampal volume.[63, 75] It provides healthy established ranges of hippocampal volume, as shown in Figure **??**, for known age and gender matched groups and has a published rate of error. Our software may provide a range of regional CBV values in control and subject groups. We wish to establish the reproducability of our work across different magnets and different sites. A framework for such a multi-site system has been used with MR imaging with the Alzheimer's Disease Neuroimaging Initiative (ADNI) and their scanning procedures.[97] Ideally, a user would be able to process locally or accurately 'push' their scans to a DICOM repository or process locally. Reports would be generated similar to existing post-processing MRI techniques.[36, 48]

1.4 Background

1.4.1 CBV fMRI and Metabolism

Physiologists and radiologists may have different fundamental ideas regarding the definition of "Metabolic" in the field of imaging. [1] It can either refer to activity-based

[1] Although many modalities claim to perform metabolic imaging, it is often based on a previous direct coupling. For instance, PET imaging is not "glucose metabolism" but rather the direct measure

or longitudinal changes in tissue energy consumption, although unless one refers to imaging of the functional component of energy in mammalian cells, ATP to ADP, usually the measured changes in vivo are from changes in the earlier stages of energy metabolism. FDG-PET measures glucose uptake through a radionuclide, fMRI BOLD measures changes of magnetic susceptibility of the oxygen carrying species, Hb and DeoxyHB, and CBV measures the signal of contrast agent only in areas of actively perfused blood[96]. When discussing changes measured in CBV, our method focuses explicitly on the steady state equilibrium found by measuring the value of signal changes only present in the microvasculature within a given set of voxels. Activity in cerebral tissues is proportional to the need to perfuse active metabolic components through the lumen of adjacent vessels.This principle that drives CBV, CBF and BOLD is referred to "neurovascular coupling" and was first defined by Roy and Sherrington. Despite a thorough understanding of underlying mechanistic changes occurring during activity and basal states, changes revealed by all functional imaging presupposes either increased glucose uptake, water movement, cerebral metabolic rate of oxygen utilization (CMRO2) or microvascular volume. One of the most important addenda to referring to FDG PET and CBV as "measures of metabolism" is to append "as shown by glucose uptake and percent signal change", respectively.

The first step in acquiring CBV scans is the acquisition of the MRI image pairs and appropriate patient safety clearing for IV contrast injection. One issue that needs to be verified mathematically and systemically is the uptake of contrast signal in the scan. Though rare, since contrast uptake in T1 weighted signal can be verified visually

of "glucose uptake"

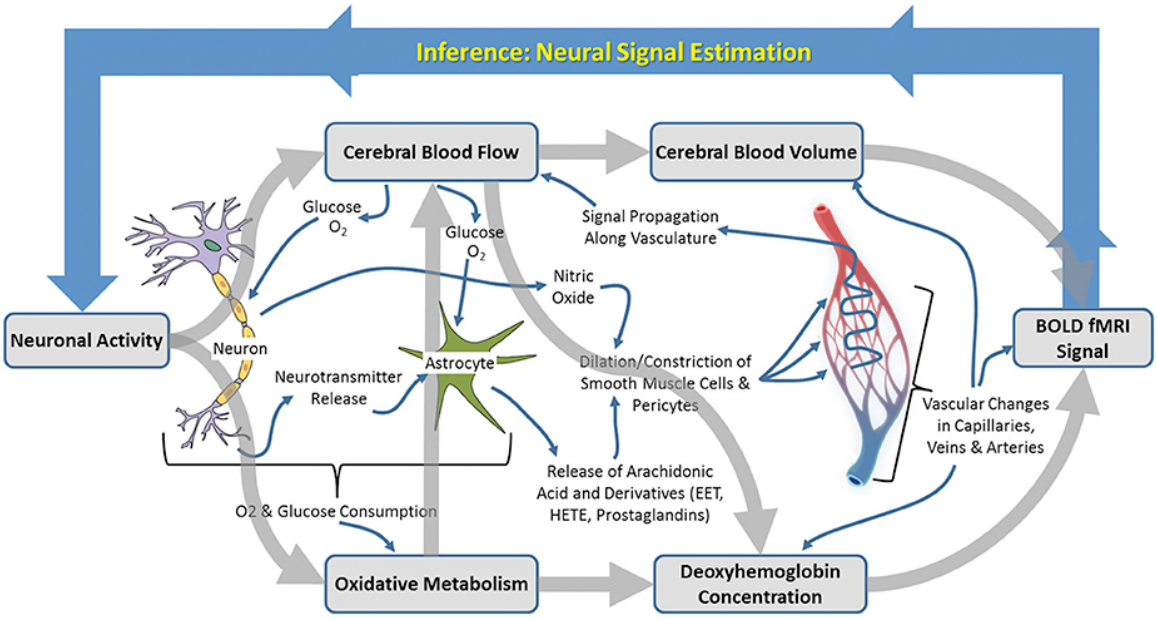

Figure 1-6: A diagram coupling neurovascular activity, metabolites, oxygen blood flow and volume[52]

by a technician, inadequate injections or improper uptake will prevent adequate signal change in the post-contrast image. Histogram analysis is used to rule out those scans prior to processing. In addition, a standard high-resolution ($<1mm^3$) image prior to the contrast image pairs is acquired and processed using FreeSurfer. The main component to generating the CBV image is isolating an area of pure blood volume. Historically, patent, large and regular cerebrovasculature is used, specifically the superior sagittal sinus.[49, 58] In the post contrast image the vessel is easily identifiable as an area of increased T1 signal. A specific algorithm isolates the largest identifiable portion of this vessel and generates a mask of its location in co-registered pre and post contrast space. An arithmetic subtracted image is calculated by taking the pre contrast image from the post-contrast image, and dividing by a value of the highest quartile of the subtracted sagittal sinus masked value. A brain mask is obtained from the binarized map, which means to set any non-zero value to 1.

FreeSurfer segmentation and several morphological techniques are also employed.

1.4.2 Statistical analysis and template atlas generation

There are two main statistical methods we employ in analyzing CBV images: mean region based and voxel based (VBA). CBV offers relatively higher spatial resolution compared to comparable functional imaging techniques (e.g. fMRI BOLD or 18-FDG PET). As such, we can capitalize on both methods in seeking to examine mean functional differences in groups both categorically and longitudinally. In the first example, VBA, the images are co-registered to a standard brain, either generated from a group specific generated template or a canonical template. N-number of statistical tests are conducted as if each measure is i.i.d. A gaussian smoothing kernel may be used after co-registration to increase SNR.[101] Statistics can be reported by setting a connected component cluster-level significance. [28]This approach is useful if the locus of signal change is expected to occur in a smaller punctate region, but the search region is unknown, as itt is unbiased to anatomical localization.

Conversely, ROI based statistical approaches rely on only one region, and generally the mean statistical value of signal in that region. This region can be chosen from either routine anatomically drawn values in native (i.e. acquisition) space or on a template to which the brains are co-registered. When the entire region of an effected area is suspected to be impaired and expected to show decreased signal, an ROI approach would yield the most significant results due to multiple comparisons. When the size and location of the region of impairment is unknown, it would be preferrable

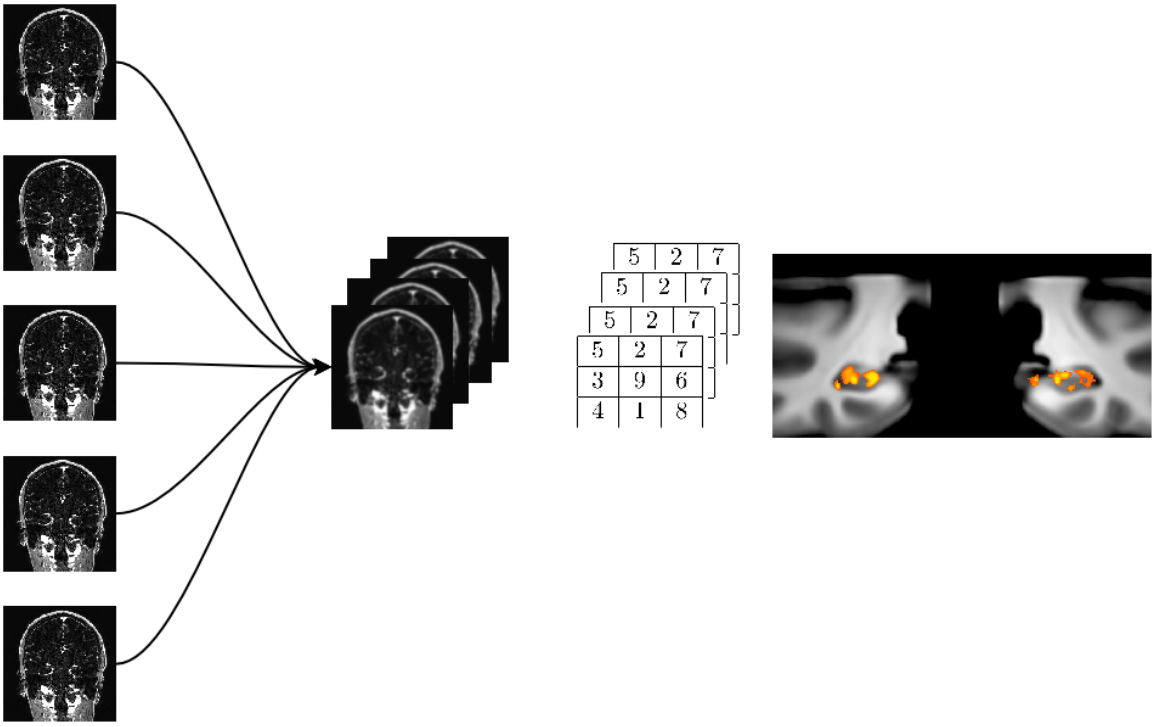

Figure 1-7: A diagram showing joined CBV maps used to generate CBV values for voxel level analysis

to focus on a VBM approach, whereas ROI analyses tend to provide statistics (most commonly mean) within a prescribed anatomical area.

1.4.3 Semi-automated analysis and error-metrics

The goal of this section was to write a software suite that could take T1-weighted images acquired with minimal a priori technician involvement and sequence parameters to generate reproducible CBV maps. Since the contrast agent impacts T1 weighting, any sequence with T1 weighting will show increased signal in the reconstructed image. To allow multiple scanners to detect the sequence and signal, we need to identify orientation, voxel size and basic SNR of both images to ensure images fall within a range to be pre-processed. Additionally, a system must be in place to filter macro

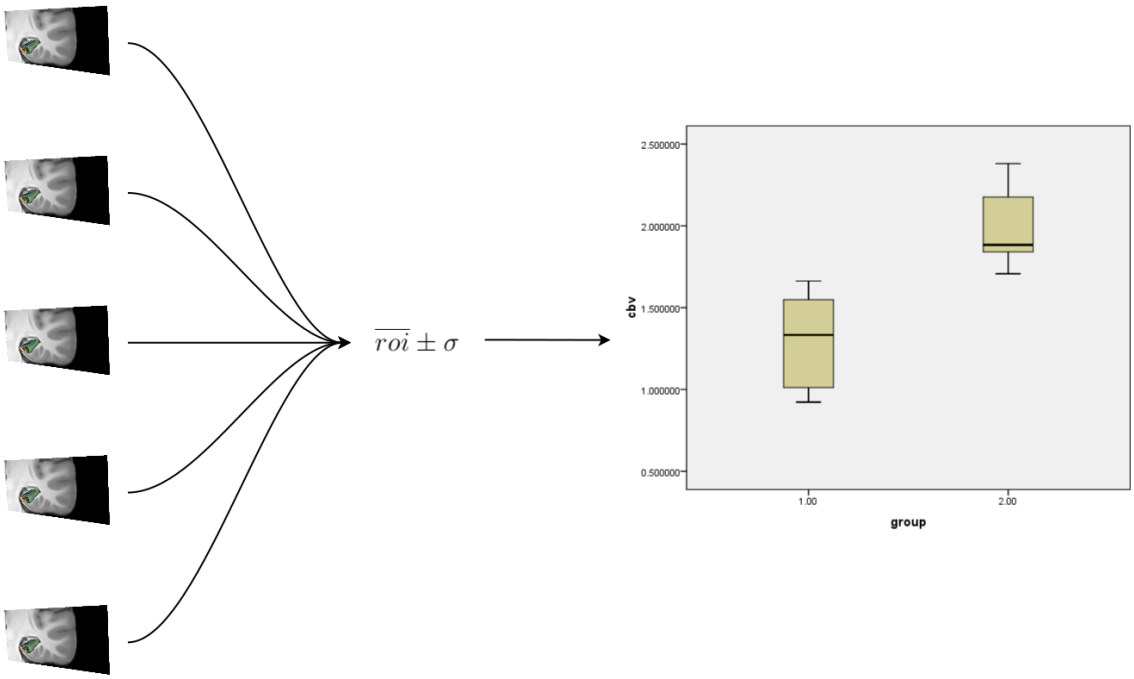

Figure 1-8: A schematic representation of how anatomically based CBV images can be used for direct statistical analyses. The left pane represents n subject images that get co-registered into a standard space of continuous values, middle, which are then used to generate voxel by voxel statistics. Since there are no time series or other corrections in place besides the initial template co-registration, any result, right, is based only on the raw subtracted and normalized signal value.

epi-cortical vessels so as they do not contribute to the regional CBV value. In original papers, a 10% threshold was used to filter such values, however, I have implemented a Gaussian model to filter discordantly high signal, effectively separating vessels larger than a voxel[50]. This model is irrespective of scanner intensity differences, as long as images are scaled appropriately in the same sequence and contrast uptake is adequate. Additionally, if either scanner, field or patient induced artifacts prevent automated vessel identification, the program will flag and allow for user investigation and intervention.

1.4.4 Parameterization and delineation of template ROIs in suspect groups

Once CBV maps have been generated, and a locus identified in a region known to demonstrate dysfunction, we must be able to either take that region or find a new regions and accurately apply to new CBV scans. For instance, in one our studies, automatically generated CBV were generated using parametric analysis and a global CBV decrease was found in pre-clinical Alzheimer's disease in patients prior to disease conversion. A particular utility in this approach would be acquiring new CBV scans on patients and stereotactically applying these parametric maps to a new brain.

Chapter 2

Specific Aim 1: Cerebral Blood Volume Toolkit Development

2.1 Examine pre and post contrast MRI images for uptake and processability

2.1.1 Introduction and study design

While there is a fascinating historical imperative governing functional brain imaging as it is practiced today, the first paper to use principles of MR images to examine relative increased activity, or function, using MRI would be by Belliveau et al.[7] In this paper, a T1-weighted MRI image was taken prior to a series of fat-suppressed echo-planar 8-10mm sagittal slice images in the V1 visual cortex in the occipital lobe. This study is often mis-intrepreted to show changes in signal concordant with BOLD,

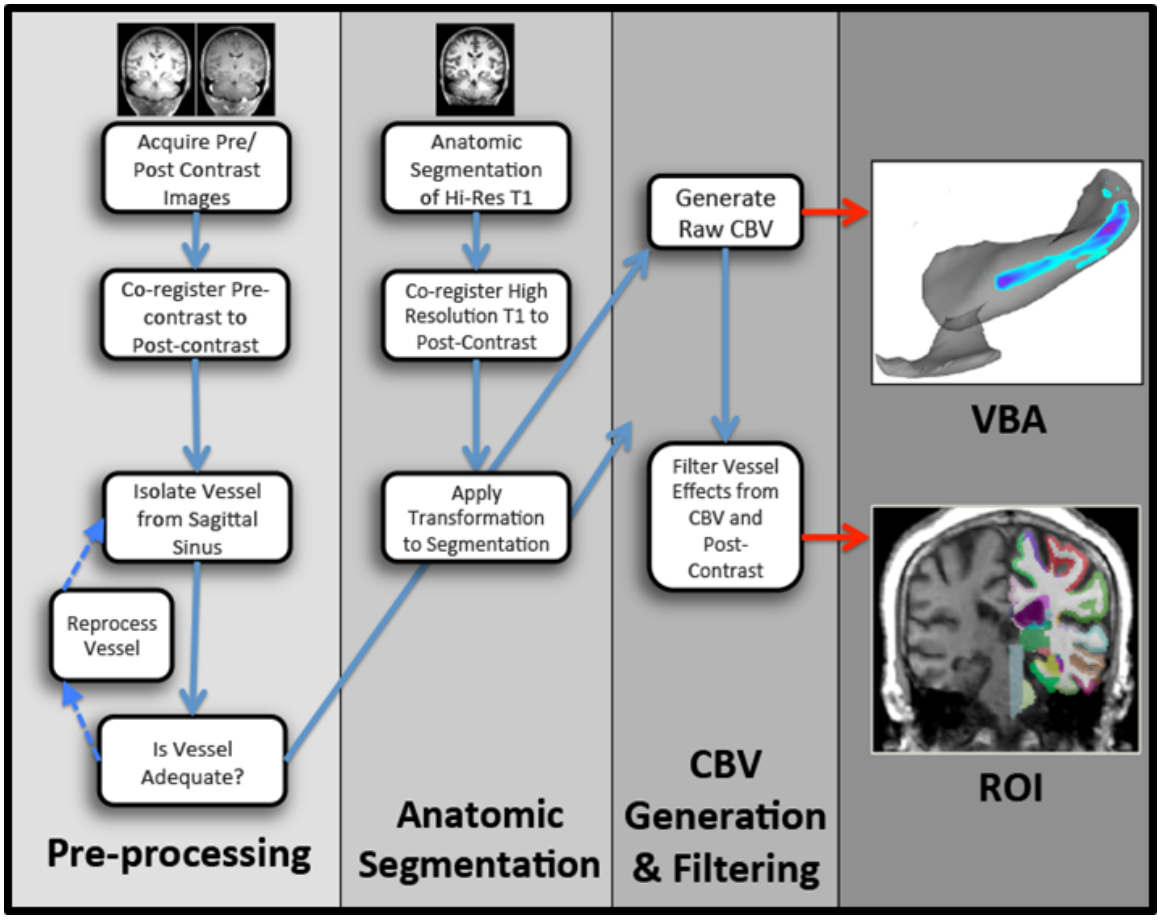

Figure 2-1: A diagram showing CBV analytic stream to generate both canonical region of interest analyses as well as voxel based analysis. Since the method of CBV generation outlied uses a pair of anisometric gradient echo images, we can use either unbiased voxel by voxel statistical measures or identify a canonical or archetypical region and co-register that region with a greated degree of certainy and fewer partial voluming effects than if it were a lower resolution EPI fMRI study or other functional image.

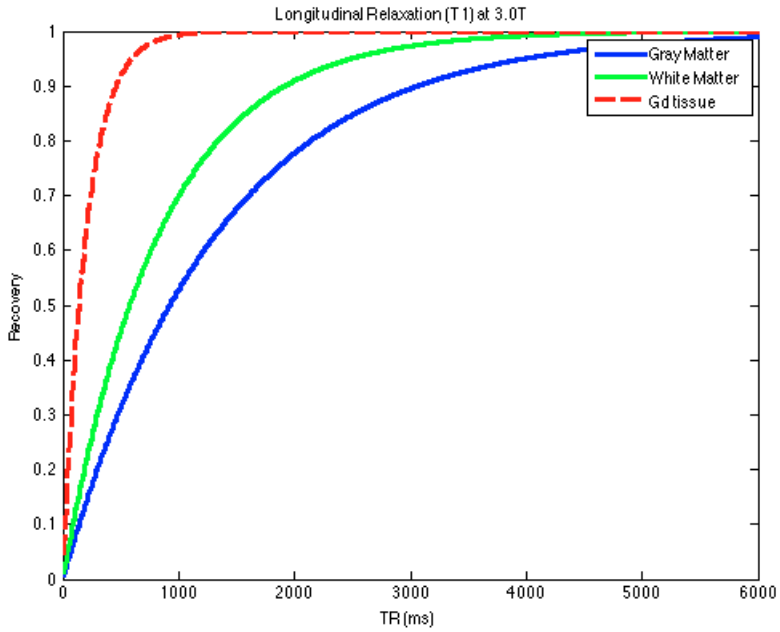

Figure 2-2: Simulated TR values for tissue classes alongside GBCA injection

but was in fact a measure local blood volume difference.[1] GBCA was administered before this process and the TR modified to account for multiple scan acquisitions. A flashing image device was fitted to elicit a strong change in cortical activity of the patient in the V1 visual cortex (in the occipital lobe).[2] The T1 was used to provide high resolution mapping while the echoplanar charted the changes of the injection of a contrast agent (chelated Gadolinium), generating a concentration-time curve, the integral of which is proportional to volume of blood in the area mapped.

While this experiment was later perfected by Ogawa et al. to define the blood oxygenation level dependent (BOLD) effect in EPI of patients, it took several years

[1]Talmudic interpretations of signal contrasts aside, MRI signal for almost all studies measure resonance changes of water, and more accurately, H^1 protons. All contrast mechanisms change either relaxivitiy or susceptibility of components within.

[2]For all fMRI studies mentioned, when discussing flashing checkerboard or other activity, all studies are dynamic sequences that look at either the increase in volume, flow or DeOHb from local changes in susceptibility or T1 shortening. ssCBV always acquires just one pair of scans; if multiple T1 scans are acquired, it often follows DCE modeling.[91, 74]

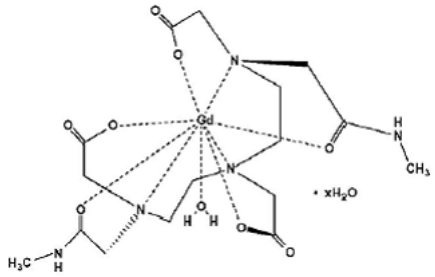

(a) a

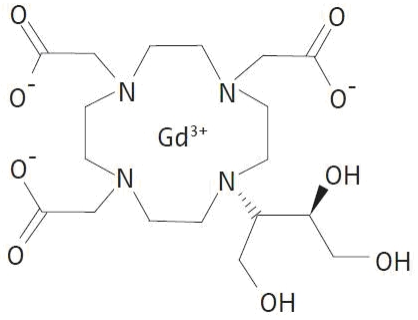

(b) b

Figure 2-3: (Two variations of chelated gadolinium contrast agent. Chelation is a process by which elemental or ionic gadolinium is bound to an inert substance that remains in the vasculature without passing the blood brain barrier of a healthy individual and is eventually excreted. (a) shows gadodiamide marketed as *Omniscan* and (b) shows Gadobutrol marketed as *Gadovist*

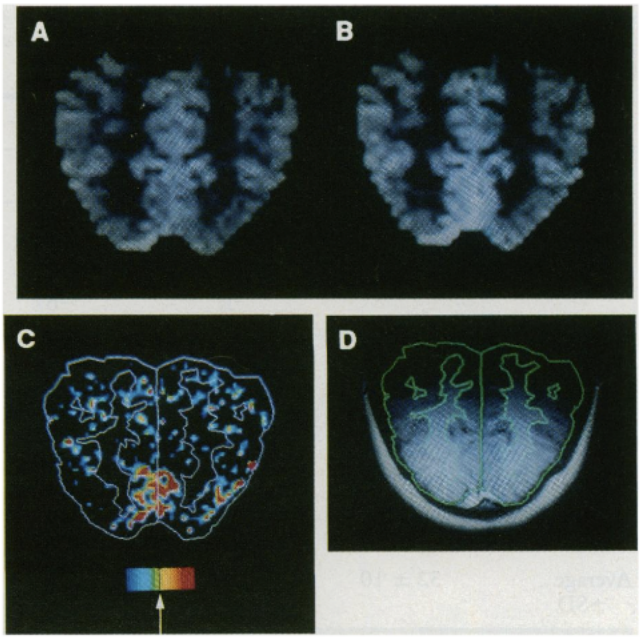

Figure 2-4: Instance of contrast enhanced signal change mapped on orthogonal projections of the brain[7]

$$C(t) = \frac{K(t - T_a)}{\beta} \exp(-\frac{t - T_a}{2\beta}) \tag{2.1}$$

Figure 2-5: Levenberg-Marquart concentration time curve of the change in ΔR2 ($\propto 1/\Delta$T2)as a function of bolus detection of GBCA injection. Both β and K are inherent functions of the curve fitting procedure, T_a is the time at which the bolus is injected and 't' is the time.[50]

to examine the basal changes in magnetic susceptibility using T1 weighted imaging in patient groups.[64] Lin et al. proposed a series of experiments repeating Belliveauś

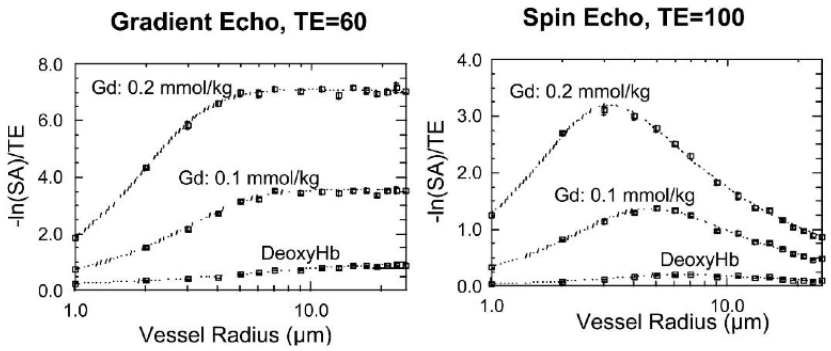

Figure 2-6: Comparison of exogenous, at multiple injection doses, and endogenous contrast agents in both gradient and spin echo MR sequences. Note ordinate is log-transformed.[66]

EPI techniques while adding a fairly generic T1-weighted sequence prior to and after the bolus injection of Gadolinium. Relaxivity values for known tissue types can be seen in 6.1.[50] This sequence was a FLASH (fast low angle shot) MRI originally designed to reduce the time of a T1 image acquisition. Since T1 times for water and tissue are larger than T2*, scanning time is an important consideration irrespective of magnetic sequence strength in developing a human MRI protocol. While T1 imaging for a sample of brain has sampling and physical proton relaxation constraints, a sub-milimeter isometric MRI pair can be acquired using current software techniques in approximately 12 minutes, an important consideration for patient compliance.[10, 24] Our lab was interested in examining was the physiological changes predicted by disease state in areas of the medial temporal lobe of the brain. To do so requires a high resolution functional image that captured the hippocampus along its longest axis;

coronal. Both murine and human variations of this steady-state exogenous CBV protocol were developed.[67, 68]

2.1.2 Methods

Image sequence and parameters for this study had been previously defined, tested and validated to optimize SNR and patient scanning time. MRI scan pairs had been acquired prior to and during the initial phase of this study using those identical parameters on a Philips Achieva 3T MRI scanner with a 32-channel SENSE head coil. A T1-weighted gradient echo scan using FFE ("T1-FFE"), FOV 240x196, TR=7, TE=3, TI=1000, FS=10, 2 dynamics, Voxel size 0.68x0.68x3mm^3.[92, 20, 69] An archetypical pulse sequence diagram can be seen in 6-13. A gradient echo image with rf spoiling is ideal (compared to gradient spoiling) for several reasons[3]:

- It is invariant in space
- Does not generate eddy currents (a common contributor to MRI noise)
- Is governed by phase changes the generally follow a fixed quadratic formula

The non-zero composition of the MRI matrix follows a modest Gaussian distribution. In order to determine whether the requisites scan acquisitions are suitable for processing, several requirements need to be met, specifically adequate contrast uptake and minimal movement artifacts. There should be a way to see if proper gadolinium uptake occurred, as well as if other artifactual errors have occurred which would preclude proper pre-processing. We assume MRI technicians will perform the necessary

[3]Spoiling of gradient echo pulse sequences are routine in modern-day clinical practice for the time and availability they provide

phantom studies and address scanner quality control assumes that permit two acquisitions without any scaling differences. Therefore, the only changes between sequence reconstructions will yield only changes attributable to factors such as RF noise, fluid movement inside the tissue being imaged. Therefore, the introduction of a systemic 'tracer', influencing a reduced T1-relaxation time and increased signal should cause the total histogram of the signal to increase, assuming a static scaling parameters. Tissue class segmentation is influenced by global histogram calculations. Gadolinium accumulates throughout a subjectś entire vasculature, but specifically does not cross the BBB in patients with an intact BBB[34, 46]. We therefore assume (and require) such integrity in patients for whom a CBV analysis is to be performed. However, as part of good radiological practices, one may discover an infarct or bleed through MR contrast administration. For these patients, a BBB integrity assumption fails, (i.e. acute trauma or malignancies), and a gadolinium-enhanced MRI could not be used for CBV calculations.

To test whether an image was properly perfused, images are converted to non-scaled the non-zero histograms of brain-extracted voxels of co-registered images (pre and post contrast) were calculated and examined. "Brain-extraction" refers to the process by which constructed MRI images are separated into the internal cerebrum and neuronal structures and the outer dura matter, cerebral spinal fluid, skull and skin.[85] Additionally, the images'regional cortical and subcortical values were examined using Freesurfer.[22] A mean difference was calculated and any results after the max histogram distribution (presumably of white and gray matter) is noted. For any can that does not have adequate uptake, this difference is orders of magnitude

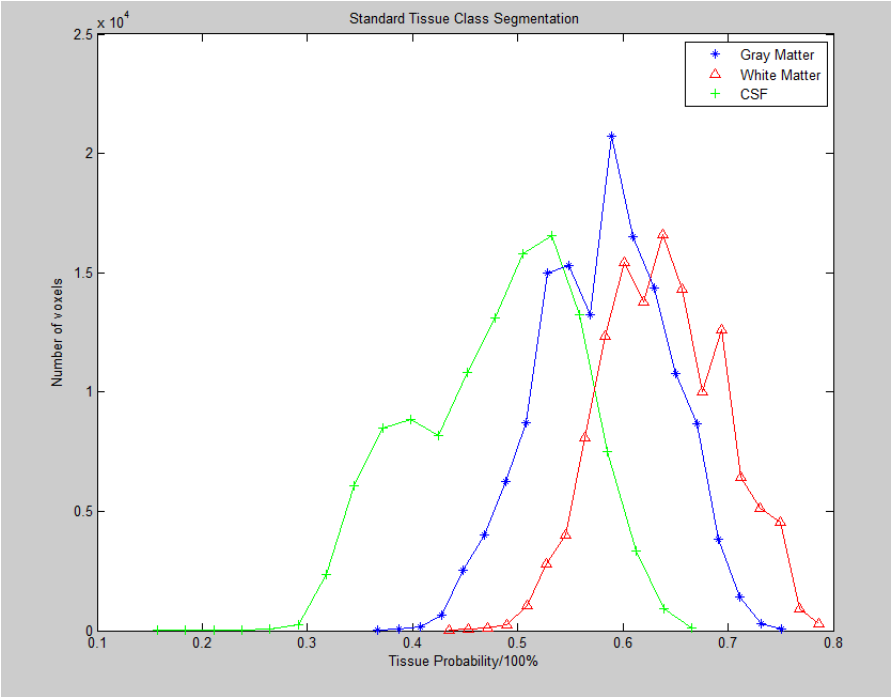

Figure 2-7: Non-zero histogram distribution for tissue classes using a standard class segmentation protocol.[2]

smaller than one for which it does. Besides examining the capacity for uptake, this pre-requisite algorithm will examine whether images were scaled using the same parameters.

2.1.3 Results

For a sample of 50 patients who had been recruited to have the pre-requisite CBV scans (pre and post contrast MPRAGE, .68x.68x3mm), two scans had been identified through traditional user curated methods to not meet standards contrast perfusion. A template was created using 20 normal controls to generate an averaged scaled histogram and mean values of a two-degree Gaussian distribution were compared from each scan pair to the "template". To provide a coarse metric or scanner uptake,

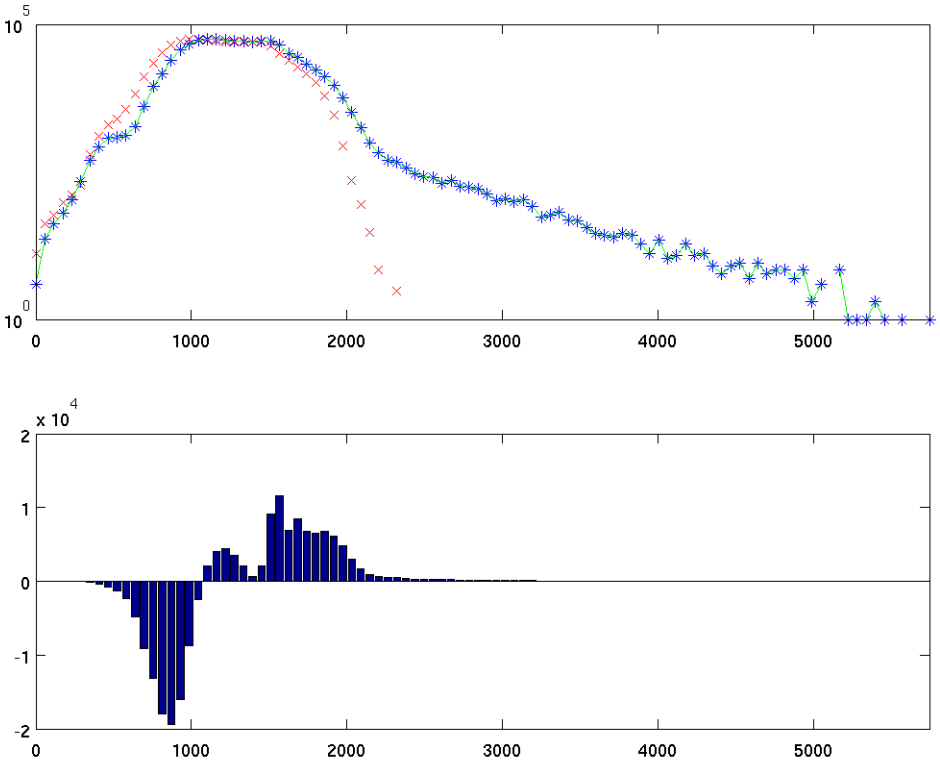

Figure 2-8: A dual histogram analysis panel: The top panel refers to non-zero histogram bins of 100 for the pre-contrast image in red and the post contrast image in blue. The lower panel refers to the subtracted histogram difference.

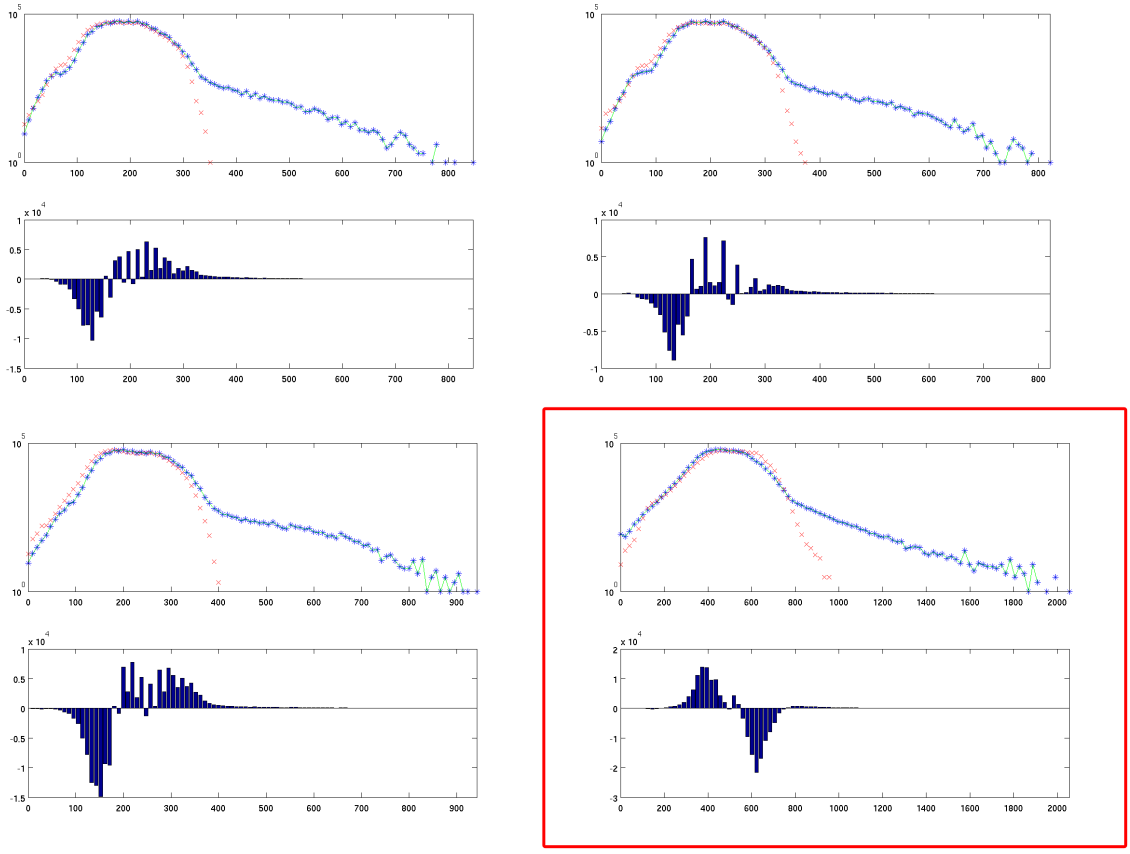

Figure 2-9: A set of four pairs of dual histogram analysis panels. TL, TR, BL all refer to patients who have had adequate contrast uptake an little movement. BR shows a patient with poor contrast uptake (often when the administration of i.v. GBCA bolus of GBCA does not enter the venous system). The bottom histogram difference can be seen to be reversed, whereas the previous bimodal distributions are clearly - and +, the bottom is reversed. Sometimes, if not revered, the fit is below a particular R^2 value when the function is minimized.

$$g(s) = \frac{1}{2\sqrt{\pi}} a_1 \exp\left(\frac{(s-b_1)^2}{2c_1^2}\right) + \frac{1}{2\sqrt{\pi}} a_1 \exp\left(\frac{(s-b_2)^2}{2c_2^2}\right) \tag{2.2}$$

Figure 2-10: A modified 2-degree gaussian distribution

signs of both means were measured as it was observed empirically that the histogram differences for all patients followed a negative first degree value (indicating voxels in the pre-contrast image that become perfused) and a positive second degree value (indicating voxels those same voxels in the post contrast image). The algorithm correctly identified every patient previously identified by rater observation to have poor contrast uptake by rater identification. We plan to explore the changes in histograms presented through movement which would improperly scale MRI images.

2.1.4 Conclusion

This is an important *a priori* measurement technique to rule out patient scans before calculation and allow a trained rater to either support the algorithm findings and exclude or further investigate. Either way, it reflects an important feature germane specifically to matched intra-class, intra-modal contrast agent images.

2.2 Identify region of pure blood in the superior sagittal sinus

2.2.1 Introduction and study design

CT or MR Angiography is an important technique in radiology to identify and examine cerebrovascular abnormalities such as aneurysms or infarct. Angiography identifies areas within tissue where active perfusion occurs.[26] In the non-acute setting where MRI has been cleared for the patient, there are two methods to generate the extent of

vascularization: time-of-flight (TOF) dynamic and contrast based MR imaging. Current FDA guidelines suggest TOF methods unless it is otherwise contraindicated.[38] Although the entire vasculature might help get a greater sampling data of mean blood volume extant literature supports isolating the main venous output of the superior portion of the brain, the superior sagittal sinus. Sampling voxels within this vessel provide a value of averaged expected signal in a modality (whether it be dynamic PET or contrast MRI) that can be used as a normalization of tissue values. For dynamic MRI imaging using a kinetic modeling, there is often an AIF measure that is acquired. This is a voxel that is placed either by software or a technician, but is often noisy and a source of error or variance.[47] In wanting to generate new CBV images and adhere to previous protocols as much as possible, we wanted to capture a portion of this vessel that we assume to be measurable in all patients repeatedly with no severe cerebral abnormalities using a semi-automated procedure. We wanted to adapt a method to identify only the specific locus of cerebrovasculature we wish to sample, the main venous outflow of the cerebrum, the SSS.

2.2.2 Methods

Clinicians order T1 weighted MRI with contrast (i.e. gadolinium) to show vasculature whilst preserving gray matter and white matter anatomy frequently. Vasculature in those images can be predicted in three dimensions through thresholding and stacking each slice orthogonal to the thickest axis (usually B0 or the axial plane, but in our case oblique coronal). We can use existing techniques using linear algebraic methods

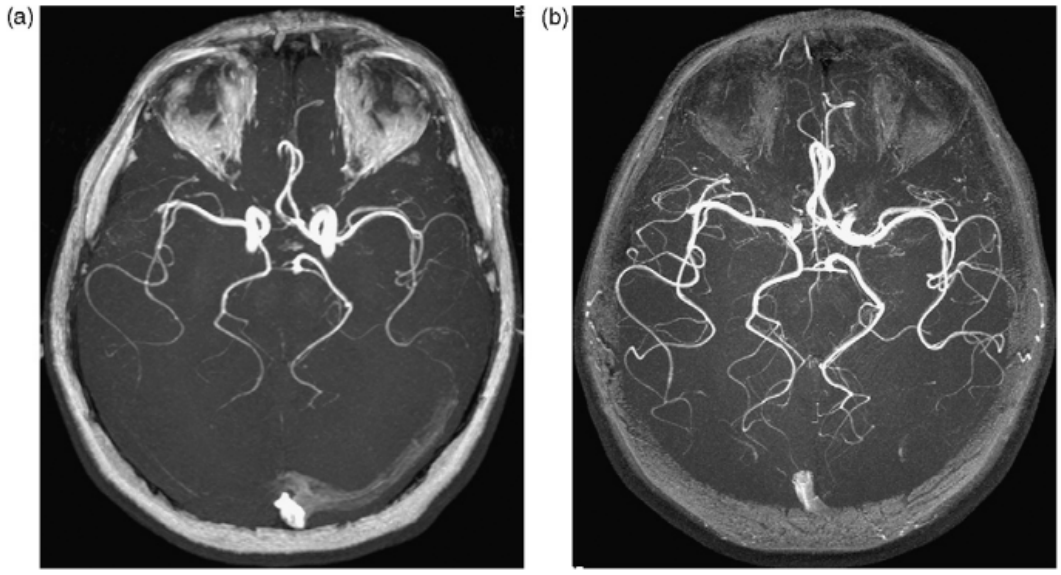

Figure 2-11: Sample time of flight (TOF) MRA with a 1.5 T MRI field strength acquisition (a) and a 3.0 T MRI field strength acquisition. [1]

$$\mathbf{H}(x) = \begin{bmatrix} \frac{\partial^2 f}{\partial x_1^2} & \frac{\partial^2 f}{\partial x_1 \partial x_2} & \cdots & \frac{\partial^2 f}{\partial x_1 \partial x_n} \\ \frac{\partial^2 f}{\partial x_2 \partial x_1} & \frac{\partial^2 f}{\partial x_2^2} & \cdots & \frac{\partial^2 f}{\partial x_2 \partial x_n} \\ \vdots & \vdots & \ddots & \vdots \\ \frac{\partial^2 f}{\partial x_n \partial x_1} & \frac{\partial^2 f}{\partial x_n \partial x_2} & \cdots & \frac{\partial^2 f}{\partial x_n^2} \end{bmatrix}. \tag{2.3}$$

Figure 2-12: Form of the Hessian matrix

to classify vessels using local matrix changes and definining shape parameters. These parameters are based on the eigenvalues of the hessian matrix and is referred to as a vesselness measure, as first described by Frangi.[27]

Frangi proposes two dissimilarity features to quantify and detect on a voxel basis. These features are based on the three eigenvalues of each voxel of the hessian form.

$$\mathcal{R}_{\mathcal{A}} = \frac{|\lambda_2|}{|\lambda_3|} \tag{2.4}$$

Figure 2-13: Ratio component for the blob likelihood.

$$\mathcal{R}_{\mathcal{B}} = \frac{|\lambda_1|}{\sqrt{||\lambda_2 \lambda_3||}} \tag{2.5}$$

Figure 2-14: Ratio component for structures that range from flat circle to line structures.

$$S = \|\mathcal{H}\|_F = \sqrt{\sum_{i \leq D} \lambda_i^2} \tag{2.6}$$

Figure 2-15: The 'structureness' component

$$\mathcal{V}_o(s) = \begin{cases} 0 & \text{if } \lambda_2 > 0 \vee \lambda_3 > 0 \\ (1 - \exp(-\frac{\mathcal{R}_{\mathcal{A}^2}}{2\alpha^2}))(\exp(-\frac{\mathcal{R}_{\mathcal{B}^2}}{2\beta^2}))(1 - \exp(-\frac{\mathcal{S}^2}{2c^2})) \end{cases} \tag{2.7}$$

Figure 2-16: All components joined together to produce final grayscale invariant vesselness equation.

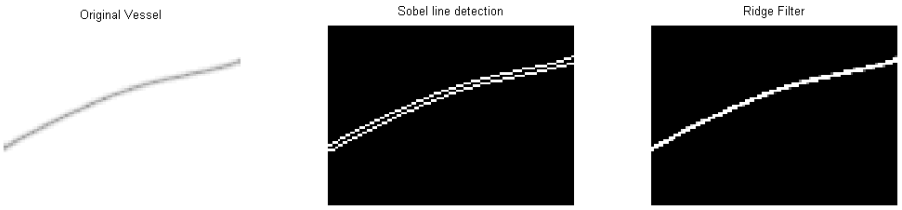

Figure 2-17: A sample image shown in A upon which an edge detection B is performed and a "Ridge" detection is performed. One can see the identifiable areas in the edge detection bound the area contained between those points, adding to difficulty for a multiple voxel boundary, or in the event an edge contains features between the abutting areas. A "Ridge" detection in C isolates the local points of infection by discretizing and modeling as a 2^{nd} degree polynomial, identifying only areas of inflection, making it ideal for vessels larger than two voxels length.

The jacobian of the 1st order derivative minima will not capture steep changes (as in the border between a vessel edge and T1 signal modulated cisternal space)in n-dimensions. Nor will it be useful in defining high intensity local changes. Instead, we chose to use 2nd order derivitives which are sensitive to points of inflection which better characterize regions where greatly increased signal are present next to physical boundaries where the signal drops off quickly. This form of the 3D matrix is called the Hessian. However, many structures in the post-contrast brain have local minima and maxima parallel to the plane of the sagittal sinus, and we wish to identify only that structure which contains the vessel in question. The steps to identify such a region are two-fold: 1) generate a probabilistic *a priori* atlas of the superior sagittal sinus and 2) to use that atlas as a probabilistic model in identifying the same vessel.

We use the vesselness method on the post-contrast image (to avoid any additional co-registration artifacts from later methods in the processing).[27] The subtracted image, which is closer in practice to an MRA was not used in order to reduce the chance of errant clusters of bright voxels. We perform morphological operations on the final thresholded vesselness map and morphologically erode those images with a cubic kernel (as seen in 2-20), apply a thresholding on the grayscaled minima and create a connected component map of the possible vessels.

We then co-register the masked connected component mask unto a co-registered probabilistic vessel atlas of manually curated vessels and choose the vessel with the highest value as seen in 2-23.

We use a Bayesian classifier to calculate the approximate vessel from a $\hat{z}$ seen in 2-21

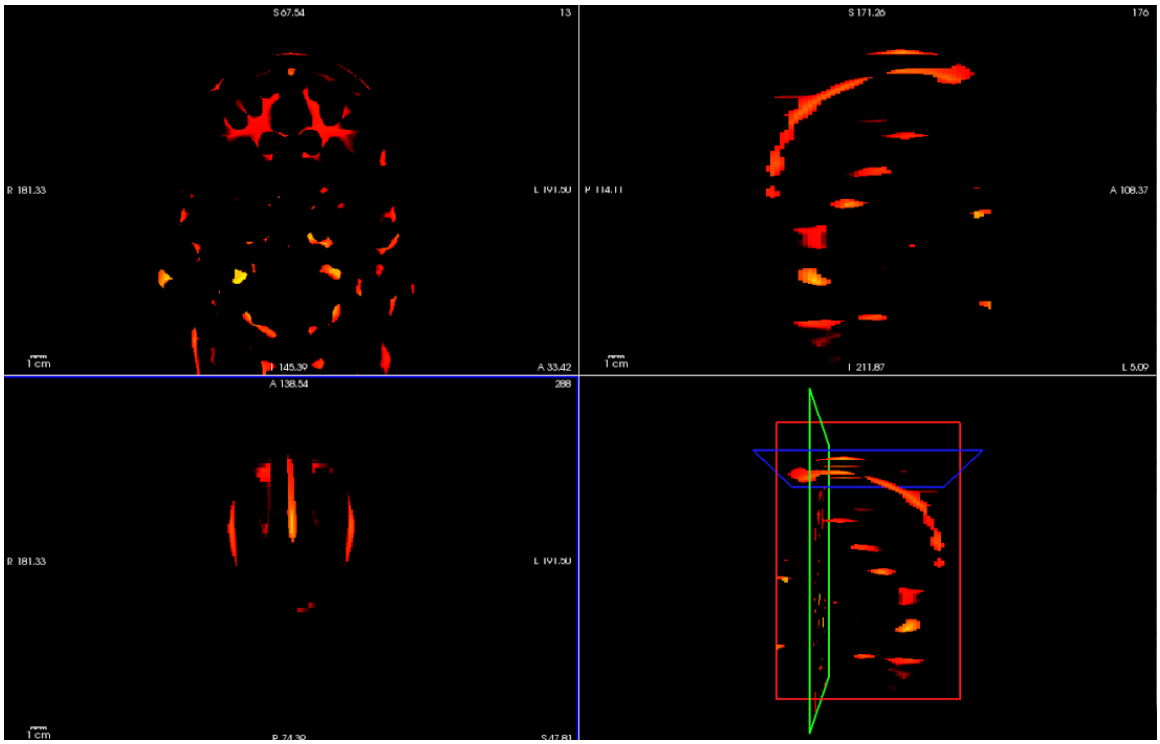

Figure 2-18: The raw vesselness map generated from a random subject's post gadolinium scan. TL is oblique coronal to the long axis of the hippocampus, TR is sagittal anisotropic and BL is axial anisotropic. One can make out several structures including the bulk of bilateral hemispheric WM. We are only interested in the isolated region located medial and superior to both of those regions.

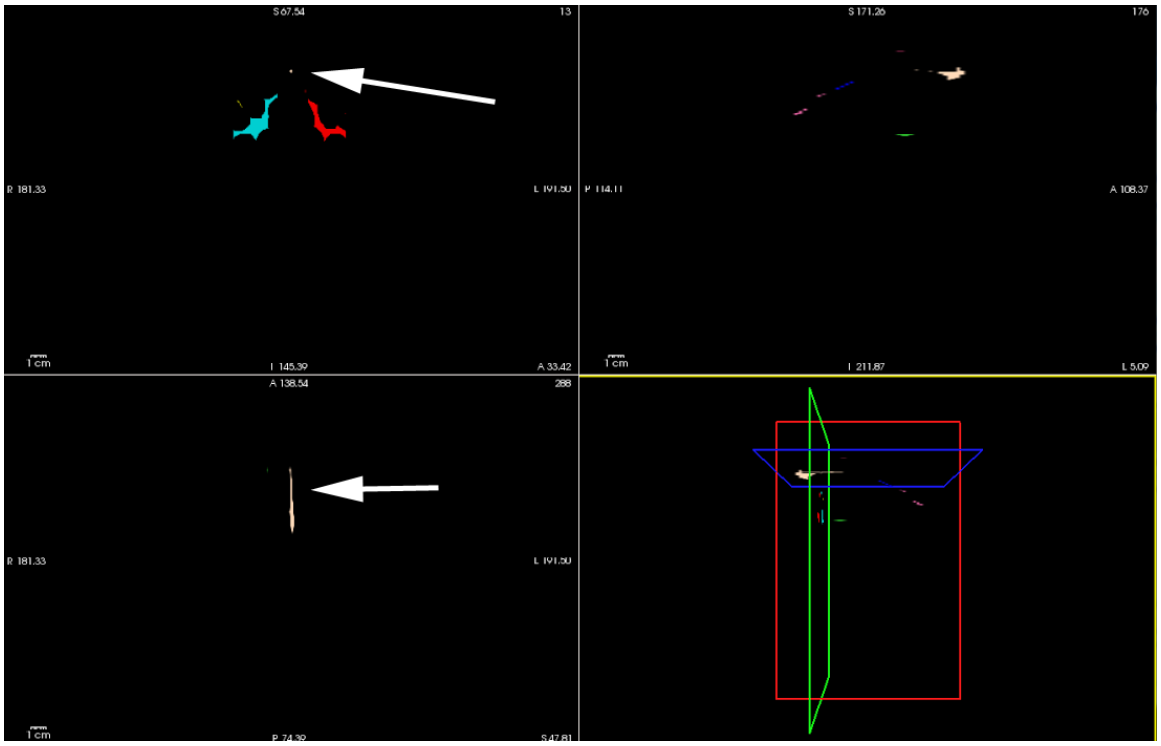

Figure 2-19: The same vesselness map in 2-18 with a connected component algorithm applied with false color. Each color reflects a masked region of contiguous voxels in n-dimensional space. The area we wish to identify is indicated with an arrow.

$$img = \begin{bmatrix} 1 & 1 & 1 & 1 & 1 \\ 1 & 1 & 1 & 1 & 1 \\ 1 & 1 & 1 & 1 & 1 \\ 1 & 1 & 1 & 1 & 1 \\ 1 & 1 & 1 & 1 & 1 \end{bmatrix}, b = \begin{pmatrix} 1 & 1 & 1 \\ 1 & 1 & 1 \\ 1 & 1 & 1 \end{pmatrix}, \text{img} \ominus \text{b} = \begin{bmatrix} 0 & 0 & 0 & 0 & 0 \\ 0 & 1 & 1 & 1 & 0 \\ 0 & 1 & 1 & 1 & 0 \\ 0 & 1 & 1 & 1 & 0 \\ 0 & 0 & 0 & 0 & 0 \end{bmatrix} \tag{2.8}$$

Figure 2-20: Here, a n-dimensional image (where n=2), img is eroded with structuring element b. For our analyses, kernels were cubic 3x3x3.

$$\hat{z} = \underset{k \in \{1,\ldots,K\}}{\text{argmax}} \; p(V_k) \prod_{i=1}^{n} p(x_i | A_k) \tag{2.9}$$

Figure 2-21: Here we wish to determine a vessel value from $\hat{z}$, from the total connected components V $\in k$, as a function of the existing atlas mask, A, and voxels in a potential mask.

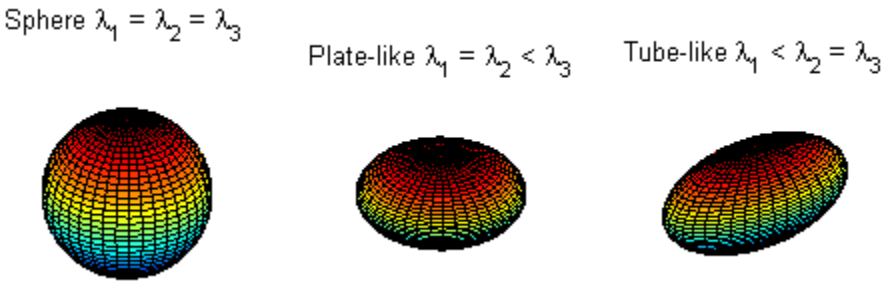

Figure 2-22: Eigenvalue shape descriptions based on the hessian matrix of a sphere (or 'blob' structure), plate-like and tube-like structure. Tubular structures can be identified by adjusting values of the prescribed eigenvalue amounts

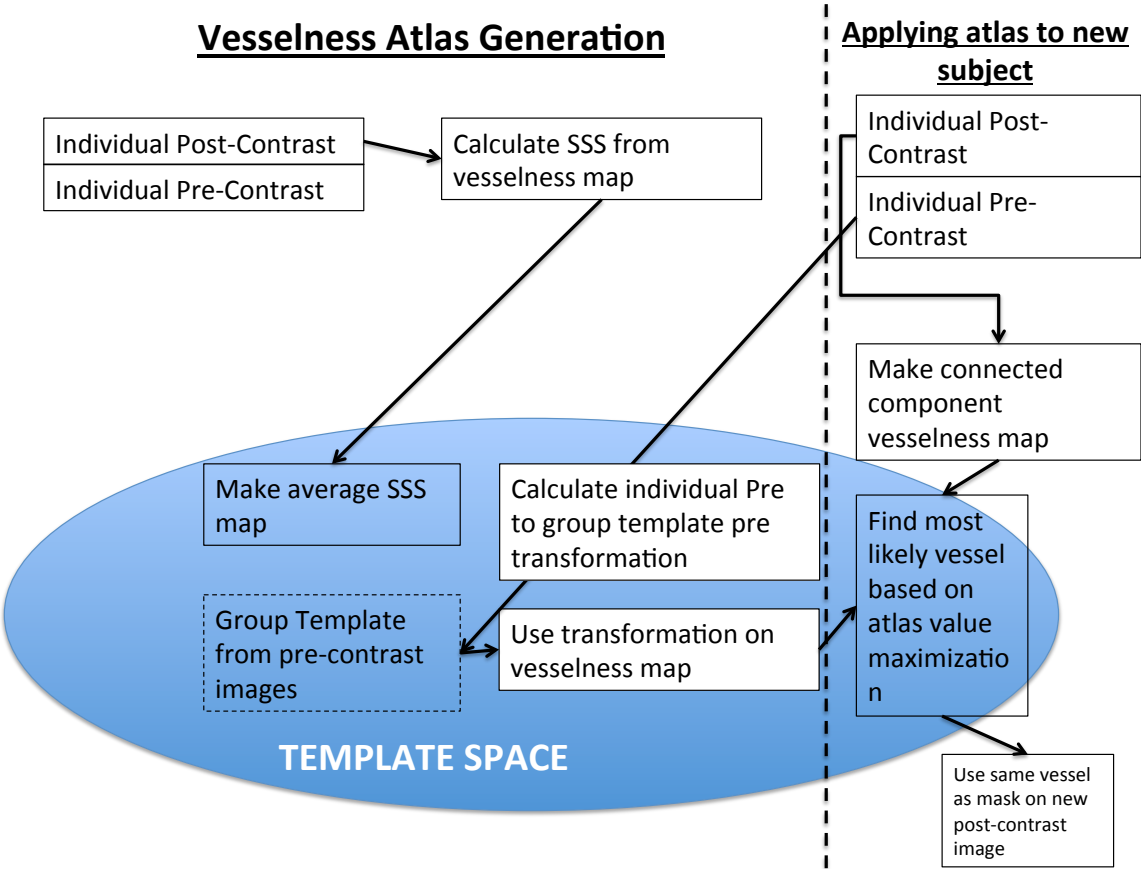

Figure 2-23: Diagram of how the vesselness atlas is created. Although we have used an aforementioned 3.0T MRI vesselness mask as our primary atlas, this explains the framework for both the creation of new vessel atlas and the application of said atlas to any new image which has had vesselness operated on it.

$$CBV = \frac{T_{Post} - T_{Pre}}{SSS_{Post} - SSS_{Pre}} \tag{2.10}$$

Figure 2-24: relative CBV is calculated from tissue, T, in a voxel in the post and pre contrast image divided by the mean value of blood as calculated from the superior sagittal sinus (SSS) in the post and pre contrast images. The denominator for each voxel in the subtracted tissue image is identical.

Once the final vessel is finally calculated the final CBV image is calculated using the following formula

2.2.3 Results

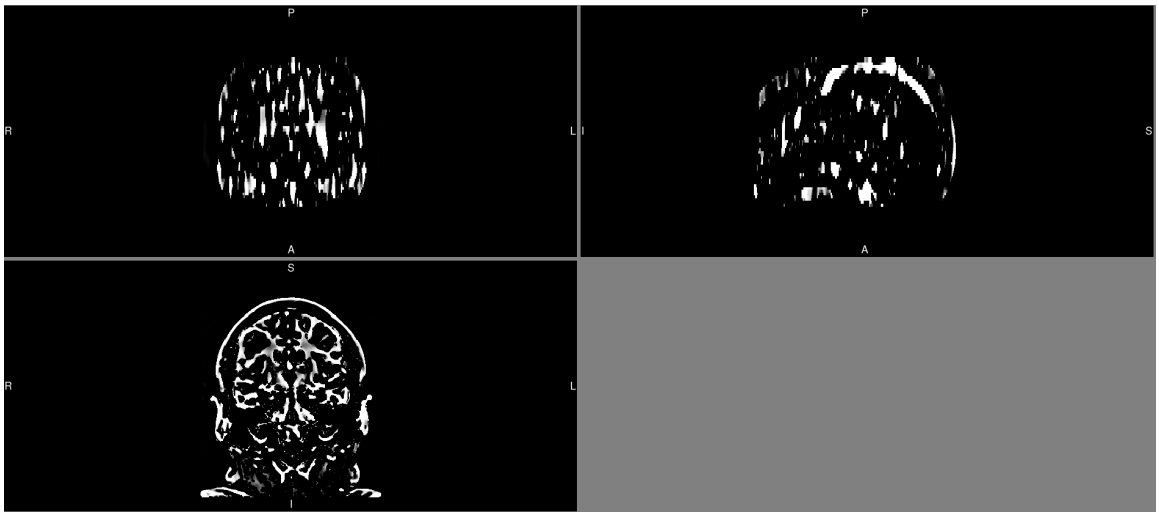

Figure 2-25: Vesselness maps with the following characterstics: α=0.05, β=20, c=30. For the scanner on which most of the pre and post contrast MRI pairs have been acquired, these are the values which have been shown to be most useful in generating reliable SSS extraction maps.

A successful vessel segmentation is defined as any ROI in which at least four voxels are isolated inside of a vessel. A mask atlas was created from a diverse population across a varied population. A top proportion of vessels is chosen from either the subtracted image or the post-contrast image, although both methods reveal similar values.

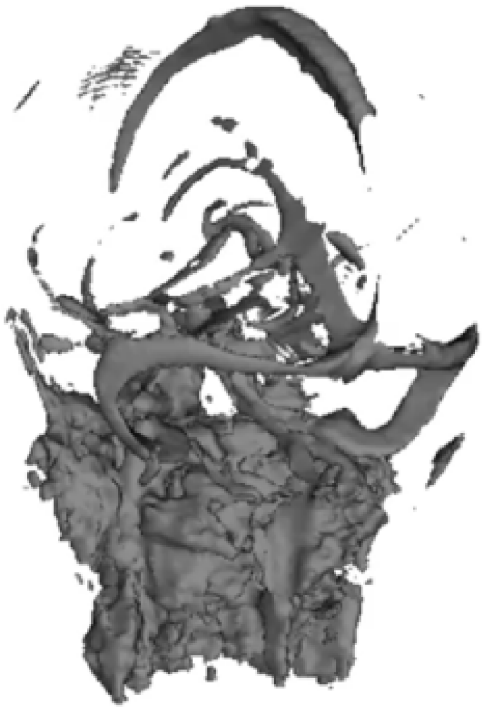

Figure 2-26: Rendering of an averaged and thresholded joint magnetic resonance angiography from a sample of co-registered vesselness maps. Note the clearly defined superior sagittal sinus on the top of the image as well as other

2.2.4 Conclusions

This particular method of vessel segmentation has provided accurate vessel representations on all of the patients to which it was applied. SSS integrity is one of the necessary components to analysis and we wish to semi-automate this process to permit for regular identification of this particular neuroanatomical structure.

2.3 Identification and elimation of epicortical vessels in ROI analysis

2.3.1 Introduction and study design

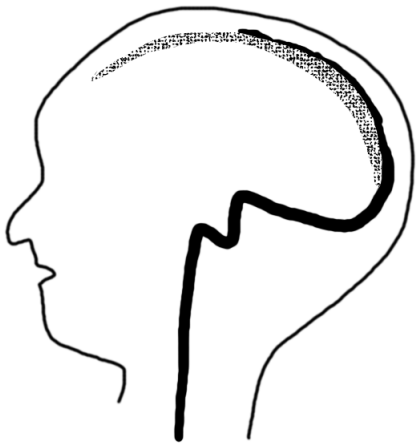

Figure 2-27: Anatomical representation of the main cavernous outflow (shown with a texture) and inflow (shown with a bold line) within the vasculature of the brain.

The brain is richly vascularized and consists of a gossamer system of extra or epicortical arterial input and venous outflows. Identification of areas located within these

largest regions allow low resolution (>1.5 mm^3) MRI images to identify voxels contained entirely within voxels thought to represent an area containing only pure blood. These areas are helpful for clinical applications of gross vascular abnormality such as measurement of blood brain barrier integrity, however, do not relate necessarily to the changes in discrete cerebrovascular function that associates with angiogenesis and synaptogenesis that we wish to measure using our CBV mapping techniques. Lin et al. prescribed a strict threshold of the highest 10% of all signal in the subtracted brain. [50] However, this original specification was meant for animal models with smaller variance in total head and neck size and shape. Hence, a hard coded percentage value does not take into account large changes in signal uptake found in the event that a patient has more tortuous or dense large vasculature.[16] To apply a dynamic approach to this filtering, we sought a method irrespective of all present signal and anatomy.

2.3.2 Methods

MRI scaling parameters for every CBV are not fixed and the intensity values present in images going to contain a mixture of values not fixed at a 10-binned histogram. A Gaussian model curve fitting for subtracted histograms was observed. Using a curve fitting procedure similar to the method described to identify uptake, as well as empirical observation of vasculature elimination as it is defined in the subtracted image (as areas of very high signal) we decided to fit a separate 2 degree Gaussian curve, eliminating all values 2.5σ above the second gaussian mean. Here we expect

variation within the distribution, as demonstrated before, however the value of 2.5σ was tested on a sample of 94 patients who had acquired the standard pre-requisite CBV scans. Empirically, each scan was inspected in this group and locations within the medical temporal lobe that are thought to contain high beds of vascular were examined along the long axis of the hippocampal circuit. An example of this patient is shown in 2-34.

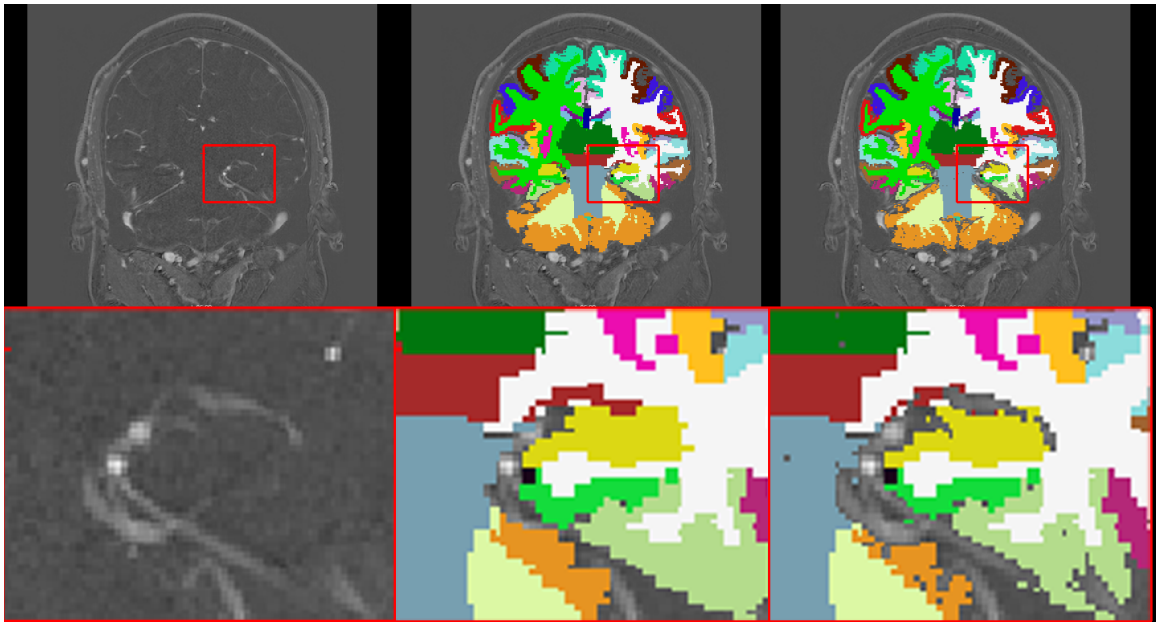

Figure 2-28: Sample MTL section of a non-brain extracted subtracted image (TL) The subtracted image. Outlined expanded below in BL. (TM) Freesurfer cortical segmentation mask (where each color represents a unique different region) overlaid onto the co-registered subtracted image. Some vasculature revealed by the subtracted image is present in the masked labels, however much is still claimed as regions since most GRE sequences Freesurfer suggests and for which it is optimized do not have any sort of vascular delineation. Outlined expanded below in BM. (TR) This section represents the cortical mask (CM) excluding any voxels which fall outside of the GMM in the vessel mask (VM) (*i.e.* $\text{CM} \wedge \neg\text{VM}$). Outlined expanded below in BL.

2.3.3 Results

Time of flight MRA information for these patients is unavailable, and if available would not necessarily align with gadolinium accumulation, since TOF MRA will not capture small vasculature. The basis for shortened T1 signal with steady state CBV is that microvasculature will exhibit increased T1 signal in patients within an arithmetic subtracted image.[100] However, by applying this signal filtering method on a large quantity of patients, we are able to manually inspect and verify adequate vessel filtering, and compare existing histogram analyses with previously acquired CBV maps.

2.3.4 Conclusions

Using this method we have improved upon an approach that does not take into account all possible histogram values. We have extended it to be adaptable to any coverage area, although there is still ways to improve upon it. Particularly, to perform isolated vascular closing on the final maps (errant voxels whose value falls outside the range of appreciable Gaussian model). While these voxels max reflect true CBV values within that area, we don't wish to include that into any appreciable validated method.

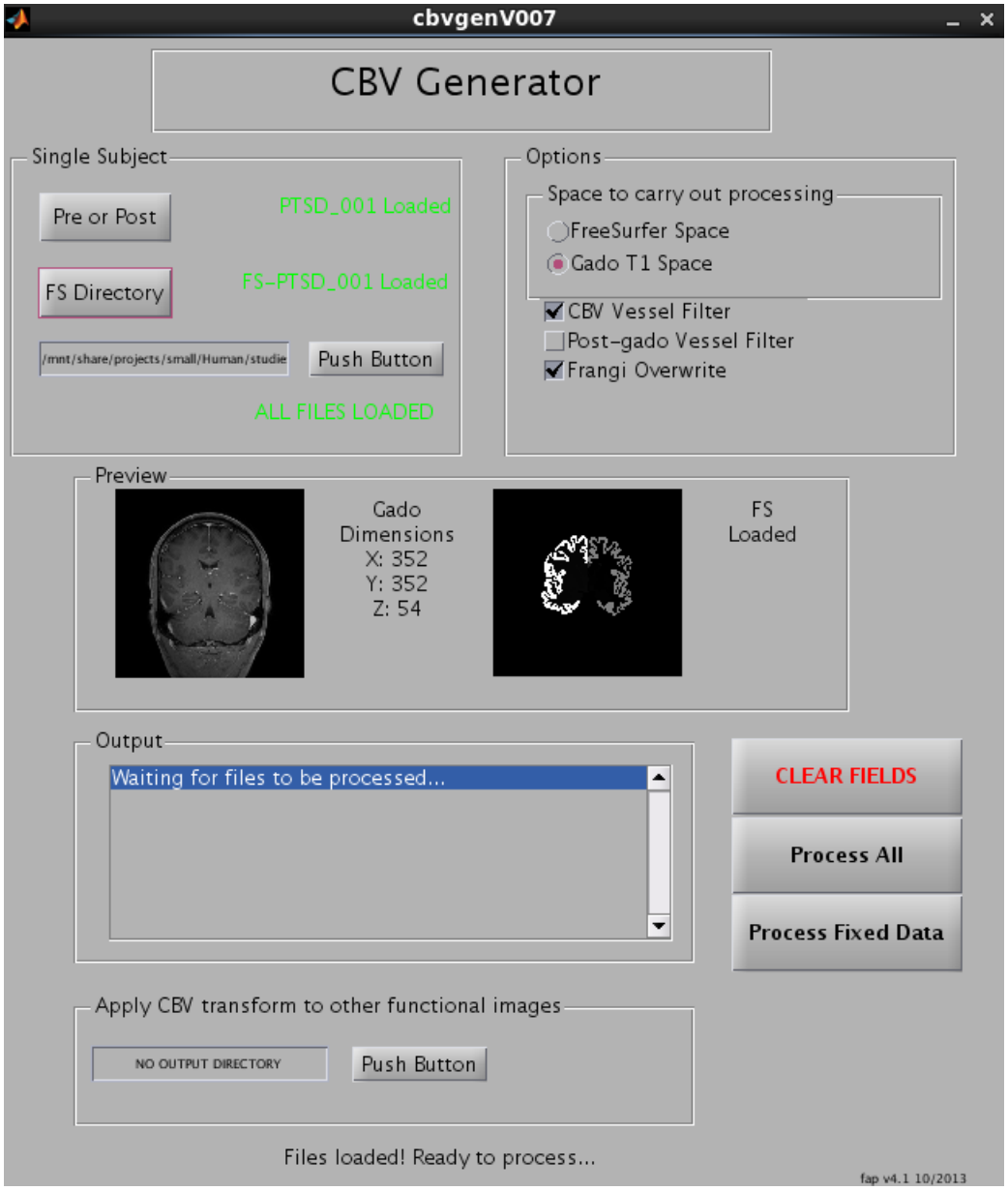

Figure 2-29: The collection of scripts are shown in the final CBV program container, written for Matlab. This program requires the input of a structural T1 weighted image and a pair of pre and post contrast gadolinium images and will generate all necessary images for ROI or VBA analysis.

2.4 Examination of the effects of bias field

2.4.1 Introduction and study design

MRI acquisition is subject to several types of artifactual concerns previously mentioned. [72, 4, 5] Some relate to environmental (such as radiofrequency (rf) noise), magnet inhomogeneities, subject specific (e.g. accumulation of para or ferromagnetic dyes or materials inside the body or skin), session specific (e.g. movement artifacts) or acquisition specific (e.g. aliasing). Repeated scans can improve the detection in contrast enhanced MRI, and any machine influence that would impact multi-site studies might be reduced by having repeated sequences.[102] Although many studies use dynamic contrast enhancement, the steady state method of CBV analysis uses only two sequences prior to and after a steady state of contrast equilibrium has been reached.

2.4.2 Methods

In order to standardize and measure bias field, we first extracted a brain mask of one of several randomly selected images within our studies. All MRI images go through a cursory inspection to ensure that gross or prohibitive scan issues are addressed.

This is usually performed by a trained MRI technician, however experience within our scanner has shown us that not all types of artifacts can be adequately identified prior to pre-processing.[88] These artifacts we have discovered to be most often motion and bias field.

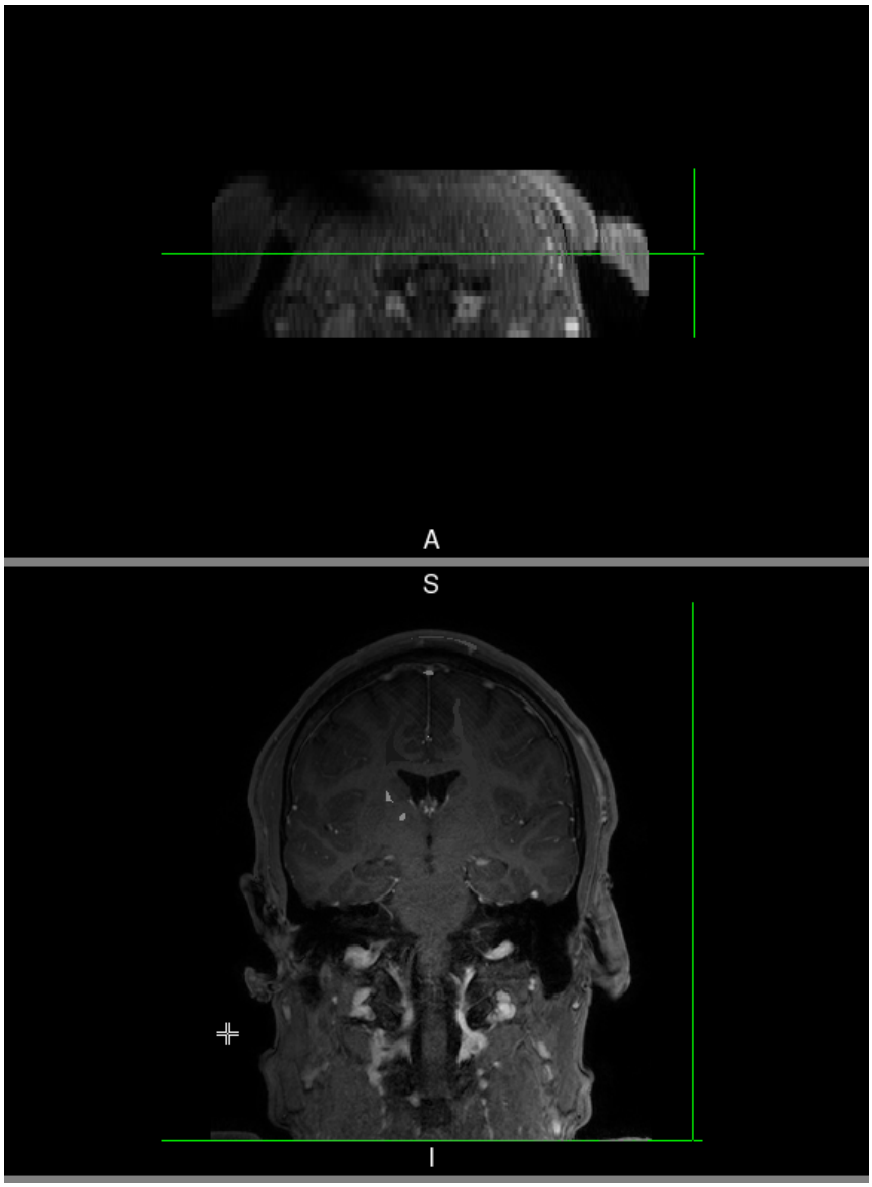

Figure 2-30: An example of bias field artifacts are shown here. Note the upper left corner of the top figure, and the left side of the bottom figure. One can easily see the dampening in signal intensity that can be potentially problematic in both clinical and research uses.

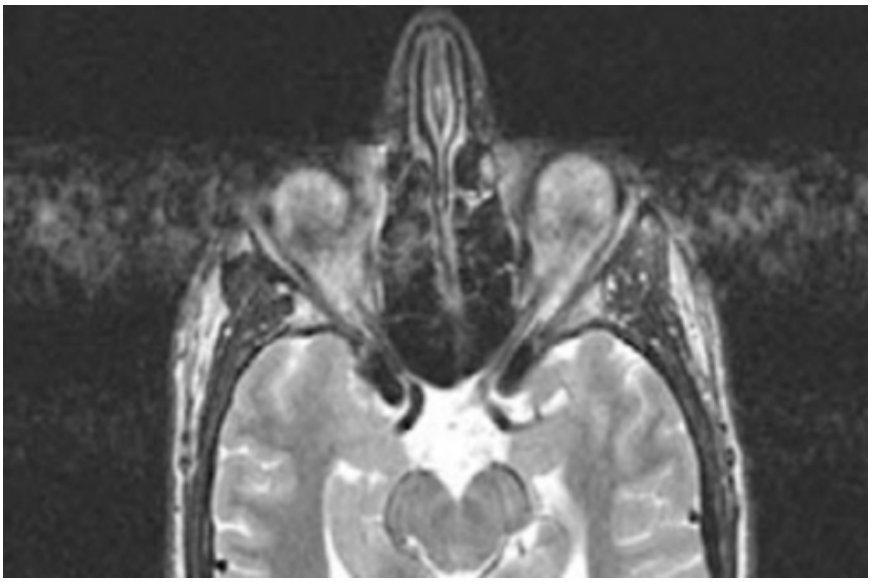

Figure 2-31: Artifactual errors seen due to high signal in the eye, indicative of a PE artifact in the left-right direction. It is possible that non-visible artifacts may artificially dampen or increase signal elsewhere parallel to the plane of the PE direction, and as such, represents an image that would most likely be excluded from CBV analysis.[61]

2.4.3 Results

Upon investigation of subtracted bias field images on pre and post contrast weighted images, maximum field error is roughly two orders of magnitude lower than single image bias field. These focal areas of bias field subtraction align with areas of high signal from GBCA accumulation. It is unlikely that the result of the bias field is in fact from the GBCA impacting the local field around the T1, and that if it does, it is on the order of 10^{-2}, which are unlikely to adversely affect our signal, if at all. Another issue is the calculation of bias field in contrast enhanced images. It is possible that the techniques by which BFE is calculated are failing to account for the differences that punctate enhancement cause, and as such would be intepreted as a higher BFE. One prospective method that should require further investigation is the extraction of

epicortical vasculature followed by BFE estimation. Similarly, an analysis of BFE on the subtracted image (which would join errors) might also prove helpful (since that is the only image where a diffuse field effect might impact quantization of signal.

2.4.4 Conclusion

Although BFE contribute to local field inhomogeneities that may impact measurements from unique scanning acquisition to scanning acquisition, it does not appear as there are BF correction algorithms in place to detect and correct the unique contrast enhanced effects present in exogenous contrast pair CBV scans. Additionally, by subtracting, the only detectable BFE field effects are the result of the BFE estimating high values near the areas of increased signal. It is more likely that the *difference* in BFE is the result of poor BFE techniques and not contributing to an effect in this dataset, but merits further exploration into techniques agnostic (or perhaps incorporating) the subtracted image maps .

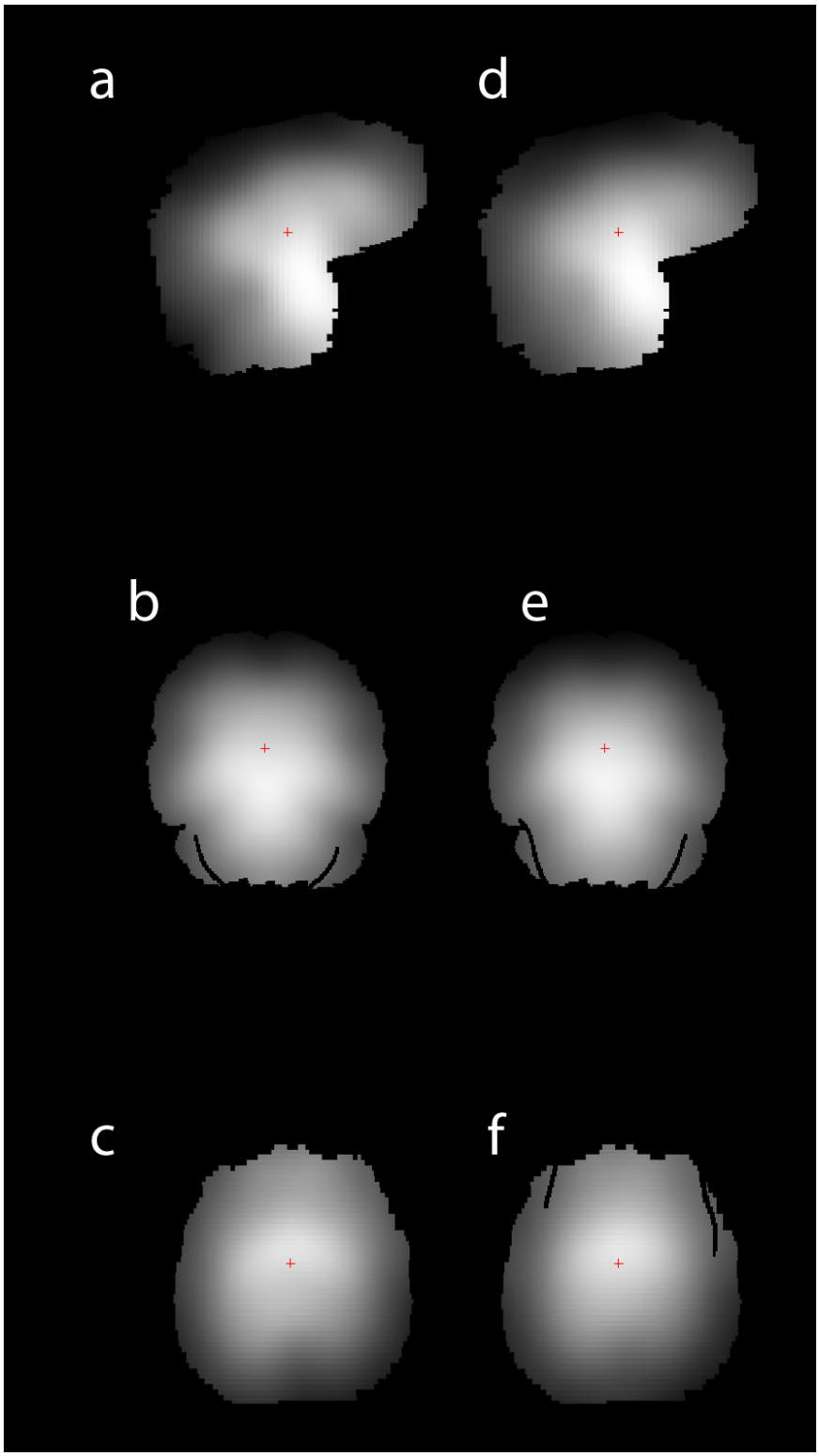

Figure 2-32: This image represents orthogonal views of the bias fields generated from both the post contrast image and the pre contrast image. The brain has been extracted prior to both of these analyses.[103] (a,b,c) Sagittal, coronal and axial view of the post-contrast image bias field maps and the (d,e,f) pre-contrast image field maps.

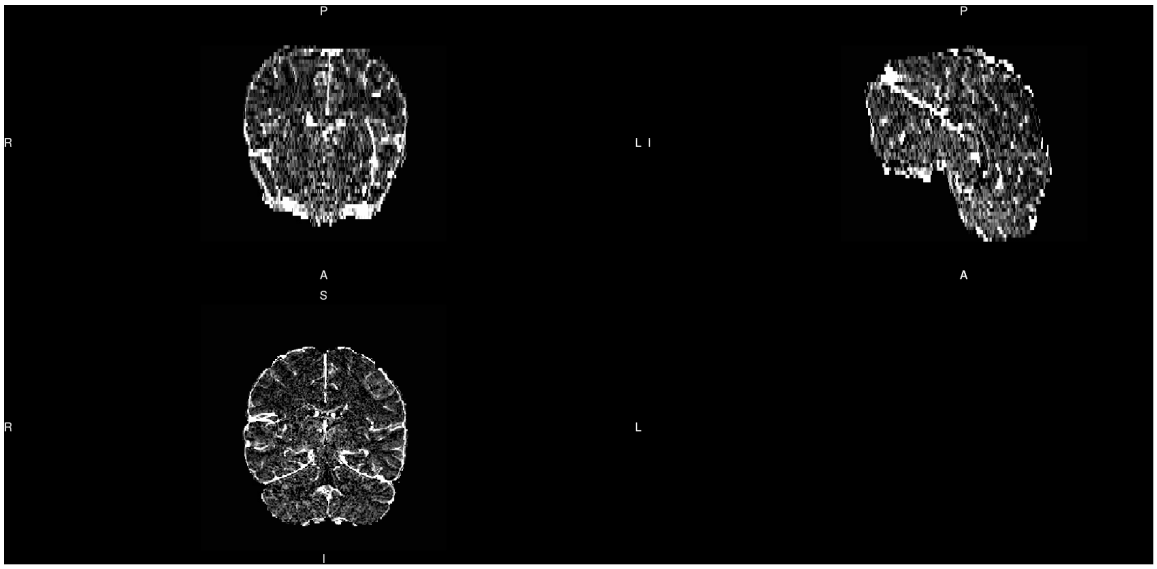

Figure 2-33: Brain extracted CBV image is shown in three orthogonal planes. The marked brightness occurs in regions with large macrovasculature.

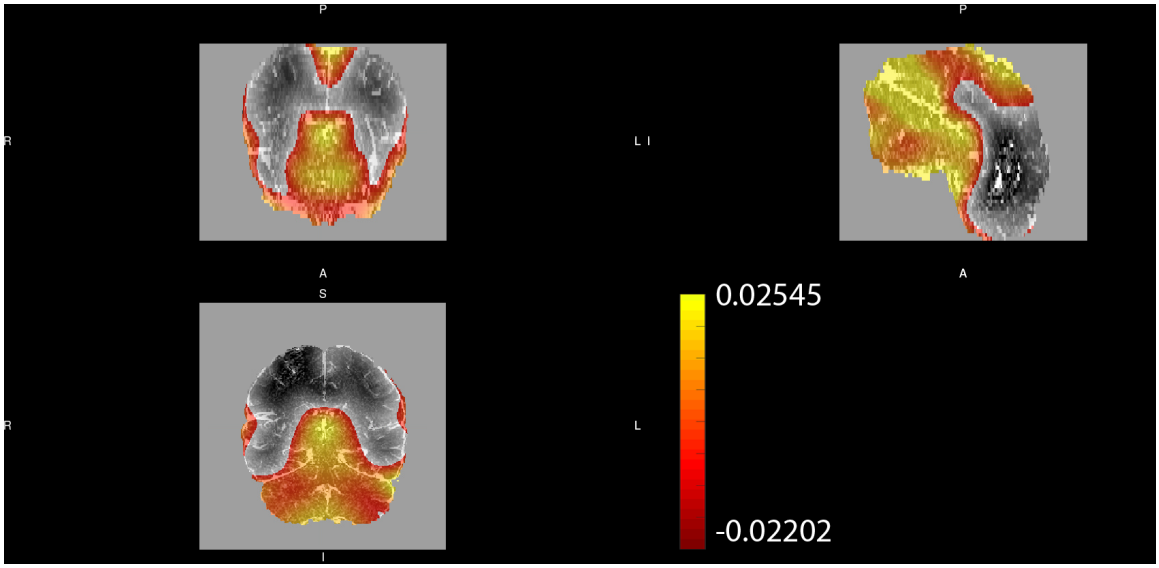

Figure 2-34: The subtracted bias field image (of *post* - *pre*) is shown overlaid with a 60% opacity on a subtracted image

Chapter 3

Apply CBV techniques on high-risk for conversion to psychosis dataset

3.1 Create a broad based population template onto which we can isolate and identify anatomical and canonical defined regions

3.1.1 Introduction and study design

Many psychiatric and neurological are structurally and morphologically identical on MRI or CT in early stages and change during advanced stages. Volume changes within the gray matter reflects an etiology that that may lead to such a change, not only

in AD, schizophrenia but also similar diseases like bipolar disorder.[17] The earliest stages of bipolar disorder and prodromal psychosis can often present with similar pathologies, the so called “Kraepelinian dichotomy”. Although fraught with issues, both disorders have been associated with structural hippocampal abnormalities.

In mid 2015, two studies featured the structural analysis of multi-site coordinated imaging projects of controls and both schizophrenia and major depressive disorder (MDD).[93][79] Hippocampal volume changes were observed in both studies compared to healthy controls, implicating a greater involvement in the hippocampal network in these diseases.

Additionally, in Alzheimer's disease one component leading to volume change can be attributed to neurofibrillary tangles, or clumping of proteins that attach to and maintain the structure of microtubules, called tau. Clumping of these proteins (as measured with histology) greatly reduce neuronal tone and shrink effective sizes of gray matter in targeted areas, specifically the hippocampal formation (hippocampus and entorhinal cortex). I along with our group have tried to examine and track these volumetric changes irrespective of other potential burdens to see how they correlate with disease diagnosis or other factors. Specifically, I wanted to test the creation of an appropriate atlas that might provide per-patient single-scan volumetric data that might provide value to later diagnosis.

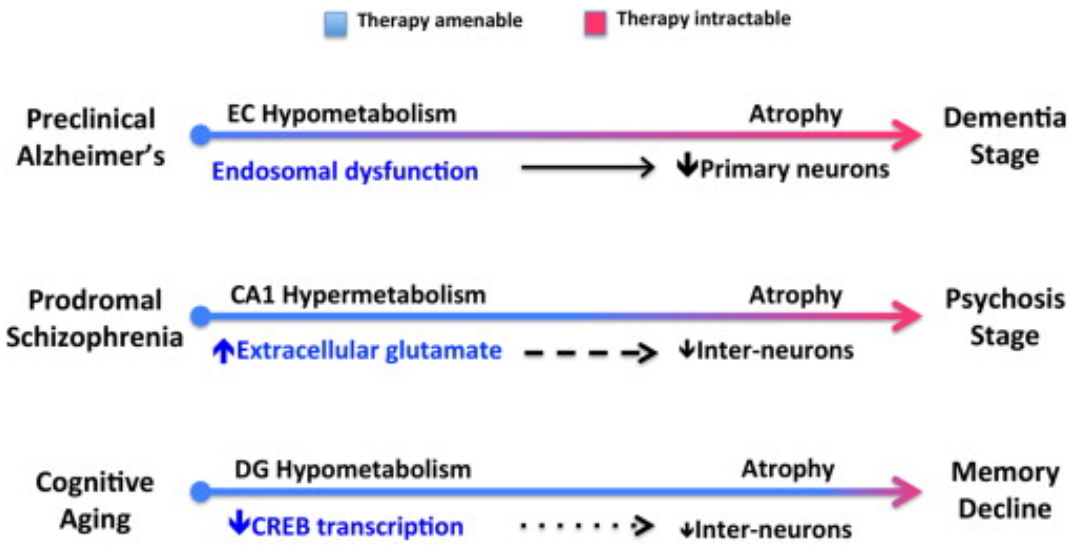

Figure 3-1: An example of disease progression as a function of impairment on the cellular level in schizophrenia[83]

3.1.2 Methods

Template atlases for brains require several features: they must reflect an accurate portrayal of the groups onto which they should be applied, must have no particularly asymmetric or out of place features and must be all of appreciable scan quality and acquisition. Two templates methodologies that address concerns of sampling and variety in normal and somewhat changed brains are varied in the archetypical approach or the population approach. In the archetypical approach, the idea is to find a brain that represents an average brain, without averaging artifacts to reduce tissue class segmentation partial voluming. An example of this brain atlas type is the '11colin" brain from Montreal Neurological Institute. The "colin" brain represented a single subject imaged 27 times using the same sequence and scanning protocol.[86] The sequences were co-registered and averaged. The strength of this atlas is to preserve

anatomical absolution while reducing scanner noise. An alternative is the MNI 152 (or 301).[17] These represent identical sequences on either 152 or 301 different brains that are also averaged. The result reduces the fine spatial information for a better template procedure, whereas the colin27 brain is subject to any particular morphological changes inherent in that one patient's brain. For our study we wanted to use a diffeomorphic technique to generate this atlas in a 54-person data set with the existing CBV protocols. Diffeomorphic atlas registration allows for local shape changes to be preserved

3.1.3 Results

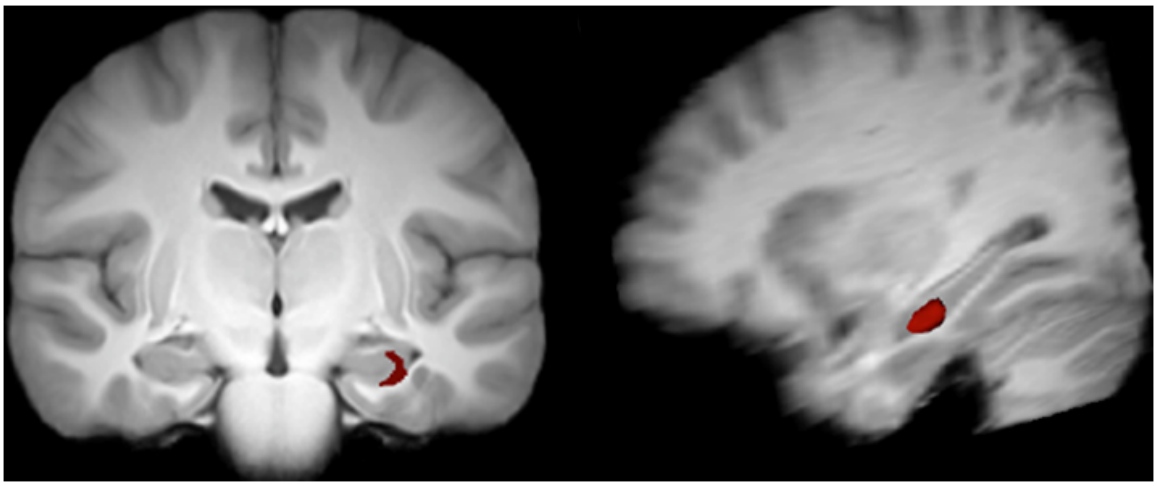

Figure 3-2: An example of a functional template brain and the region of interest we wish to test, specifically the left anterior CA1 of the hippocampus

Diffeomorphic co-registration was able to generate a T1 weighted image that could clearly define the hippocampal subregions and eliminate any medial temporal abnormalities upon visual inspection. A trained rater was able to delineate a portion of anatomy (in this case, and what will be defined later) the anterior portion of of the

CA1 of the hippocampus. Any image that is co-registered to this map will have this region as defined by a symmetric co-registration procedure. Each of the 54 images were checked with a 'yes' or 'no' rater metric to ensure the ROI was within the CA1.

3.1.4 Conclusions

The purpose of this arm of the study was descriptive and categorical, since there is no 'canonical' CA1 ROI based on Schobel et al's work that a user was trained to draw on new datasets, only the fact that the ROI successully encompassed a region on a new image that is considered the same that is found in the paper. Further studies should examine forward application of CBV results in a template space to refine those regions.

3.2 Test forward application and accuracy of template to functional CBV images

3.2.1 Introduction and study design

Canonical regions are not necessarily pathologically or etiologically the regions where a disease is though to occur. Although canonical regions often overlap, in the hippocampus, if a disease is thought to occur in a particular region, then that region ought to be tested irrespective of how it is defined either pathologically or structurally. Santiago Ramon y Cajal, thought to be the founder of modern neuroscience, defined canonical regions and layers of the hippocampus as delineated by fiber pro-

jections, histology and pathology.[73] Individual template registrations use several different methods to identify regions based on a priori population templates drawings and such voxel labeling methods as hidden markov random fields (HMRF). However, disease locus may not include canonical labeling constructs. CBV has been used for neuro-oncological purposes irrespective of BBB integrity to determine CBV changes in response to chemotherapeutic or surgical intervention. These CBV values, however, are germane to only instances where accumulation of contrast agent is much higher than structurally comparable brains, and reflect grossly abnormal malignant tissue, with an entirely different range of angiogenic contrast uptake values. Therefore SNR thresholds that may preclude structural (T1 weighted) MRI brain scans for our population based of neurologically and psychiatric analyses are not expected to present with radiologically identifiable alterations. This is not true for brain tumors, such as glioblastoma multiforme (GBM), where CBV values are often used to determine extent threshold of blood supplies and cortigraphy. Since the region of interest for certain diseases is focally localized but not limited to a particular canonical region, we need to determine which region, based off of parametric or slice-by-slice analysis that allow for accurate forward application, i.e. inform a hand drawn region of interest on existing findings anatomically and take the union of a group of those regions on a template to find the best match.

As such, we wish to strengthen our template overlapping on the co-registration and atlas, instead of other regional devices.

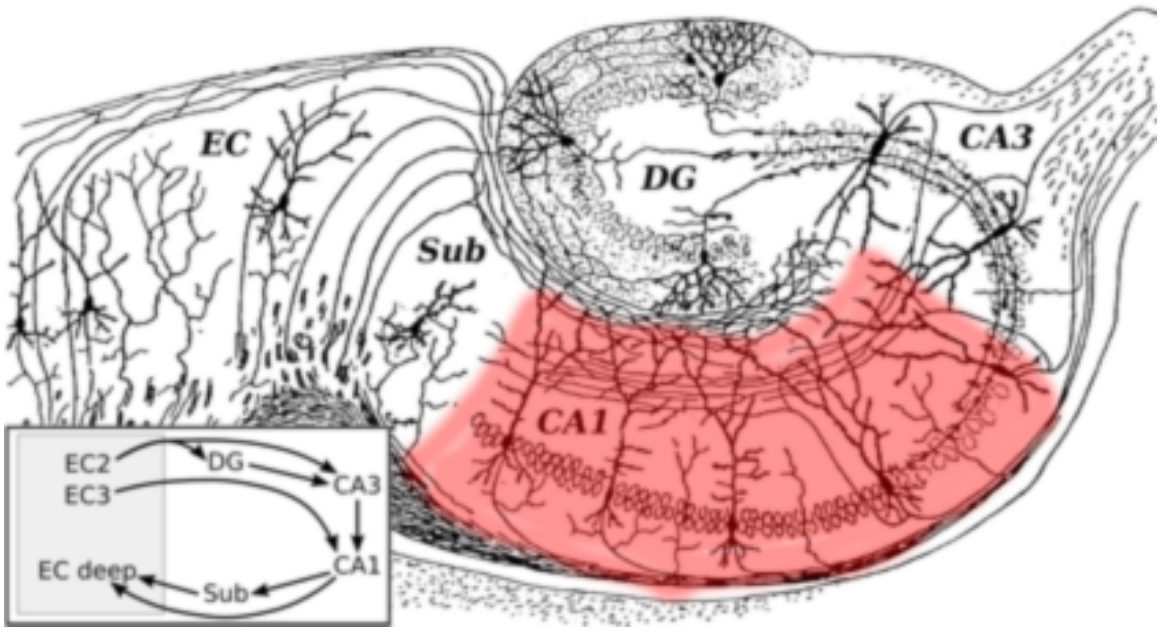

Figure 3-3: Drawing of the hippocampus as edited from Santiago Ramon y Cajal which delineates subregions[73]

3.2.2 Methods

Having developed the previous methodology, we test overlapping metrics of different sized ROIs compared to hand drawn ROIs in the sample database and test the overlap. We will generate a template from a mixed subject and control group space with no identifiable structural abnormalities. Structural aberrations in the hippocampus have been shown to be present in cases with responsible confirmed diagnoses of schizophrenia (i.e. 12-18 months of psychiatric evaluation), however in wanting to address all possible variations of these patient populations we expect a larger number of patients to be included in this population template. Our steady state CBV method is unique in that the functional alterations do not impart any partial voluming difference compared to the structural image. In BOLD, very few acquisitions can reveal structural detail required to define small regions. Since the CA1 comprises a "C" shape of

roughly 1 cubic centimeter in patients, cubic interpolation would average signal and include the suspected spared dentate gyrus region. We wish to compare hand-drawn CA1 in patients with the co-registered images with generated co-registered images with population derived ROIs.

3.3 Demonstrate CBV changes in humans in a new prodromal psychosis population with forward application of CBV ROI

3.3.1 Introduction and study design

Our lab has previously produced existing findings in human CBV dysfunction driven by suspected glutamate alterations[80] which have additionally been replicated by an outside laboratory[90]. In short, these findings predict elevations in ssCBV in the left anterior hippocampus (encompassing the CA1) in patients with prodromal psychosis and schizophrenia. Other studies have examined CBF changes in male schizophrenic patients and have found lateralized aberrations in the left temporal area during an auditory task.[40] This may correlate to suspected increases of glutamate focal to the same region, and the potential value of potential glutamate reducing agents in ameliorating positive disease symptoms. We wish to use a CA1 ROI (whether hand drawn or automatically applied) to determine whether this region can provide a sensitive and specific measure to determine prodromal patients from CBV scanning alone.

The success of this would be t-test significance and appreciable ROC compared to other ROI regions. The advantage of ssCBV compared to dynamic T2* weighted image or DSC acquisitions is whole hippocampal circuit acquisition and the ability to differentiate whole circuit subfields (i.e. CA1, CA3, subiculum and dentate gyrus)

3.3.2 Methods

Using Cerebral Blood Volume (CBV) fMRI, we have previously reported that selective hypermetabolism in the anterior CA1 region of the hippocampal circuit occurs in prodromal stages of schizophrenia and related psychotic disorders. To date, a manual approach was used to generate CBV maps of the hippocampal circuit. This approach is time consuming and introduces sources of noise. To address these limitations, over the last few years we have been developing and optimized an analytic toolkit that generates CBV maps of the hippocampal circuit in an automated fashion. Here, we show this toolkit and test its ability to detect anterior CA1 hypermetabolism in prodromal stages of disease. Recruited patients who are at an at-risk state for conversion to pyschosis (N=50) and controls (N=16) underwent a series of identical MRI scans on a Philips Achieva 3.0T MRI scanner, including a structural T1-weighted image (1x1x1 mm) as well as two T1-weighted scans (.68x.68x3 mm), acquired in the coronal plane along the long axis of the hippocampus prior to and after a bolus injection of a GBCA. The at-risk group eligibility is determined by positive symptoms detected through an established inventory.[55] Of these patients, roughly 1/3 are predicted to convert to Schizophrenia within 24 months whereas the remaining patients are generally given

other related diagnoses, such as schizoaffective disorder. The aforementioned 'best' template methodology (either automated or hand drawn) is to be applied and tested.

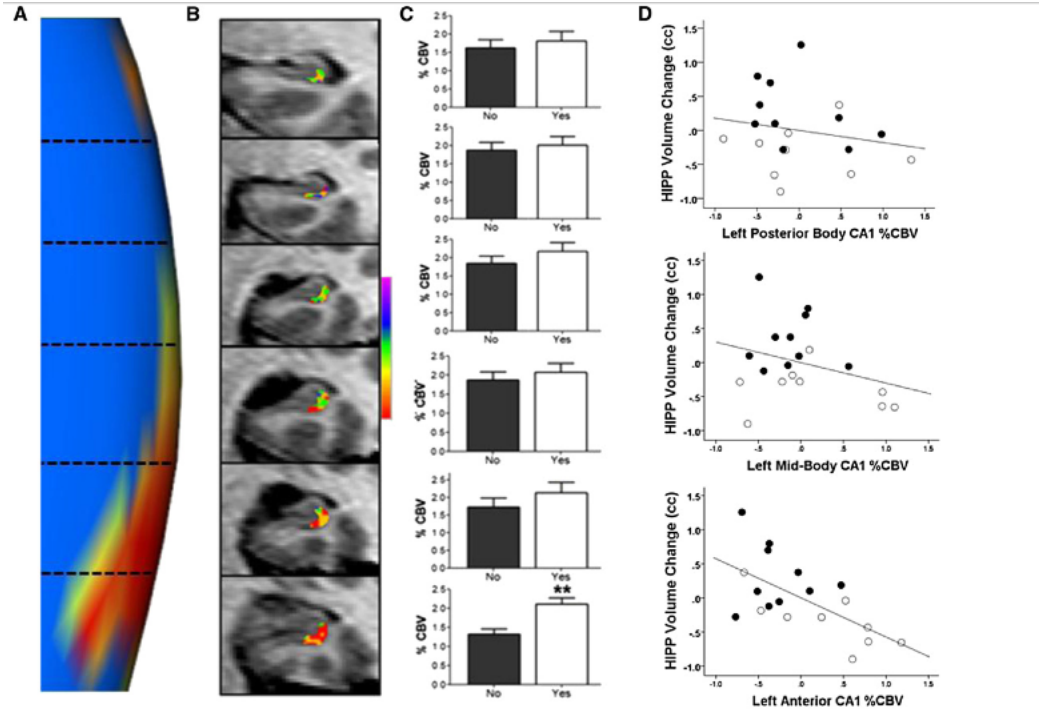

Figure 3-4: Findings from a paper which used a manual/per slice region of interest analysis [17]

3.3.3 Results

Our software was able to generate CBV maps for each patient and apply the template drawn ROIs to template co-registered CBV. Mean value differences reveal a significant increase in CBV signal, concordant with extant literature, in the prodromal group versus the age matched controls. By detected anterior CA1 CBV elevation, we can hypothesize that elevations in CBV are correlated to increased basal metabolism. For a sample of 66 age matched patients (50 prodromal psychosis 16 healthy controls) a two-tailed t-test revealed a $p<0.003$, whereas no area in the anterior hippocampus

exhibited any alterations. Achieving this goal is important if CBV-fMRI is to be applied in different research centers if the focus of interest if investigating hippocampal circuit may help elucidate disease state. Additionally, an automated toolkit is required if CBV-fMRI will turn out to become a biomarker of prodromal schizophrenia, as we are currently testing, and potentially used in clinical trials.

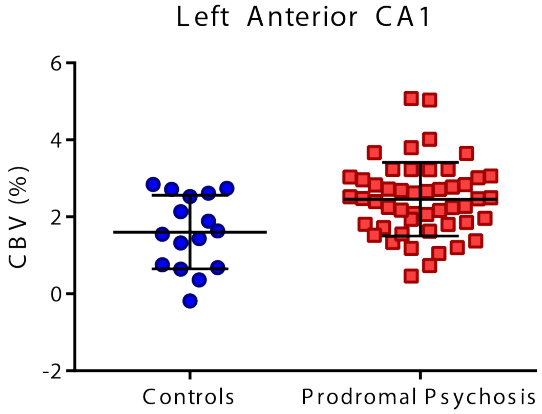

Figure 3-5: Preliminary results from CBV ROI study. Independent samples t-test is significant at $p<0.005$ not assuming equal variances.

3.3.4 Conclusions

It appears as though upon an initial fairly low-N study that this CBV toolkit demonstrates results concordant with existing literature, as in a increase in mean CBV sensitive to only the anterior CA1 of the hippocampus in patients in an at-risk group. Given this finding, it merits further exploration of our methods and techniques on a larger scale to further validate this as well determine repeatability and reliability in our studies.

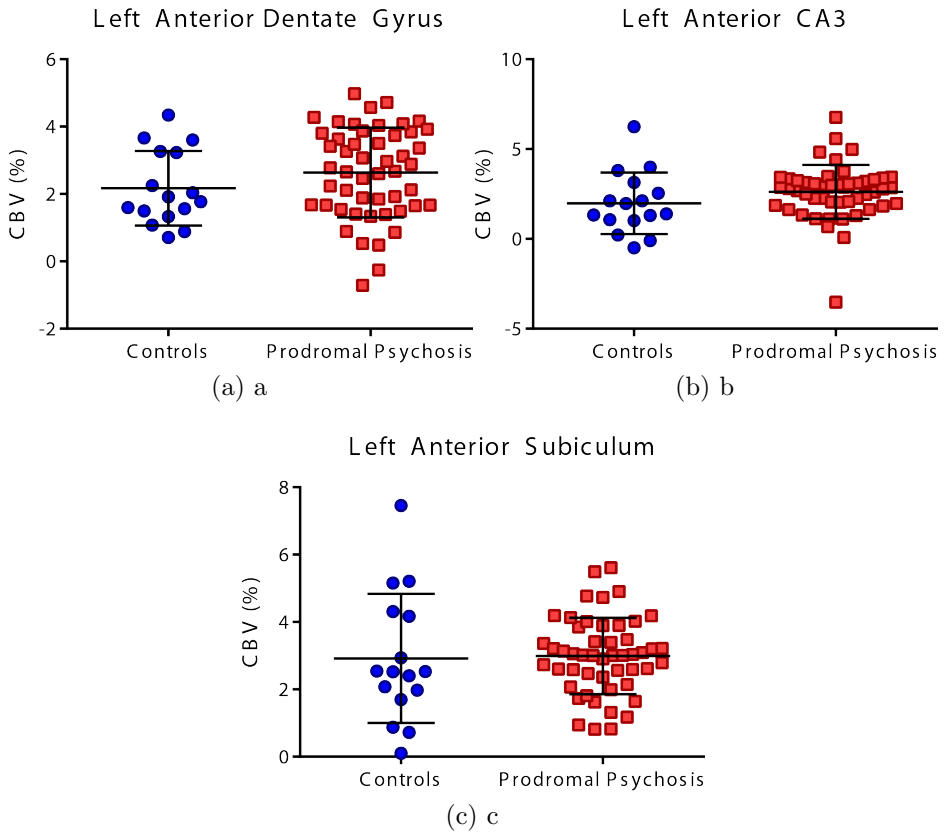

(a) a

(b) b

(c) c

Figure 3-6: (Left anterior (a) dentate gyrus (b) CA3 and (c) subiculum mean CBV value in a group of controls and age-matched patients at high risk for psychosis. Independent samples t-test is not significant at $p<0.05$ not assuming equal variances.

Chapter 4

Examining utlility of functionally derived results on structural images

4.1 Examine CBV and volume in Alzheimer's disease

4.1.1 Introduction and study design

Hippocampal grey matter volume loss in Alzheime's dementia is a well-known structural change that occurs in advanced stage disease. Aβ, both CSF and cerebral, WMH, specific neuropsychological dysfunction are also established markers of disease state, but with varying severity and metrics.[14, 12, 11, 13, 10, 15, 99] However, vol-

ume loss indicates a heretofore-irreversible pathological disease state with little known potential amelioration.[87, 6, 81, 41] In a previous study I have shown that amyloid deposition and regionally defined PiB PET positivity (as 1.5< mean PiB SUV) to be "necessary but not sufficient" in characterizing Alzheime's disease in a patient[71]. However, the exact mechanism and relationship of amyloid deposition is still not well defined in the earliest stages of AD[18].

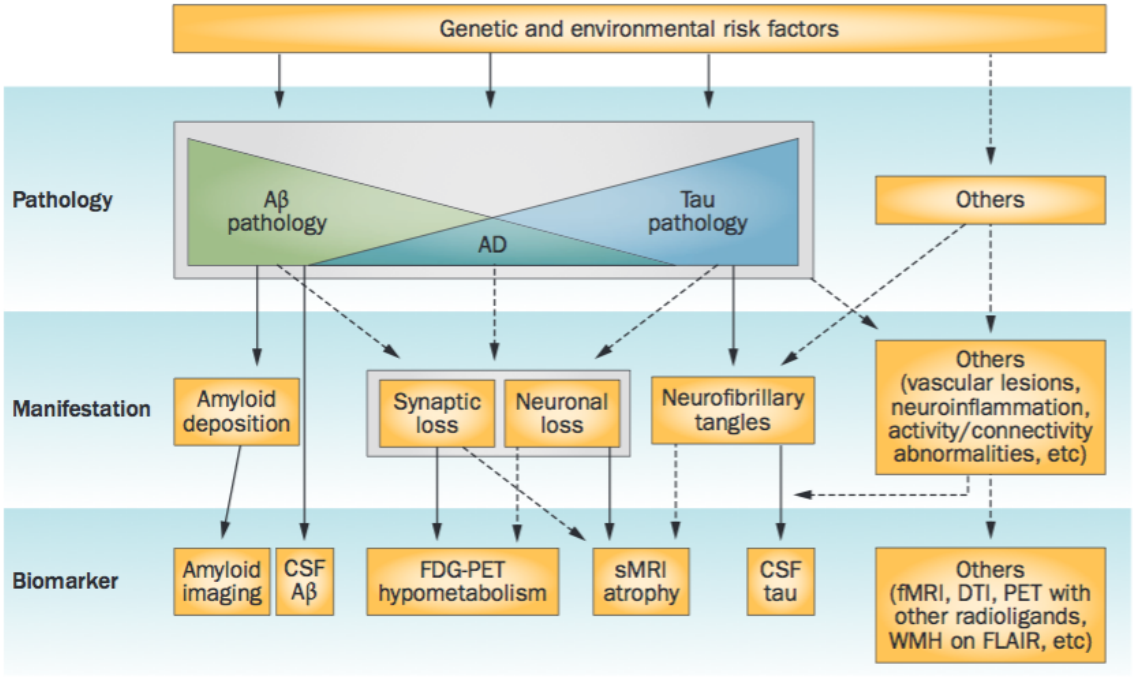

Figure 4-1: Established athologies in AD along with the biomarkers that can be used to discriminate between the various blood, neuropsych and imaging markers.[18]

Although the utility for A β imaging exists for neurologists, A β *positivity* is not particularly useful in sequestering patients with "preclinical" (i.e. patients who progress to a confirmed AD diagnosis within 3-5 years) Alzheimer's disease and those who have a different form of dementia such as LBD; however, it is useful in excluding Aβ negative patients with FTD.[59] We showed changes in CBV in the area known

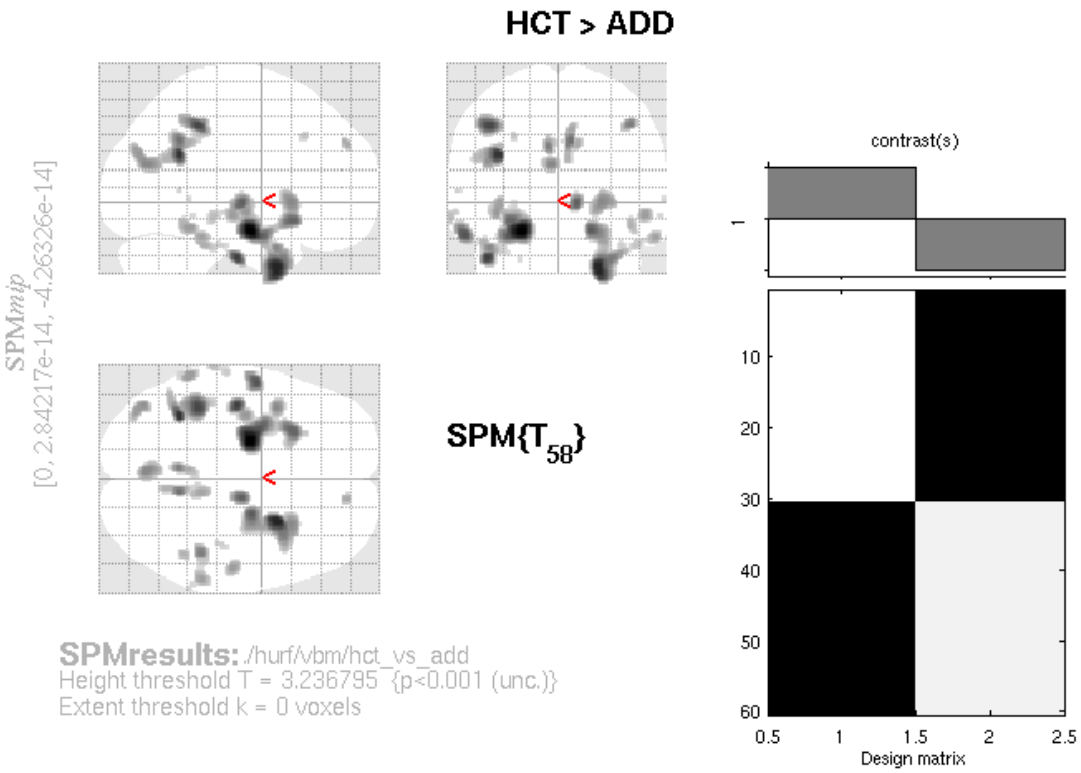

Figure 4-2: VBM analysis of age-matched controls and AD patients in the ADNI dataset. Voxel-level significance at p<0.001 reveals several clusters, many of which pass cluster level significance statistical threshold.

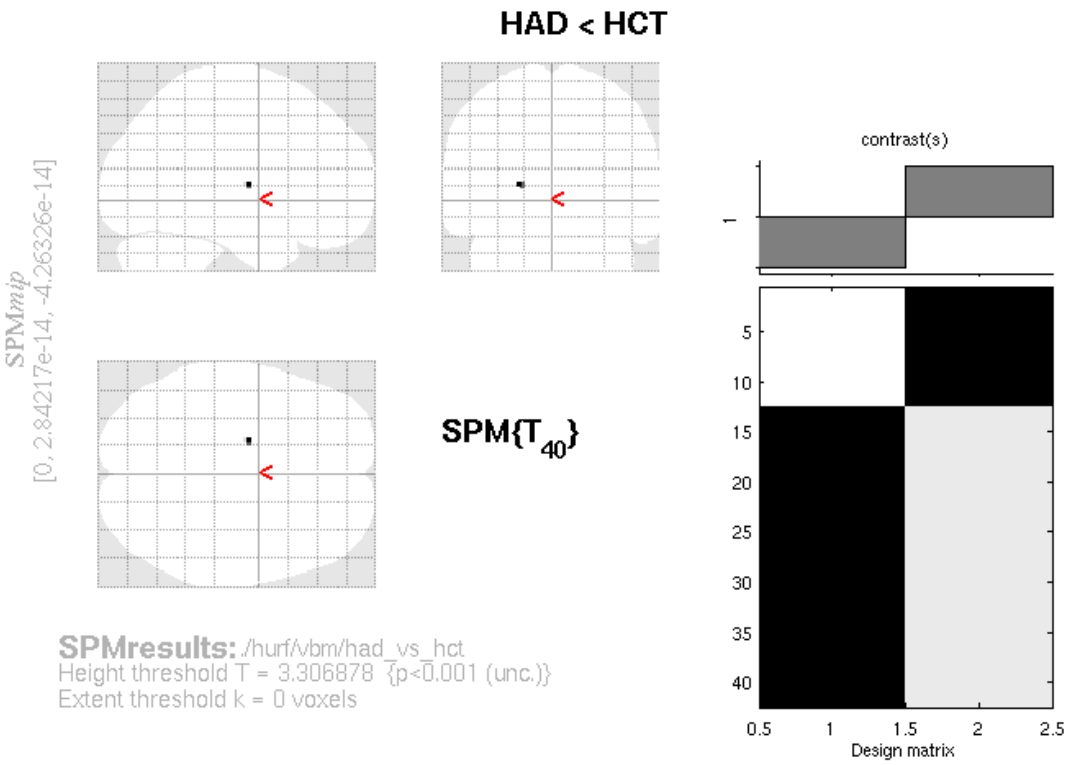

Figure 4-3: VBM analysis of age-matched controls and controls who convert to AD within 36 months in the ADNI dataset. Voxel-level significance at $p<0.001$ reveals one small cluster that does not pass cluster-level significance.

as the lateral EC (sometimes referred to as transrhinal cortex) concordant with early Braak staging findings in both preclinical human AD and animal models with AD pathology[9].

It would behoove clinicians to determine a timeline or appropriate curve fitting procedure to assign structural or functional changes to the HC along with suspected disease state. What we hypothesize is a hippocampal volume reduction being driven by dysfunction in the lateral EC. We would like to determine which region (either canonical EC or our parametrically derived lateral EC) is most sensitive in predicating conversion to AD from a categorically healthy state. To do this, we will use big-data neuroimaging initiatives (ADNI and NACC) with acquired structural images and our own datasets WHICAP (Washington Heights Inwood Community Alzheimerś Project) to establish expected variances according to age and potential disease progression.

4.1.2 Methods

We want to confirm structural changes in a sample population of patients and localize these changes. Well known structural changes have been identified in the medial temporal lobe which follow the known etiology of Alzheimer's disease. Additionally, the posterior parietal lobe has also been well established as a cite of structural and functional impairment in disease state that might otherwise be structurally identified as normal.[56] These well known features core to the disease state are to be proven in a subsection of well-characterized adults in the ADNI dataset. One hypothesis we test

is that functionally derived findings from a voxel based CBV analysis might be more sensitive in detecting early disease state when compared to structural findings. CBV imaging presupposes that cerebral tissue tone changes occur following a reduction in vascular perfusion and availability. Whether this reorganization occurs as the result of angiogenic mechanisms resulting from synaptic pruning or other causes, there should be a change in the GBCA subtracted image due to local overal Gd^{3+} concentration differences .[95]

We then test on a new dataset the positive predictive value of gray matter volume per-patient in this structurally (VBM)-derived ROI mask, our functionally derived parametric ROI mask and a standard hippocampal ROI mask.[30] SPM8 will be used to perform tissue class segmentation. We predict healthy controls to AD converters to have no significant baseline structural abnormalities (isometric T1 weighted 1x1x1mm3) at baseline as measured through a standard voxel.

4.1.3 Results

We performed two primary VBM experiments in our ADNI groups to replicate known dysfunction and to test the sensitivity of possible preclinical structural changes. HC who stay healthy compared to healthy controls to convert to AD within 3 years did not reveal any structural changes in the MTL. A glass brain output of the SPM analysis reveals a small cluster that does not pass cluster-level significance testing, the results of which can be seen in 4-3. A second analysis was performed comparing the same healthy control group to patients with confirmed AD. The results are in 4-2

with cluster significances in 6.3. Several cluster level regions are noted, specifically a region wit 1315 cluster and a cluster level significance of $p<0.009$ located in the left hippocampus and entorhinal cortex. Visual inspection of the results in the glass brain show bilateral medial temporal lobe involvement with varying degrees of significance.

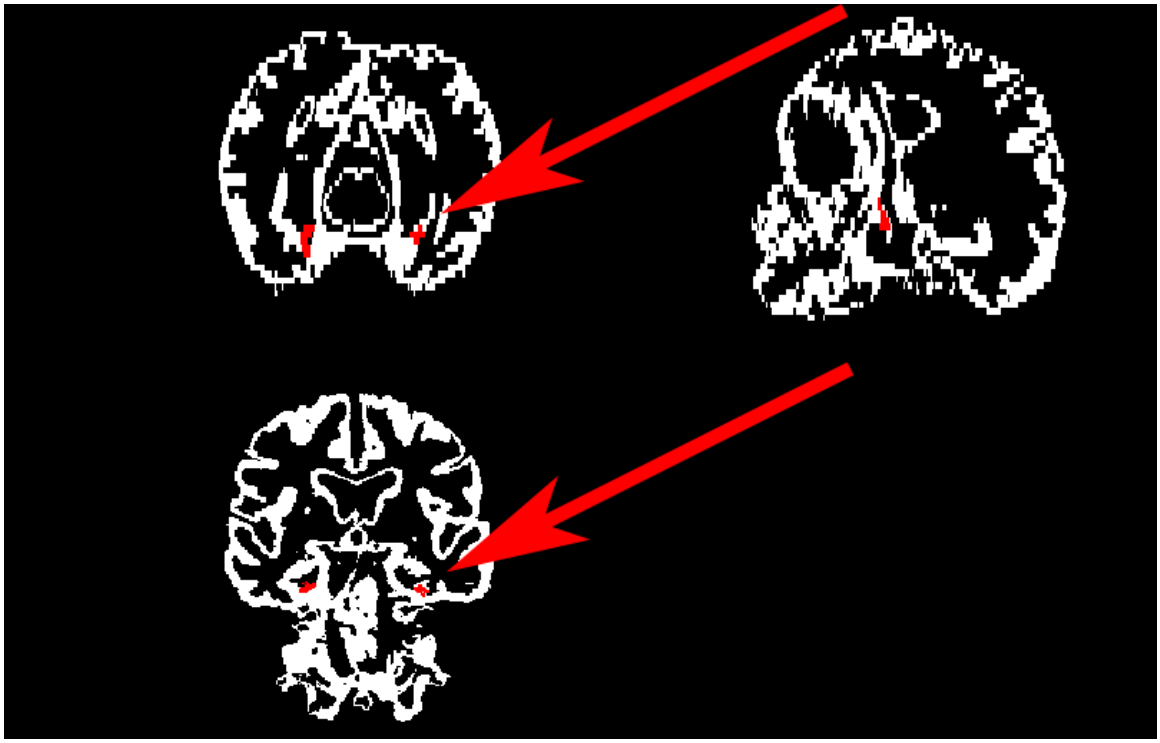

Figure 4-4: Shown in white is a sample gray matter segmented image co-registered to template space. The red arrows point to ares of red that reflect the thresholded binarized mask co-registered to the space of the image.

4.1.4 Conclusion

This analysis demonstrates a 'ground truth' for volumetric changes in two of the groups in our ADNI study. It confirms existing findings of volumetric loss in disease state, while showing no demonstrable volume loss in categorically healthy groups we know to convert to AD versus groups who do.

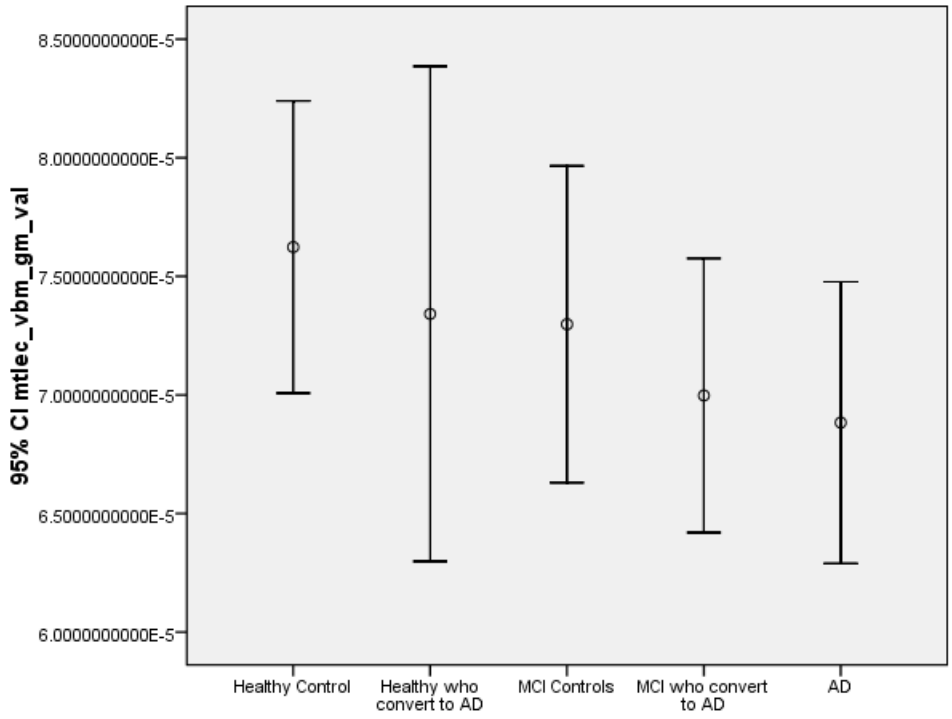

Figure 4-5: Gray matter volume in the MTRC in the five age-matched ADNI groups. One way ANOVA and pair-wise students t-test are not significant at $p<0.05$.

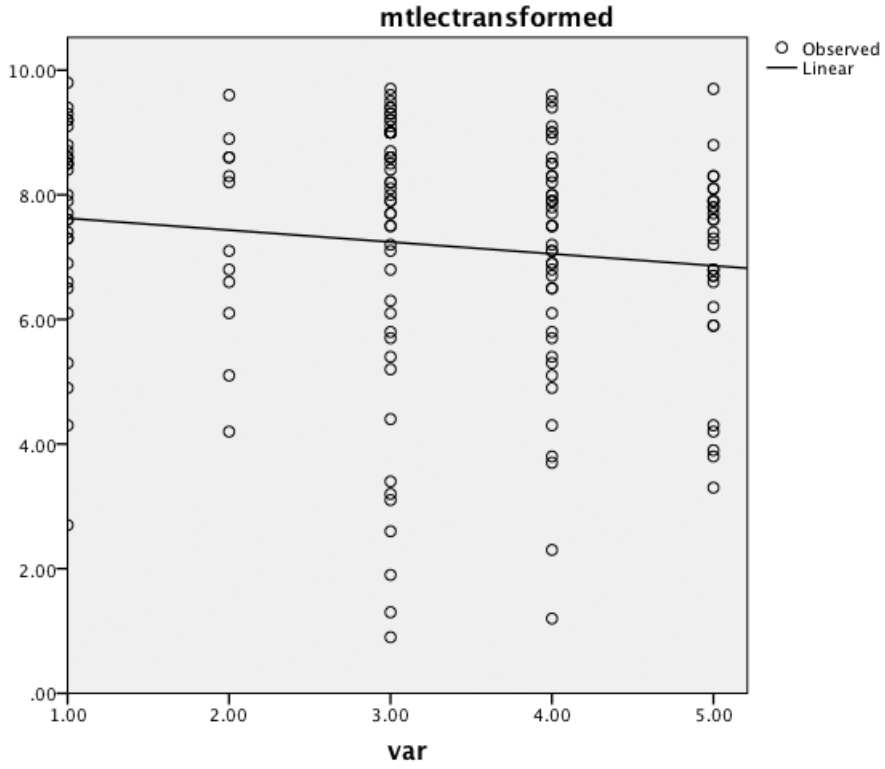

Figure 4-6: Linear regression of five age-matched ADNI groups in increasing order of potential clinical risk. 1) Healthy Controls 2) Healthy Controls who convert to AD within 3 years 3) MCI who do not convert to AD in 3 years 4) MCI who do convert to AD within 3 years 5) AD. R^2=0.017, F=2.8, p<0.096

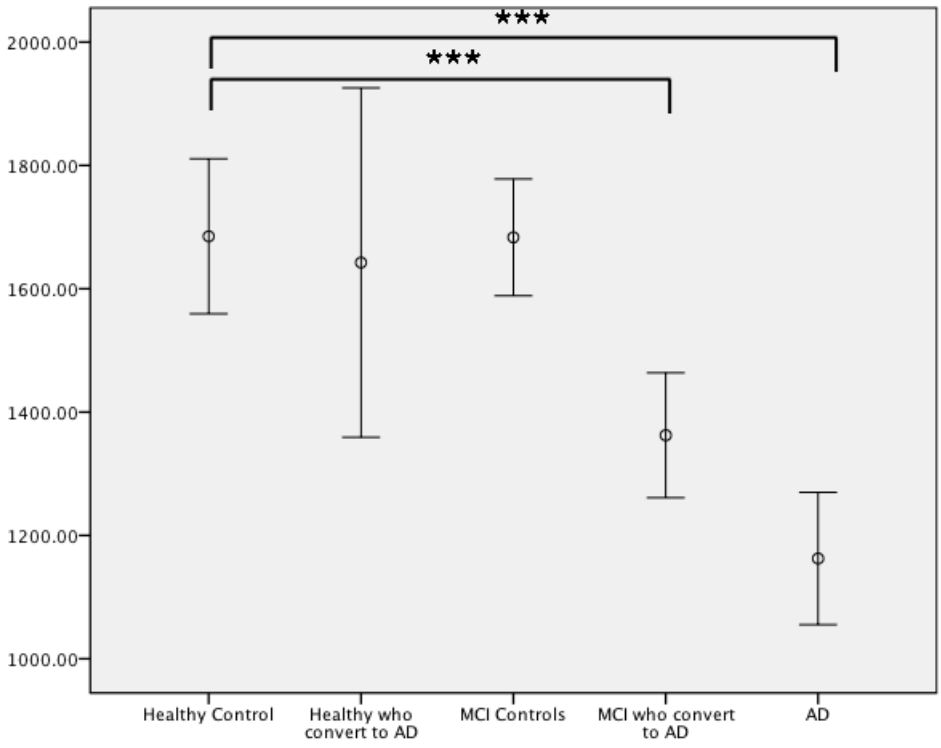

Figure 4-7: The entorhinal cortex volume (in mm^3 of five groups of subjects in the ADNI study. All subject groups were age matched. *** indicates two-tailed t-test significance. For the HC compared to AD, t=6.467 p<0.001, for the HC compared to MCI who convert to AD, t=4.067 p<0.001. The demographic and population information are in 6-9

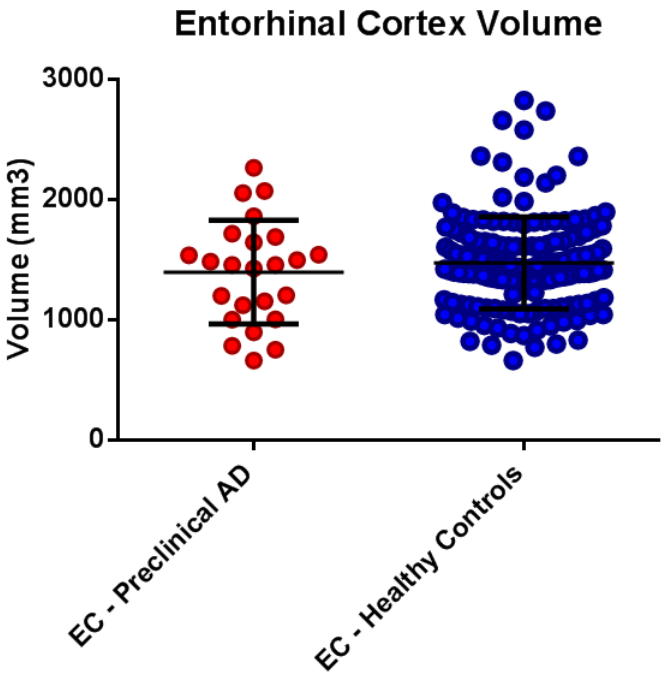

Figure 4-8: Left pane reflects predicted EC CBV value differences in preclinical AD compared to healthy controls whereas right pane reflects predicted EC volume differences in the same group

4.2 Test the postitive predictive value of forward-applied functionally derived metabolic atlases in early-stage structural MRI disease states

4.2.1 Introduction and study design

BOLD was originally lauded by psychologists without medical clearance to provide i.v. injections of contrast agent in order to determine changes in neurovascular coupling during active or resting states.[10, 31] One question we wish to explore is in disparate databases, we ca n apply functional templates of either VBM or CBV VBA to test whether those regions provide increased statistical significance in determining patient groups compared to unbiased voxel based t-testing. Such a study would permit for a system that can apply these parametrically derived regions using a specific and sometimes difficult to obtain protocol on either retrospective structural MRI analyses of varied acquisition parameters compared across various sites. Although we have processed CBV on various scanners through collaborators, several million non-GBCA T1 structural scans are performed every year in the US and present a potential valuable dataset for focal and predicted grey matter loss otherwise determined to be insignificant on a group level in preclinical stages.

4.2.2 Methods

We wish to use a large, public, sample database such as the ADNI dataset to categorize and define hippocampal change in patients. We wish to test the templates of those

particular data and determine whether our existing finding in CBV patients is more or less accurate in determining conversion of patients to AD from a categorically healthy state. We will co-register our Figure 2 findings along with findings to see which has the highest positive predictive value.

4.2.3 Results

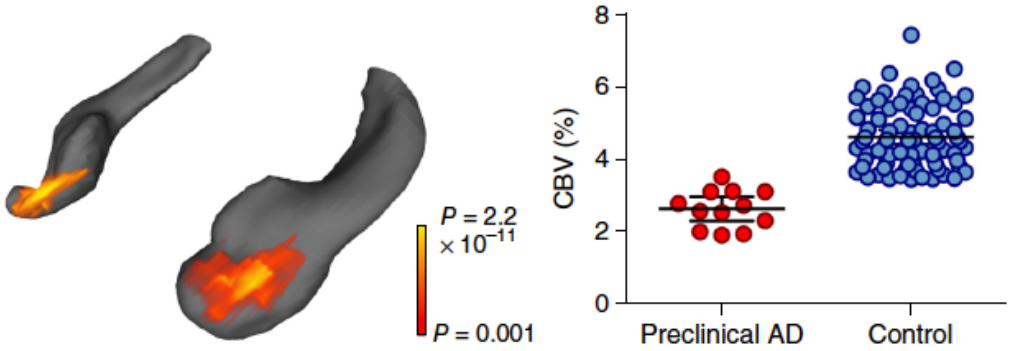

Figure 4-9: An example of a expected variance for age in a specific age group with CBV, taken from studies related to hippocampal volume changes[10]

4.2.4 Conclusion

Using the previous analysis, we have examined groups for which there are no structural deficits along with groups for which there are known structural deficits. From a temporal perspective, one can predict linearity from the stage of healthy late-adulthood through to confirmed Alzheimer's Disease, which at least three stages between the two (known healthy converters, mild cognitive impairment, and known mild cognitive impairment converters).

Chapter 5

Discussion and conclusion

5.1 Discussion

5.1.1 Specific Aim 1

We have now discussed the development of a framework to calculate exogenous contrast ssCBV from routine T1 weighted MRI images prior to and after the injection of a contrast agent. The aforementioned algorithm and technique is simply an extension of the existing manual methods that our lab had performed. In developing it, we wished to preserve modularity to allow for troubleshooting as well as allow other methods to be supplanted at any stage. This evolving algorithm has been applied to hundreds of MRI pre/post gadolinium pairs. Literature on MRI artifacts and pre-processing is procedural and generally lacking in detail with respect to scanner acquisition. Fortuitously, a wide range of MRI quality in the images we have processed have allowed us to build analytic techniques into our algorithm. Although this does so at the cost of

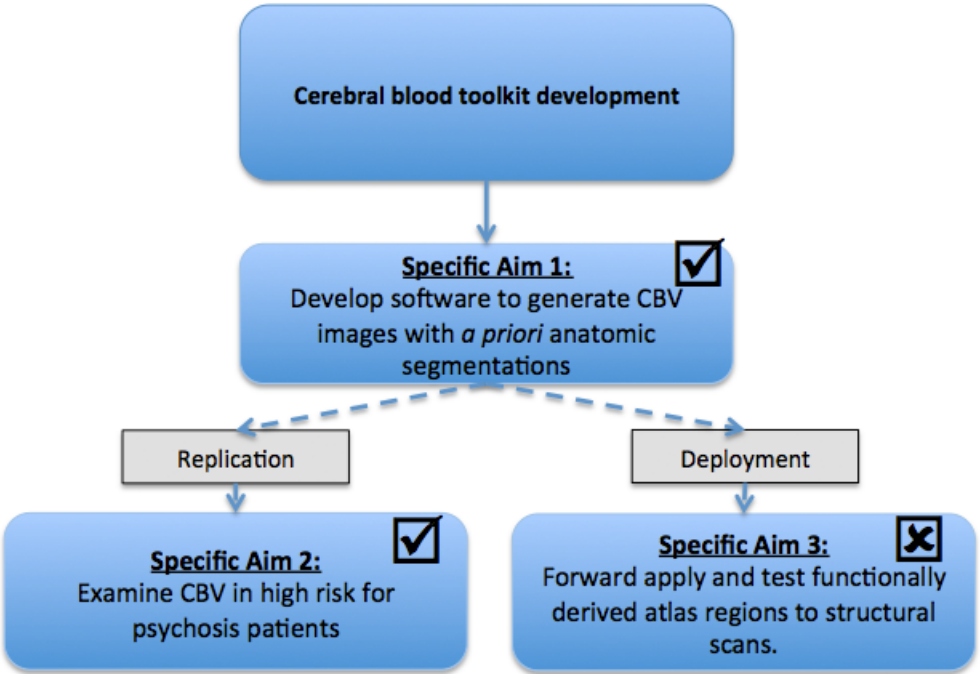

Figure 5-1: The addressed specific aims of this project. The first two aims were executed successfully, since the toolkit has been able to semi-automate the development of exogenous steady state cerebral blood volume maps, and we were able to show dysfunction specific and sensitive the region previously shown to exhibit dysfunction in patients who progress to psychosis. The applied CBV region, however, did not have a higher positive predictive value than a known area of dysfunction in diagnosis or predicting disease states.

scan exclusion, it is a practice that many studies fail to adequately address.

We have also proposed two methods of vessel identification and elimination and examined the results of those techniques on the same scans. Unfortunately, we stand by our approach to base our algorithmic development on existing methods in lieu of completely foregoing each existing procedural step. Doing so we have in essence 'automated' the human intervention approaches such as identifying four voxels in a vessel and applying a strict threshold of voxels. By adding adaptive components to each, we have created a unique range of intra-subject CBV ROI values that are in concordance with existing literature and expected physiological values. Assigning an absolute numerical value, however, to these results, requires joint *in* and *ex vivo* analysis, perhaps using imaging capable of measuring neuronal blood volume through microscopy or histology approaches.

Nevertheless, we are eager to test and seek improvements for this approach on more images from different scanner types and acquisitions. Since much of our analysis requires templates (that are not yet generative), a greater variance in usable subject acquisition can provide important results. We also wish to seek better test-retest reliability, since there is no gold-standard for CBV, only differing modalities with their own advantages and limitations.

5.1.2 Specific Aim 2

We expect a variance of physiological CBV with the expectation that disease state aberrations are larger than that variance. Although we were uncertain of what results

might have been feasible given a new dataset and this group of controls and patients, we were pleased to discover changes that currently fall in line with expected findings in schizophrenia and psychosis using an entirely new analysis and approach. Although this dataset is still actively being followed, and we do not know eventual converters to psychosis given this high risk group, it is promising that alterations sensitive and specific to a region[1] of known dysfunction were sensitive and specific within a small region of the hippocampus.

The methodology of this template approach is one that can benefit from more sensitive hippocampal (or other regional) improvements and methods of co-registration, as well as different types of population templates. However, as it stands now, supported by the voxel information present in the current acquisition parameters, a highly accurate scheme of template derived images can be used to examine known loci of cerebral blood volume changes.

5.1.3 Specific Aim 3

The testing of this aim was a feasibility paradigm for *informed* structural image analysis changes. Given our finding in Alzheimer's disease CBV changes, we wanted to examine whether this region, the 'outer banks' of the lateral entorhinal cortex, the MTRC, might show structural signs of vulnerability in a new dataset, otherwise undetectable using group based or cortical volume based approaches.

Although this approach is examining two different measures, gray matter volume in an identical region applied to several images, and canonically derived entorhinal

[1]By region we mean either a canonical, drawn or derived region

cortex volume, the hypothesis that the region would be predictive of conversion in otherwise healthy individuals was based on the understanding that blood volume changes and cell death are continous and overlapping. Although the MTRC volume approach linearly trended towards significance across disease states, pure entorhinal cortex volume was significant at determining advanced disease state. To our surprise, MTRC GM volume changes were not as significant at delineating healthy controls and AD as entorhinal cortex volume alone. This leads us to support our previous hypothesis that impairment is focal in a specific area of the MTRC in the earlier stages of disease but then spreads through the MTL and other parts of the brain in later disease.

The framework of this analysis might have value in examining other areas of dysfunction measurable on CBV VBA that can be applied to gray matter volume. Although the exact timeline and mechanism of AD spread is not known in humans, one might be able to use this categorical disease state and volume analyses as a foundation for charting disease progression as a gradient: measurable changes in CBV leading to changes in gray matter, potentially overlapping depending on disease and pathology.

5.2 Conclusion

We have studied a variant of fMRI often overlooked, but with its roots firmly in the history of neuroimaging. We have analyzed this approach from 'fruits to nuts', inspecting all components from patient acquisition to forward application of detected regions. Although there is still much work to be done to examine replication, repro-

ducability, inter-scanner variance and longtiduinal analyses, we are eager to see the evolution of this version of functional imaging and the improvements we can make on existing and new disease states.

Bibliography

[1] J. Alvarez-Linera. 3t mri: advances in brain imaging. *Eur J Radiol*, 67(3):415–26, 2008.

[2] John Ashburner and Karl J. Friston. Unified segmentation. *NeuroImage*, 26(3):839–851, 2005.

[3] B. B. Avants, N. J. Tustison, J. Wu, P. A. Cook, and J. C. Gee. An open source multivariate framework for n-tissue segmentation with evaluation on public data. *Neuroinformatics*, 9(4):381–400, 2011.

[4] L. Axel. Surface coil magnetic resonance imaging. *J Comput Assist Tomogr*, 8(3):381–4, 1984.

[5] L. Axel and C. Hayes. Surface coil magnetic resonance imaging. *Arch Int Physiol Biochim*, 93(5):11–8, 1985.

[6] J. C. Baron, G. Chetelat, B. Desgranges, G. Perchey, B. Landeau, V. de la Sayette, and F. Eustache. In vivo mapping of gray matter loss with voxel-based morphometry in mild alzheimer's disease. *Neuroimage*, 14(2):298–309, 2001.

[7] J. W. Belliveau, Jr. Kennedy, D. N., R. C. McKinstry, B. R. Buchbinder, R. M. Weisskoff, M. S. Cohen, J. M. Vevea, T. J. Brady, and B. R. Rosen. Functional mapping of the human visual cortex by magnetic resonance imaging. *Science*, 254(5032):716–9, 1991.

[8] Hal Blumenfeld. *Neuroanatomy through clinical cases*. Sinauer Associates, Sunderland, Mass., 2002.

[9] H. Braak and E. Braak. Neuropathological stageing of alzheimer-related changes. *Acta Neuropathol*, 82(4):239–59, 1991.

[10] A. M. Brickman, U. A. Khan, F. A. Provenzano, L. K. Yeung, W. Suzuki, H. Schroeter, M. Wall, R. P. Sloan, and S. A. Small. Enhancing dentate gyrus function with dietary flavanols improves cognition in older adults. *Nat Neurosci*, 17(12):1798–803, 2014.

[11] A. M. Brickman, I. B. Meier, M. S. Korgaonkar, F. A. Provenzano, S. M. Grieve, K. L. Siedlecki, B. T. Wasserman, L. M. Williams, and M. E. Zimmerman.

Testing the white matter retrogenesis hypothesis of cognitive aging. *Neurobiol Aging*, 33(8):1699–715, 2012.

[12] A. M. Brickman, F. A. Provenzano, J. Muraskin, J. J. Manly, S. Blum, Z. Apa, Y. Stern, T. R. Brown, J. A. Luchsinger, and R. Mayeux. Regional white matter hyperintensity volume, not hippocampal atrophy, predicts incident alzheimer disease in the community. *Arch Neurol*, 69(12):1621–7, 2012.

[13] A. M. Brickman, N. Schupf, J. J. Manly, Y. Stern, J. A. Luchsinger, F. A. Provenzano, A. Narkhede, Q. Razlighi, L. Collins-Praino, S. Artero, T. N. Akbaraly, K. Ritchie, R. Mayeux, and F. Portet. Apoe epsilon4 and risk for alzheimer's disease: do regionally distributed white matter hyperintensities play a role? *Alzheimers Dement*, 10(6):619–29, 2014.

[14] A. M. Brickman, J. R. Sneed, F. A. Provenzano, E. Garcon, L. Johnert, J. Muraskin, L. K. Yeung, M. E. Zimmerman, and S. P. Roose. Quantitative approaches for assessment of white matter hyperintensities in elderly populations. *Psychiatry Res*, 193(2):101–6, 2011.

[15] A. M. Brickman, L. B. Zahodne, V. A. Guzman, A. Narkhede, I. B. Meier, E. Y. Griffith, F. A. Provenzano, N. Schupf, J. J. Manly, Y. Stern, J. A. Luchsinger, and R. Mayeux. Reconsidering harbingers of dementia: progression of parietal lobe white matter hyperintensities predicts alzheimer's disease incidence. *Neurobiol Aging*, 36(1):27–32, 2015.

[16] E. Bullitt, G. Gerig, S. M. Pizer, W. Lin, and S. R. Aylward. Measuring tortuosity of the intracerebral vasculature from mra images. *IEEE Trans Med Imaging*, 22(9):1163–71, 2003.

[17] L. G. Chepenik, F. Wang, L. Spencer, M. Spann, J. H. Kalmar, F. Womer, E. Kale Edmiston, B. Pittman, and H. P. Blumberg. Structure-function associations in hippocampus in bipolar disorder. *Biol Psychol*, 90(1):18–22, 2012.

[18] G. Chetelat. Alzheimer disease: Abeta-independent processes-rethinking preclinical ad. *Nat Rev Neurol*, 9(3):123–4, 2013.

[19] GlÃd'scher J.; Gitelman D. Contrast weights in flexible factorial de sign with multiple gr oups of subjects. *Online Publication*, 2008.

[20] V. Denolin, C. Azizieh, and T. Metens. New insights into the mechanisms of signal formation in rf-spoiled gradient echo sequences. *Magn Reson Med*, 54(4):937–54, 2005.

[21] L. Derex, M. Hermier, P. Adeleine, J. B. Pialat, M. Wiart, Y. Berthezene, J. C. Froment, P. Trouillas, and N. Nighoghossian. Influence of the site of arterial occlusion on multiple baseline hemodynamic mri parameters and post-thrombolytic recanalization in acute stroke. *Neuroradiology*, 46(11):883–7, 2004.

[22] C. Destrieux, B. Fischl, A. Dale, and E. Halgren. Automatic parcellation of human cortical gyri and sulci using standard anatomical nomenclature. *Neuroimage*, 53(1):1–15, 2010.

[23] Jacqueline Dominguez, Merceditas Dizon, Encarnita Ampil, Irma Kintanar, Ma Lourdes Corrales-Joson, and Marissa Ong. Use of neuroquant automated volumetric mri for alzheimer's disease diagnosis. *Alzheimer's and Dementia: The Journal of the Alzheimer's Association*, 9(4):P422–P423, 2013.

[24] Henri M. Duvernoy. *The human hippocampus functional anatomy, vascularization, and serial sections with MRI.* Springer,, Berlin ; New York, 3rd edition, 2005.

[25] B. Fischl, D. H. Salat, E. Busa, M. Albert, M. Dieterich, C. Haselgrove, A. van der Kouwe, R. Killiany, D. Kennedy, S. Klaveness, A. Montillo, N. Makris, B. Rosen, and A. M. Dale. Whole brain segmentation: automated labeling of neuroanatomical structures in the human brain. *Neuron*, 33(3):341–55, 2002.

[26] T. K. Foo, M. Saranathan, M. R. Prince, and T. L. Chenevert. Automated detection of bolus arrival and initiation of data acquisition in fast, three-dimensional, gadolinium-enhanced mr angiography. *Radiology*, 203(1):275–80, 1997.

[27] A.F. Frangi, W.J. Niessen, K.L. Vincken, and M. A. Viergever. Multiscale vessel enhancement filtering. *MICCAI'98 Lecture Notes in Computer Science*, 1496:130–137, 1998.

[28] K.J. Friston, A.P. Holmes, Worsley K. J., Poline J.P., C.D. Frith, and R. S. J. Frackowiak. Statistical parametric maps in functional imaging: A general linear approach. *Human Brain Mapping*, 2(4):189–210, 1994.

[29] C. B. Grandin, A. Bol, A. M. Smith, C. Michel, and G. Cosnard. Absolute cbf and cbv measurements by mri bolus tracking before and after acetazolamide challenge: repeatabilily and comparison with pet in humans. *Neuroimage*, 26(2):525–35, 2005.

[30] H. Greenspan, A. Ruf, and J. Goldberger. Constrained gaussian mixture model framework for automatic segmentation of mr brain images. *IEEE Trans Med Imaging*, 25(9):1233–45, 2006.

[31] D. A. Gusnard, M. E. Raichle, and M. E. Raichle. Searching for a baseline: functional imaging and the resting human brain. *Nat Rev Neurosci*, 2(10):685–94, 2001.

[32] N. B. Hamilton, D. Attwell, and C. N. Hall. Pericyte-mediated regulation of capillary diameter: a component of neurovascular coupling in health and disease. *Front Neuroenergetics*, 2, 2010.

[33] X. Han, J. Jovicich, D. Salat, A. van der Kouwe, B. Quinn, S. Czanner, E. Busa, J. Pacheco, M. Albert, R. Killiany, P. Maguire, D. Rosas, N. Makris, A. Dale, B. Dickerson, and B. Fischl. Reliability of mri-derived measurements of human cerebral cortical thickness: the effects of field strength, scanner upgrade and manufacturer. *Neuroimage*, 32(1):180–94, 2006.

[34] N.G. Harris, V. Gauden, P.A. Fraser, S.R. Williams, and G.J.M. Parker. Blood-brain barrier permeability to gadolinium and horseradish peroxidase after spontaneous reperfusion in the starch microsphere model of ischemia. *Proc. Intl. Soc. Mag. Reson. Med*, 8, 2000.

[35] W Harvey. *On The Motion Of The Heart And Blood In Animals*. 1628.

[36] C. Haselgrove, J. B. Poline, and D. N. Kennedy. A simple tool for neuroimaging data sharing. *Front Neuroinform*, 8:52, 2014.

[37] X. He and D. A. Yablonskiy. Quantitative bold: mapping of human cerebral deoxygenated blood volume and oxygen extraction fraction: default state. *Magn Reson Med*, 57(1):115–26, 2007.

[38] Aetna Healthcare. Aetna clinical policy bulletin: Magnetic resonance angiography (mra) and magnetic resonance venography (mrv). *Online Publication*, 2014.

[39] M. E. Henry, M. J. Kaufman, N. Lange, M. E. Schmidt, S. Purcell, J. Cote, D. M. Perron-Henry, E. Stoddard, B. M. Cohen, and P. F. Renshaw. Test-retest reliability of dsc mri cbv mapping in healthy volunteers. *Neuroreport*, 12(8):1567–9, 2001.

[40] M. Higashima, Y. Kawasaki, K. Urata, N. Sakai, T. Nagasawa, Y. Koshino, H. Sumiya, N. Tonami, S. Tsuji, and H. Matsuda. Regional cerebral blood flow in male schizophrenic patients performing an auditory discrimination task. *Schizophr Res*, 42(1):29–39, 2000.

[41] E. Imabayashi, H. Matsuda, T. Tabira, K. Arima, N. Araki, K. Ishii, F. Yamashita, T. Iwatsubo, and Initiative Japanese Alzheimer's Disease Neuroimaging. Comparison between brain ct and mri for voxel-based morphometry of alzheimer's disease. *Brain Behav*, 3(4):487–93, 2013.

[42] N. Kanwisher, J. McDermott, and M. M. Chun. The fusiform face area: a module in human extrastriate cortex specialized for face perception. *J Neurosci*, 17(11):4302–11, 1997.

[43] G. Kempermann, H. G. Kuhn, and F. H. Gage. More hippocampal neurons in adult mice living in an enriched environment. *Nature*, 386(6624):493–5, 1997.

[44] U. A. Khan, L. Liu, F. A. Provenzano, D. E. Berman, C. P. Profaci, R. Sloan, R. Mayeux, K. E. Duff, and S. A. Small. Molecular drivers and cortical spread

of lateral entorhinal cortex dysfunction in preclinical alzheimer's disease. *Nat Neurosci*, 17(2):304–11, 2014.

[45] K. Kuppusamy, W. Lin, G. R. Cizek, and E. M. Haacke. In vivo regional cerebral blood volume: quantitative assessment with 3d t1-weighted pre- and postcontrast mr imaging. *Radiology*, 201(1):106–12, 1996.

[46] H. B. Larsson, M. Stubgaard, J. L. Frederiksen, M. Jensen, O. Henriksen, and O. B. Paulson. Quantitation of blood-brain barrier defect by magnetic resonance imaging and gadolinium-dtpa in patients with multiple sclerosis and brain tumors. *Magn Reson Med*, 16(1):117–31, 1990.

[47] C. Lavini and J. J. Verhoeff. Reproducibility of the gadolinium concentration measurements and of the fitting parameters of the vascular input function in the superior sagittal sinus in a patient population. *Magn Reson Imaging*, 28(10):1420–30, 2010.

[48] K. Y. Leung, F. van der Lijn, H. A. Vrooman, M. C. Sturkenboom, and W. J. Niessen. It infrastructure to support the secondary use of routinely acquired clinical imaging data for research. *Neuroinformatics*, 13(1):65–81, 2015.

[49] N. M. Lewandowski, Y. Bordelon, A. M. Brickman, S. Angulo, U. Khan, J. Muraskin, E. Y. Griffith, P. Wasserman, L. Menalled, J. P. Vonsattel, K. Marder, S. A. Small, and H. Moreno. Regional vulnerability in huntington's disease: fmri-guided molecular analysis in patients and a mouse model of disease. *Neurobiol Dis*, 52:84–93, 2013.

[50] W. Lin, A. Celik, and R. P. Paczynski. Regional cerebral blood volume: a comparison of the dynamic imaging and the steady state methods. *J Magn Reson Imaging*, 9(1):44–52, 1999.

[51] H. L. Liu, Y. Pu, Y. Liu, L. Nickerson, T. Andrews, P. T. Fox, and J. H. Gao. Cerebral blood flow measurement by dynamic contrast mri using singular value decomposition with an adaptive threshold. *Magn Reson Med*, 42(1):167–72, 1999.

[52] C. Martin. Contributions and complexities from the use of in vivo animal models to improve understanding of human neuroimaging signals. *Front Neurosci*, 8:211, 2014.

[53] J. Mazziotta, A. Toga, A. Evans, P. Fox, J. Lancaster, K. Zilles, R. Woods, T. Paus, G. Simpson, B. Pike, C. Holmes, L. Collins, P. Thompson, D. MacDonald, M. Iacoboni, T. Schormann, K. Amunts, N. Palomero-Gallagher, S. Geyer, L. Parsons, K. Narr, N. Kabani, G. Le Goualher, D. Boomsma, T. Cannon, R. Kawashima, and B. Mazoyer. A probabilistic atlas and reference system for the human brain: International consortium for brain mapping (icbm). *Philos Trans R Soc Lond B Biol Sci*, 356(1412):1293–322, 2001.

[54] J. Mazziotta, A. Toga, A. Evans, P. Fox, J. Lancaster, K. Zilles, R. Woods, T. Paus, G. Simpson, B. Pike, C. Holmes, L. Collins, P. Thompson, D. MacDonald, M. Iacoboni, T. Schormann, K. Amunts, N. Palomero-Gallagher, S. Geyer, L. Parsons, K. Narr, N. Kabani, G. Le Goualher, J. Feidler, K. Smith, D. Boomsma, H. Hulshoff Pol, T. Cannon, R. Kawashima, and B. Mazoyer. A four-dimensional probabilistic atlas of the human brain. *J Am Med Inform Assoc*, 8(5):401–30, 2001.

[55] T. J. Miller, T. H. McGlashan, J. L. Rosen, K. Cadenhead, T. Cannon, J. Ventura, W. McFarlane, D. O. Perkins, G. D. Pearlson, and S. W. Woods. Prodromal assessment with the structured interview for prodromal syndromes and the scale of prodromal symptoms: predictive validity, interrater reliability, and training to reliability. *Schizophr Bull*, 29(4):703–15, 2003.

[56] S. Minoshima, B. Giordani, S. Berent, K. A. Frey, N. L. Foster, and D. E. Kuhl. Metabolic reduction in the posterior cingulate cortex in very early alzheimer's disease. *Ann Neurol*, 42(1):85–94, 1997.

[57] B. Moghaddam and D. Javitt. From revolution to evolution: the glutamate hypothesis of schizophrenia and its implication for treatment. *Neuropsychopharmacology*, 37(1):4–15, 2012.

[58] H. Moreno, F. Hua, T. Brown, and S. Small. Longitudinal mapping of mouse cerebral blood volume with mri. *NMR Biomed*, 19(5):535–43, 2006.

[59] E. C. Mormino, M. G. Brandel, C. M. Madison, G. D. Rabinovici, S. Marks, S. L. Baker, and W. J. Jagust. Not quite pib-positive, not quite pib-negative: slight pib elevations in elderly normal control subjects are biologically relevant. *Neuroimage*, 59(2):1152–60, 2012.

[60] A. Mosso. *Ueber den Kreislauf des Blutes im menschlichen Gehirn*. Verlag von Veit, Leipzig, 1881.

[61] MRI-q. Choosing pe and fe direction.

[62] John P. Mugler and James R. Brookeman. Three-dimensional magnetization-prepared rapid gradient-echo imaging (3d mp rage). *Magnetic Resonance in Medicine*, 15(1):152–157, 1990.

[63] A. L. Ochs, D. E. Ross, M. D. Zannoni, T. J. Abildskov, and E. D. Bigler. Comparison of automated brain volume measures obtained with neuroquant(r) and freesurfer. *J Neuroimaging*, 2015.

[64] S. Ogawa, T. M. Lee, A. S. Nayak, and P. Glynn. Oxygenation-sensitive contrast in magnetic resonance image of rodent brain at high magnetic fields. *Magn Reson Med*, 14(1):68–78, 1990.

[65] Y. Okubo, H. Olsson, H. Ito, M. Lofti, T. Suhara, C. Halldin, and L. Farde. Pet mapping of extrastriatal d2-like dopamine receptors in the human brain using an anatomic standardization technique and [11c]flb 457. *Neuroimage*, 10(6):666–74, 1999.

[66] L. Ostergaard. Cerebral perfusion imaging by bolus tracking. *Top Magn Reson Imaging*, 15(1):3–9, 2004.

[67] George Paxinos, Keith B. J. Franklin, and Keith B. J. Franklin. *Paxinos and Franklin's the mouse brain in stereotaxic coordinates*. Boston : Elsevier/Academic Press, Amsterdam, 4th edition, 2013.

[68] A. C. Pereira, D. E. Huddleston, A. M. Brickman, A. A. Sosunov, R. Hen, G. M. McKhann, R. Sloan, F. H. Gage, T. R. Brown, and S. A. Small. An in vivo correlate of exercise-induced neurogenesis in the adult dentate gyrus. *Proc Natl Acad Sci U S A*, 104(13):5638–43, 2007.

[69] R. I. Pettigrew, L. Avruch, W. Dannels, J. Coumans, and M. E. Bernardino. Fast-field-echo mr imaging with gd-dtpa: physiologic evaluation of the kidney and liver. *Radiology*, 160(2):561–3, 1986.

[70] R. E. Port, M. V. Knopp, and G. Brix. Dynamic contrast-enhanced mri using gd-dtpa: interindividual variability of the arterial input function and consequences for the assessment of kinetics in tumors. *Magn Reson Med*, 45(6):1030–8, 2001.

[71] F. A. Provenzano, J. Muraskin, G. Tosto, A. Narkhede, B. T. Wasserman, E. Y. Griffith, V. A. Guzman, I. B. Meier, M. E. Zimmerman, A. M. Brickman, and Initiative Alzheimer's Disease Neuroimaging. White matter hyperintensities and cerebral amyloidosis: necessary and sufficient for clinical expression of alzheimer disease? *JAMA Neurol*, 70(4):455–61, 2013.

[72] E. Pusey, R. B. Lufkin, R. K. Brown, M. A. Solomon, D. D. Stark, R. W. Tarr, and W. N. Hanafee. Magnetic resonance imaging artifacts: mechanism and clinical significance. *Radiographics*, 6(5):891–911, 1986.

[73] Santiago Ramon y Cajal. *Histologie du systeme nerveux de lhomme and des vertebres*. A. Maloine, Paris, 1909.

[74] B. R. Rosen, J. W. Belliveau, H. J. Aronen, D. Kennedy, B. R. Buchbinder, A. Fischman, M. Gruber, J. Glas, R. M. Weisskoff, M. S. Cohen, and et al. Susceptibility contrast imaging of cerebral blood volume: human experience. *Magn Reson Med*, 22(2):293–9; discussion 300–3, 1991.

[75] D. E. Ross, A. L. Ochs, J. M. Seabaugh, M. F. Demark, C. R. Shrader, J. H. Marwitz, and M. D. Havranek. Progressive brain atrophy in patients with chronic neuropsychiatric symptoms after mild traumatic brain injury: a preliminary study. *Brain Inj*, 26(12):1500–9, 2012.

[76] J. Rother, F. Guckel, W. Neff, A. Schwartz, and M. Hennerici. Assessment of regional cerebral blood volume in acute human stroke by use of single-slice dynamic susceptibility contrast-enhanced magnetic resonance imaging. *Stroke*, 27(6):1088–93, 1996.

[77] C. S. Roy and C. S. Sherrington. On the regulation of the blood-supply of the brain. *J Physiol*, 11(1-2):85–158 17, 1890.

[78] M. R. Sabuncu, B. T. Yeo, K. Van Leemput, B. Fischl, and P. Golland. A generative model for image segmentation based on label fusion. *IEEE Trans Med Imaging*, 29(10):1714–29, 2010.

[79] L. Schmaal, D. J. Veltman, T. G. van Erp, P. G. Samann, T. Frodl, N. Jahanshad, E. Loehrer, H. Tiemeier, A. Hofman, W. J. Niessen, M. W. Vernooij, M. A. Ikram, K. Wittfeld, H. J. Grabe, A. Block, K. Hegenscheid, H. Volzke, D. Hoehn, M. Czisch, J. Lagopoulos, S. N. Hatton, I. B. Hickie, R. Goya-Maldonado, B. Kramer, O. Gruber, B. Couvy-Duchesne, M. E. Renteria, L. T. Strike, N. T. Mills, G. I. de Zubicaray, K. L. McMahon, S. E. Medland, N. G. Martin, N. A. Gillespie, M. J. Wright, G. B. Hall, G. M. MacQueen, E. M. Frey, A. Carballedo, L. S. van Velzen, M. J. van Tol, N. J. van der Wee, I. M. Veer, H. Walter, K. Schnell, E. Schramm, C. Normann, D. Schoepf, C. Konrad, B. Zurowski, T. Nickson, A. M. McIntosh, M. Papmeyer, H. C. Whalley, J. E. Sussmann, B. R. Godlewska, P. J. Cowen, F. H. Fischer, M. Rose, B. W. Penninx, P. M. Thompson, and D. P. Hibar. Subcortical brain alterations in major depressive disorder: findings from the enigma major depressive disorder working group. *Mol Psychiatry*, 2015.

[80] S. A. Schobel, N. H. Chaudhury, U. A. Khan, B. Paniagua, M. A. Styner, I. Asllani, B. P. Inbar, C. M. Corcoran, J. A. Lieberman, H. Moore, and S. A. Small. Imaging patients with psychosis and a mouse model establishes a spreading pattern of hippocampal dysfunction and implicates glutamate as a driver. *Neuron*, 78(1):81–93, 2013.

[81] N. Schuff, N. Woerner, L. Boreta, T. Kornfield, L. M. Shaw, J. Q. Trojanowski, P. M. Thompson, Jr. Jack, C. R., M. W. Weiner, and Initiative Alzheimer's Disease Neuroimaging. Mri of hippocampal volume loss in early alzheimer's disease in relation to apoe genotype and biomarkers. *Brain*, 132(Pt 4):1067–77, 2009.

[82] Y. I. Sheline. Neuroimaging studies of mood disorder effects on the brain. *Biol Psychiatry*, 54(3):338–52, 2003.

[83] S. A. Small. Isolating pathogenic mechanisms embedded within the hippocampal circuit through regional vulnerability. *Neuron*, 84(1):32–9, 2014.

[84] S. A. Small, S. A. Schobel, R. B. Buxton, M. P. Witter, and C. A. Barnes. A pathophysiological framework of hippocampal dysfunction in ageing and disease. *Nat Rev Neurosci*, 12(10):585–601, 2011.

[85] S. M. Smith. Fast robust automated brain extraction. *Hum Brain Mapp*, 17(3):143–55, 2002.

[86] V. Smith, L. Shapiro, D. Hanlon, R. Martin, J. Brinkley, A. Poliakov, G. Ojemann, and D. Corina. Evaluating spatial normalization methods for the human brain. *Conf Proc IEEE Eng Med Biol Soc*, 5:5331–4, 2005.

[87] R. A. Sperling, P. S. Aisen, L. A. Beckett, D. A. Bennett, S. Craft, A. M. Fagan, T. Iwatsubo, Jr. Jack, C. R., J. Kaye, T. J. Montine, D. C. Park, E. M. Reiman, C. C. Rowe, E. Siemers, Y. Stern, K. Yaffe, M. C. Carrillo, B. Thies, M. Morrison-Bogorad, M. V. Wagster, and C. H. Phelps. Toward defining the preclinical stages of alzheimer's disease: recommendations from the national institute on aging-alzheimer's association workgroups on diagnostic guidelines for alzheimer's disease. *Alzheimers Dement*, 7(3):280–92, 2011.

[88] A. Stadler, W. Schima, A. Ba-Ssalamah, J. Kettenbach, and E. Eisenhuber. Artifacts in body mr imaging: their appearance and how to eliminate them. *Eur Radiol*, 17(5):1242–55, 2007.

[89] K. H. Su, J. S. Lee, J. H. Li, Y. W. Yang, R. S. Liu, and J. C. Chen. Partial volume correction of the micropet blood input function using ensemble learning independent component analysis. *Phys Med Biol*, 54(6):1823–46, 2009.

[90] P. Talati, S. Rane, S. Kose, J. U. Blackford, J. Gore, M. J. Donahue, and S. Heckers. Increased hippocampal ca1 cerebral blood volume in schizophrenia. *Neuroimage Clin*, 5:359–64, 2014.

[91] P. S. Tofts, G. Brix, D. L. Buckley, J. L. Evelhoch, E. Henderson, M. V. Knopp, H. B. Larsson, T. Y. Lee, N. A. Mayr, G. J. Parker, R. E. Port, J. Taylor, and R. M. Weisskoff. Estimating kinetic parameters from dynamic contrast-enhanced t(1)-weighted mri of a diffusable tracer: standardized quantities and symbols. *J Magn Reson Imaging*, 10(3):223–32, 1999.

[92] P. van der Meulen, J. P. Groen, and J. J. Cuppen. Very fast mr imaging by field echoes and small angle excitation. *Magn Reson Imaging*, 3(3):297–9, 1985.

[93] T. G. van Erp, D. P. Hibar, J. M. Rasmussen, D. C. Glahn, G. D. Pearlson, O. A. Andreassen, I. Agartz, L. T. Westlye, U. K. Haukvik, A. M. Dale, I. Melle, C. B. Hartberg, O. Gruber, B. Kraemer, D. Zilles, G. Donohoe, S. Kelly, C. McDonald, D. W. Morris, D. M. Cannon, A. Corvin, M. W. Machielsen, L. Koenders, L. de Haan, D. J. Veltman, T. D. Satterthwaite, D. H. Wolf, R. C. Gur, R. E. Gur, S. G. Potkin, D. H. Mathalon, B. A. Mueller, A. Preda, F. Macciardi, S. Ehrlich, E. Walton, J. Hass, V. D. Calhoun, H. J. Bockholt, S. R. Sponheim, J. M. Shoemaker, N. E. van Haren, H. E. Pol, R. A. Ophoff, R. S. Kahn, R. Roiz-Santianez, B. Crespo-Facorro, L. Wang, K. I. Alpert, E. G. Jonsson, R. Dimitrova, C. Bois, H. C. Whalley, A. M. McIntosh, S. M. Lawrie, R. Hashimoto, P. M. Thompson, and J. A. Turner. Subcortical brain volume

abnormalities in 2028 individuals with schizophrenia and 2540 healthy controls via the enigma consortium. *Mol Psychiatry*, 2015.

[94] M. J. van Osch, E. J. Vonken, C. J. Bakker, and M. A. Viergever. Correcting partial volume artifacts of the arterial input function in quantitative cerebral perfusion mri. *Magn Reson Med*, 45(3):477–85, 2001.

[95] P. Vanderhaeghen and H. J. Cheng. Guidance molecules in axon pruning and cell death. *Cold Spring Harb Perspect Biol*, 2(6):a001859, 2010.

[96] A. Villringer and U. Dirnagl. Coupling of brain activity and cerebral blood flow: basis of functional neuroimaging. *Cerebrovasc Brain Metab Rev*, 7(3):240–76, 1995.

[97] K. B. Walhovd, A. M. Fjell, and T. Espeseth. Cognitive decline and brain pathology in aging–need for a dimensional, lifespan and systems vulnerability view. *Scand J Psychol*, 55(3):244–54, 2014.

[98] S. Warach, W. Li, M. Ronthal, and R. R. Edelman. Acute cerebral ischemia: evaluation with dynamic contrast-enhanced mr imaging and mr angiography. *Radiology*, 182(1):41–7, 1992.

[99] J. Z. Willey, N. Scarmeas, F. A. Provenzano, J. A. Luchsinger, R. Mayeux, and A. M. Brickman. White matter hyperintensity volume and impaired mobility among older adults. *J Neurol*, 260(3):884–90, 2013.

[100] D. L. Wilson and J. A. Noble. An adaptive segmentation algorithm for time-of-flight mra data. *Medical Imaging IEEE Transactions on*, 18(10):938–945, 1999.

[101] A. M. Wink and J. B. Roerdink. Denoising functional mr images: a comparison of wavelet denoising and gaussian smoothing. *IEEE Trans Med Imaging*, 23(3):374–87, 2004.

[102] C. Yang, G. S. Karczmar, M. Medved, A. Oto, M. Zamora, and W. M. Stadler. Reproducibility assessment of a multiple reference tissue method for quantitative dynamic contrast enhanced-mri analysis. *Magn Reson Med*, 61(4):851–9, 2009.

[103] Y. Zhang, M. Brady, and S. Smith. Segmentation of brain mr images through a hidden markov random field model and the expectation-maximization algorithm. *IEEE Trans Med Imaging*, 20(1):45–57, 2001.

[104] K. C. Zierhut, R. Grassmann, J. Kaufmann, J. Steiner, B. Bogerts, and K. Schiltz. Hippocampal ca1 deformity is related to symptom severity and antipsychotic dosage in schizophrenia. *Brain*, 136(Pt 3):804–14, 2013.

Chapter 6

Appendix

Table 6.1: T1 relaxation values of known tissue types

Tissue	T1(ms)
gray matter (GM)	950
white matter (WM)	600
muscle	900
cerebrospinal fluid (CSF)	4500
blood (arterial)	1200
blood (venous)	1200
blood (gado enhanced)	1200

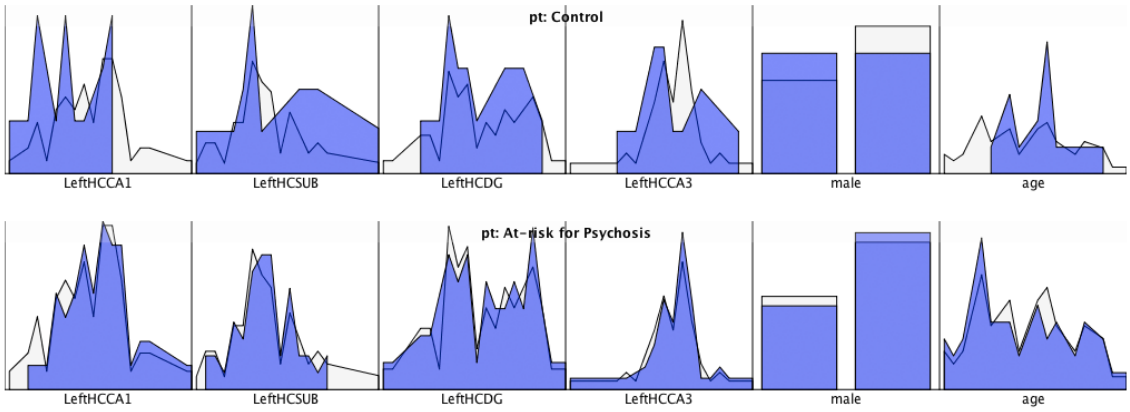

pt		age	male
Control	Mean	22.5625	.5000
	N	16	16
	Std. Deviation	2.25000	.51640
At-risk for Psychosis	Mean	21.1000	.6522
	N	50	46
	Std. Deviation	3.81324	.48154
Total	Mean	21.4545	.6129
	N	66	62
	Std. Deviation	3.53959	.49106

Figure 6-1: The demographics of the prodromal psychosis data-set.

Table 6.2: Eigenvalue shape characteristics in three dimensions based on the 1st, 2nd and 3rd eigenvalues[27]

λ_1	λ_1	λ_1	Orientation Pattern
L	L	H(-)	plate like (bright)
L	L	H(+)	plate like (dark)
L	H(-)	H(-)	tubular like (bright)
L	H(+)	H(+)	tubular like (dark)
H(-)	H(-)	H(-)	blob like (bright)
H(+)	H(+)	H(+)	blob like (dark)

Table 6.3: Voxel and cluster based results from VBM analysis

cluster p(FWE-cor)	cluster p(FDR-cor)	cluster equivk	cluster p(unc)	peak p(FWE-cor)	peak p(FDR-cor)	peak T	peak equivZ	peak p(unc)	x,y,z	{mm}	
0.122	0.255	1315	0.009	0.234	0.658	4.78	4.37	0	-21	-7	-17
				0.856	0.658	4.07	3.8	0	-28	18	-11
				0.977	0.69	3.81	3.58	0	-42	9	-27
0.271	0.31	958	0.023	0.445	0.658	4.51	4.15	0	26	9	-39
				0.828	0.658	4.11	3.83	0	21	-7	-17
				0.995	0.69	3.66	3.46	0	28	-1	-23
0.971	0.843	207	0.257	0.554	0.658	4.39	4.06	0	-38	-51	28
0.995	0.843	118	0.393	0.639	0.658	4.31	4	0	-44	-16	-33
0.863	0.843	352	0.144	0.695	0.658	4.25	3.95	0	-42	-39	45
0.967	0.843	215	0.248	0.764	0.658	4.18	3.89	0	-57	-4	-20
0.994	0.843	128	0.373	0.847	0.658	4.08	3.81	0	10	-13	0
0.942	0.843	258	0.207	0.908	0.69	3.99	3.73	0	8	-51	37
				0.997	0.704	3.61	3.42	0	8	-37	43
				0.999	0.704	3.54	3.35	0	6	-57	27
0.996	0.843	112	0.406	0.96	0.69	3.87	3.64	0	-6	-52	33
0.989	0.843	153	0.329	0.973	0.69	3.82	3.6	0	-3	-72	22
0.901	0.843	311	0.168	0.975	0.69	3.81	3.59	0	27	18	0
0.996	0.843	117	0.395	0.985	0.69	3.76	3.54	0	-44	-73	24
				0.994	0.69	3.69	3.48	0	-40	-78	30
0.993	0.843	134	0.362	0.992	0.69	3.7	3.49	0	-38	-10	-6

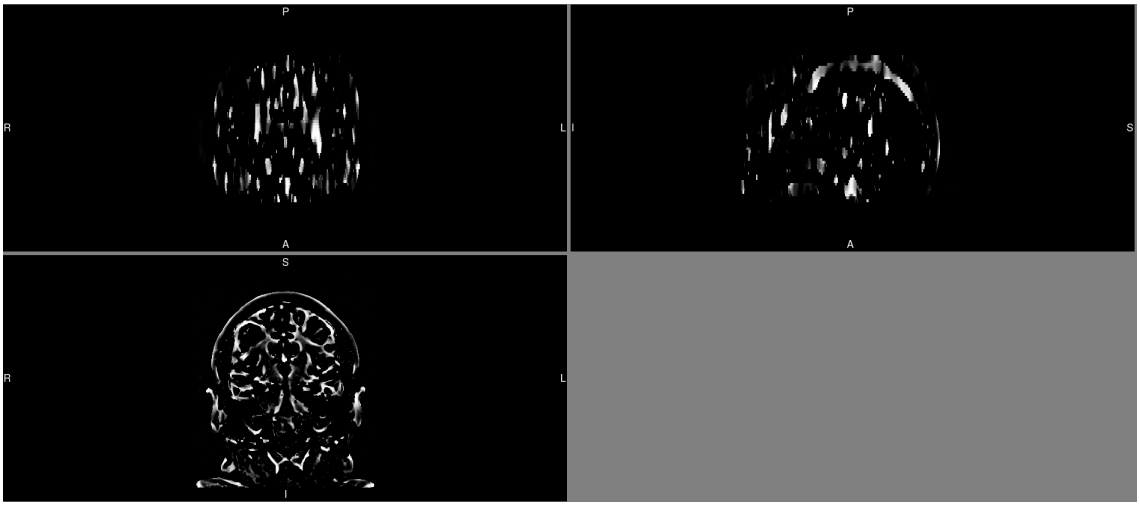

Figure 6-2: Vesselness maps with the following characterstics: α=0.2, β=20, c=30

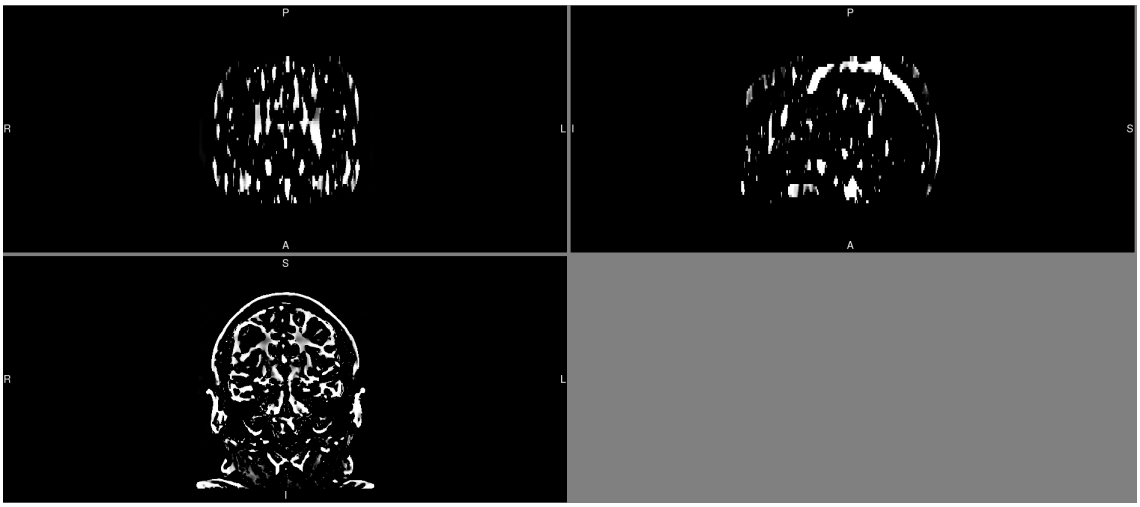

Figure 6-3: Vesselness maps with the following characterstics: α=0.05, β=50, c=30

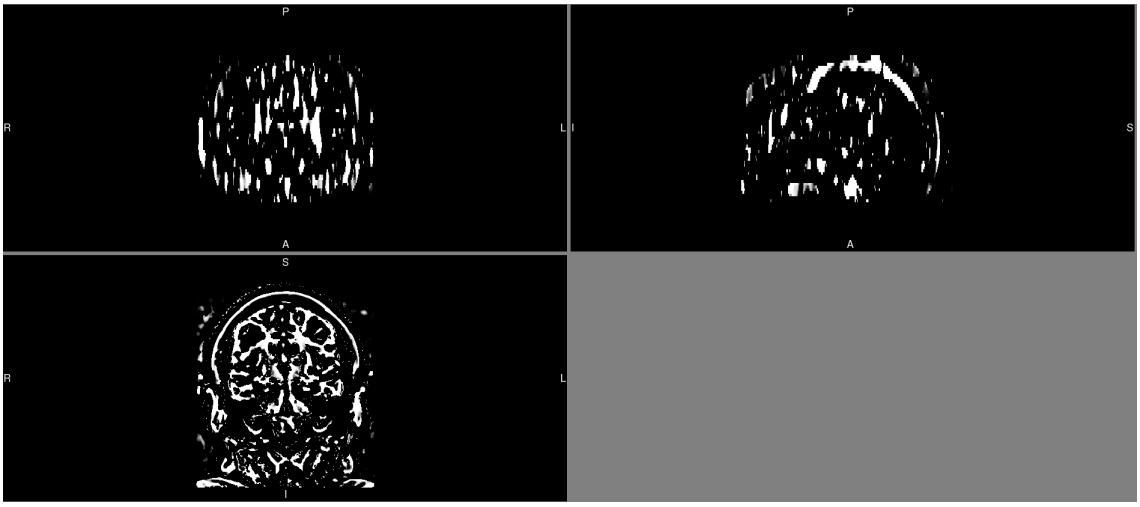

Figure 6-4: Vesselness maps with the following characterstics: α=0.05, β=50, c=1

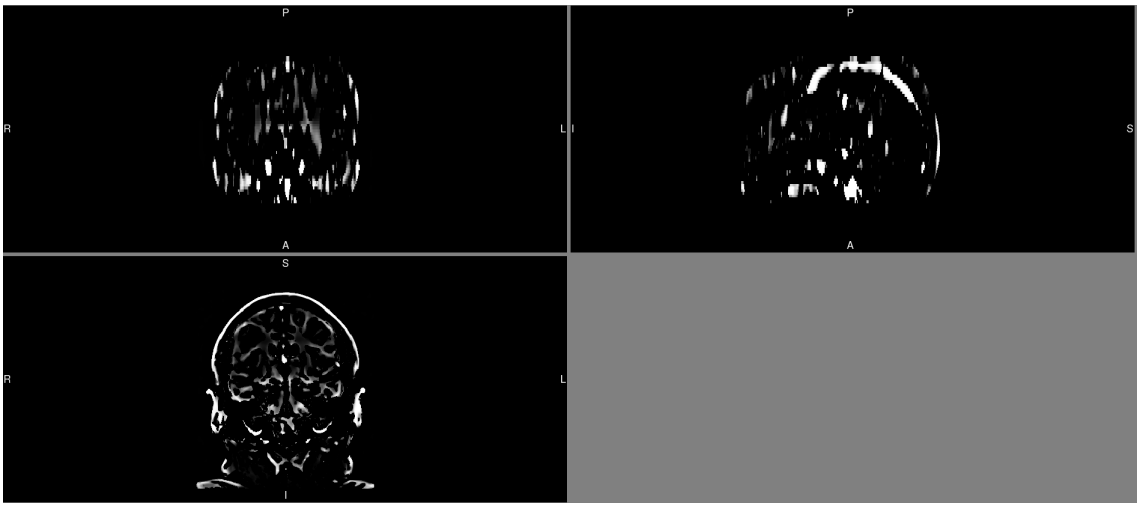

Figure 6-5: Vesselness maps with the following characterstics: α=0.2, β=20, c=100

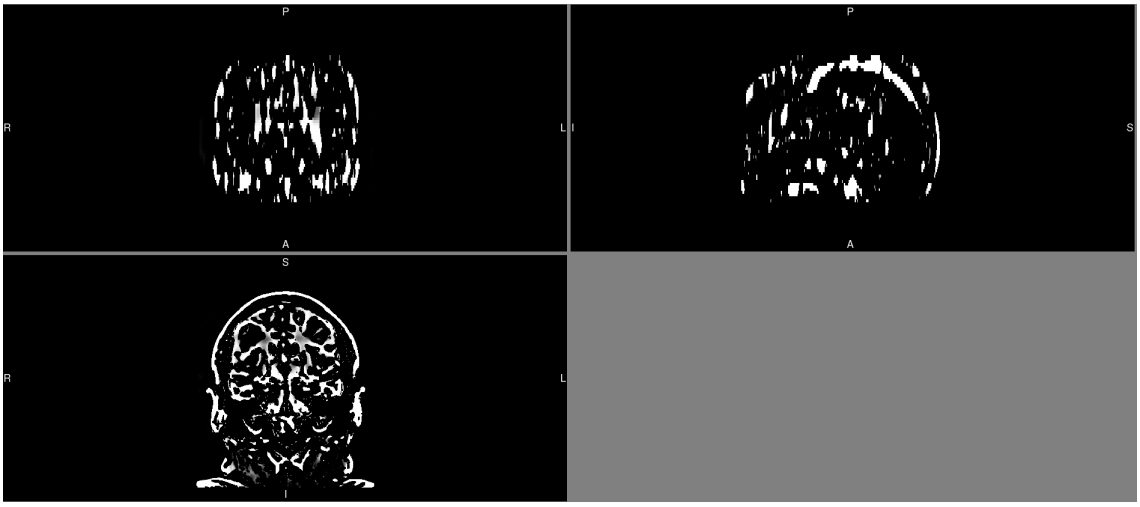

Figure 6-6: Vesselness maps with the following characterstics: α=0.01, β=20, c=30

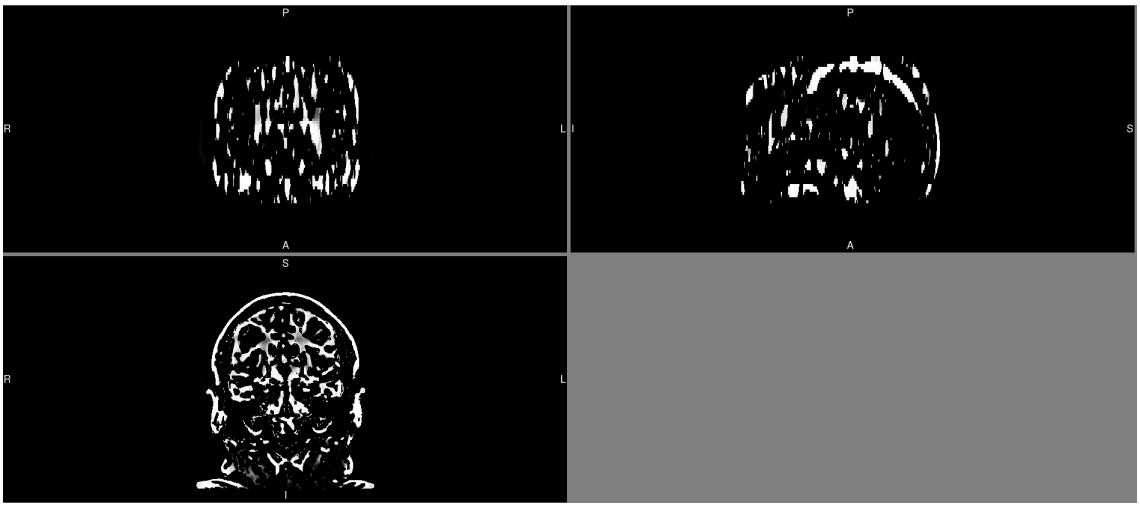

Figure 6-7: Vesselness maps with the following characterstics: α=0.01, β=1, c=30

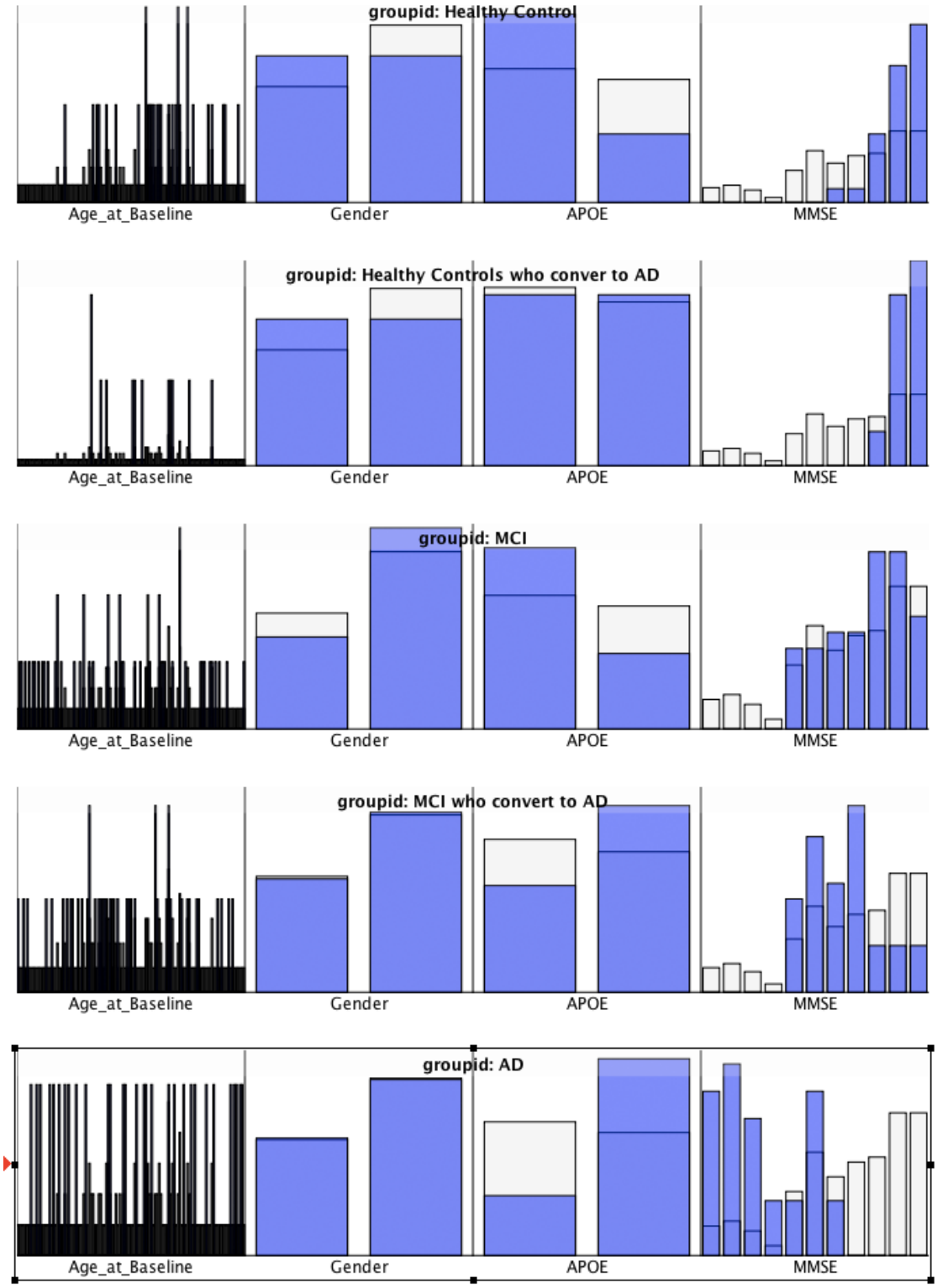

Figure 6-8: ADNI study demographics.

grouping		APOE	mmse	weight	Gender	age_at_baseline
Healthy Control	N	30	30	30	30	30
	Mean	3.27	29.1000	75.5867	.50	79.060000
	Std. Deviation	.450	1.02889	14.22263	.509	3.7512848
Healthy Control who convert to AD	N	12	12	12	12	12
	Mean	3.50	29.4167	71.6917	.50	77.400000
	Std. Deviation	.522	.66856	13.55618	.522	3.6321794
MCI Control	N	51	51	51	51	51
	Mean	3.29	27.4510	78.4843	.69	74.431373
	Std. Deviation	.460	1.89012	12.93224	.469	7.7100322
MCI Control who convert to AD	N	44	44	44	44	44
	Mean	3.64	26.3864	74.0477	.61	74.965909
	Std. Deviation	.487	1.71472	16.24594	.493	6.5061310
AD Control	N	30	30	30	30	30
	Mean	3.77	22.4333	72.9133	.60	76.413333
	Std. Deviation	.430	2.04574	12.35346	.498	7.4144190
Total	N	167	167	167	167	167
	Mean	3.48	26.7066	75.3060	.60	75.973054
	Std. Deviation	.501	2.80127	14.08669	.490	6.6865396

Figure 6-9: ADNI study demographics.

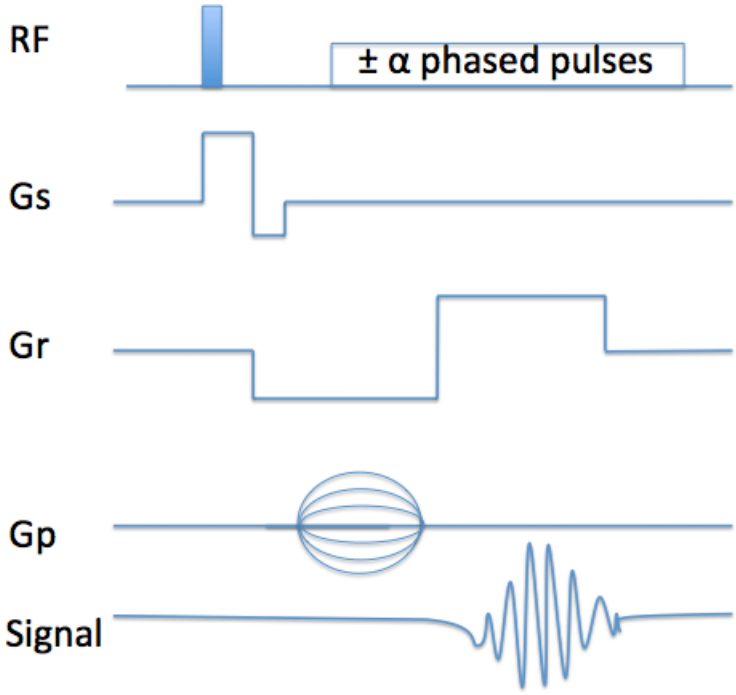

Figure 6-10: Pulse sequence diagram of an rf spoiled gradient echo image, as is used in the antecedent pre and post contrast MRI images. The top line reflects the rf pulse from the magnet, that both applies the prepulse and alternating phased pulses to cancel transverse magnetizations. 'Gs' reflects the slice lobe, 'Gr' reflects the read lobe, 'Gp' the phase lobe and 'Signal' contains just that. Gradient spoiling can occur by means of either just the 'Gs' or with the 'Gr' applying a varying, sometimes random pulse.

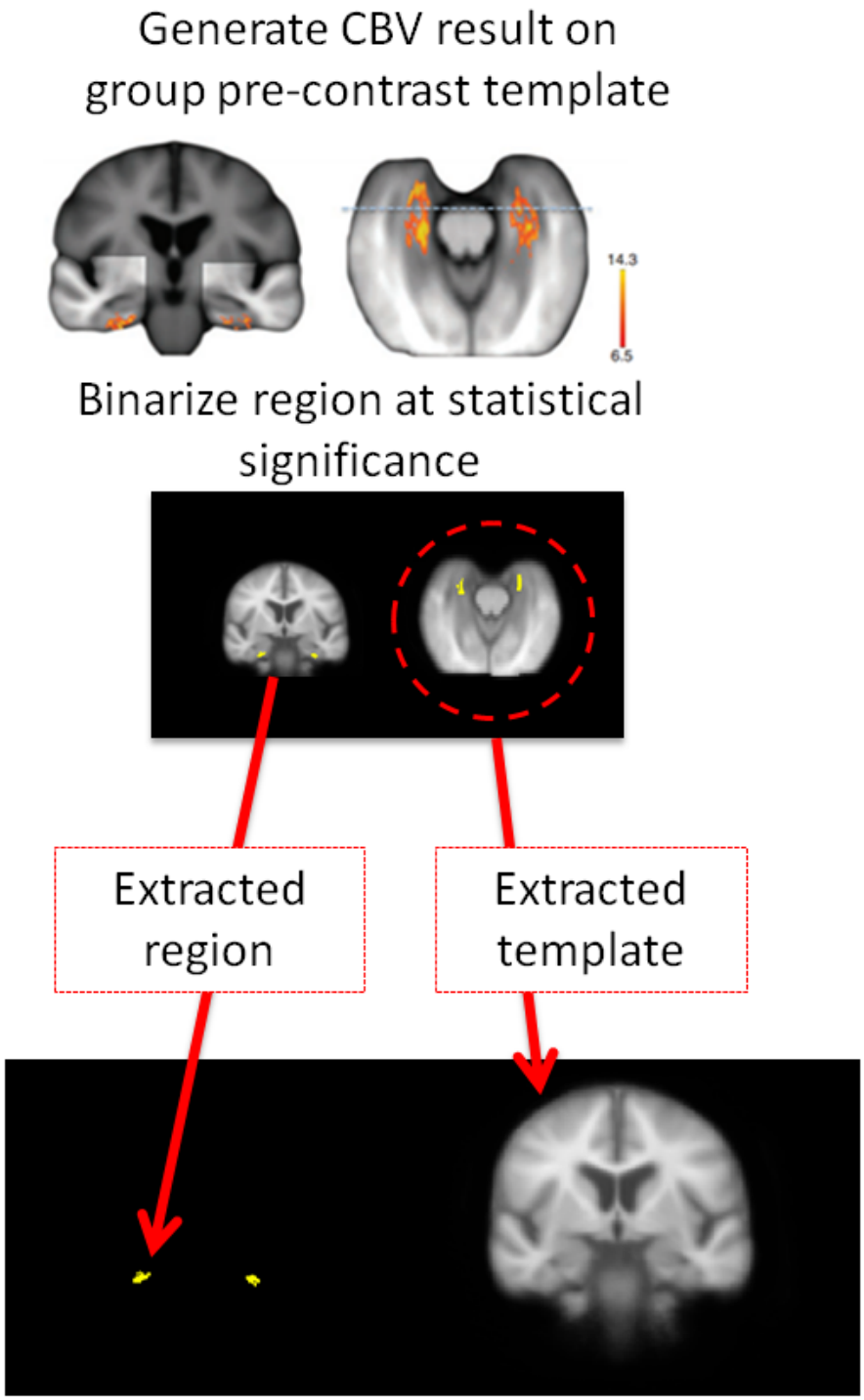

Figure 6-11: This shows how we derive functional ROI from voxel based approaches. To do this we generate CBV results on a template brain which is derived from pre-contrast T1 weighted images. These images contain adequate structural data for diffeomorphic co-registration algorithms to co-register smaller features than EPI sequences. We binarize (i.e. threshold the resultant map at the t or f level of significance) the mask at the lowest statistical level and save that separate from the generated template

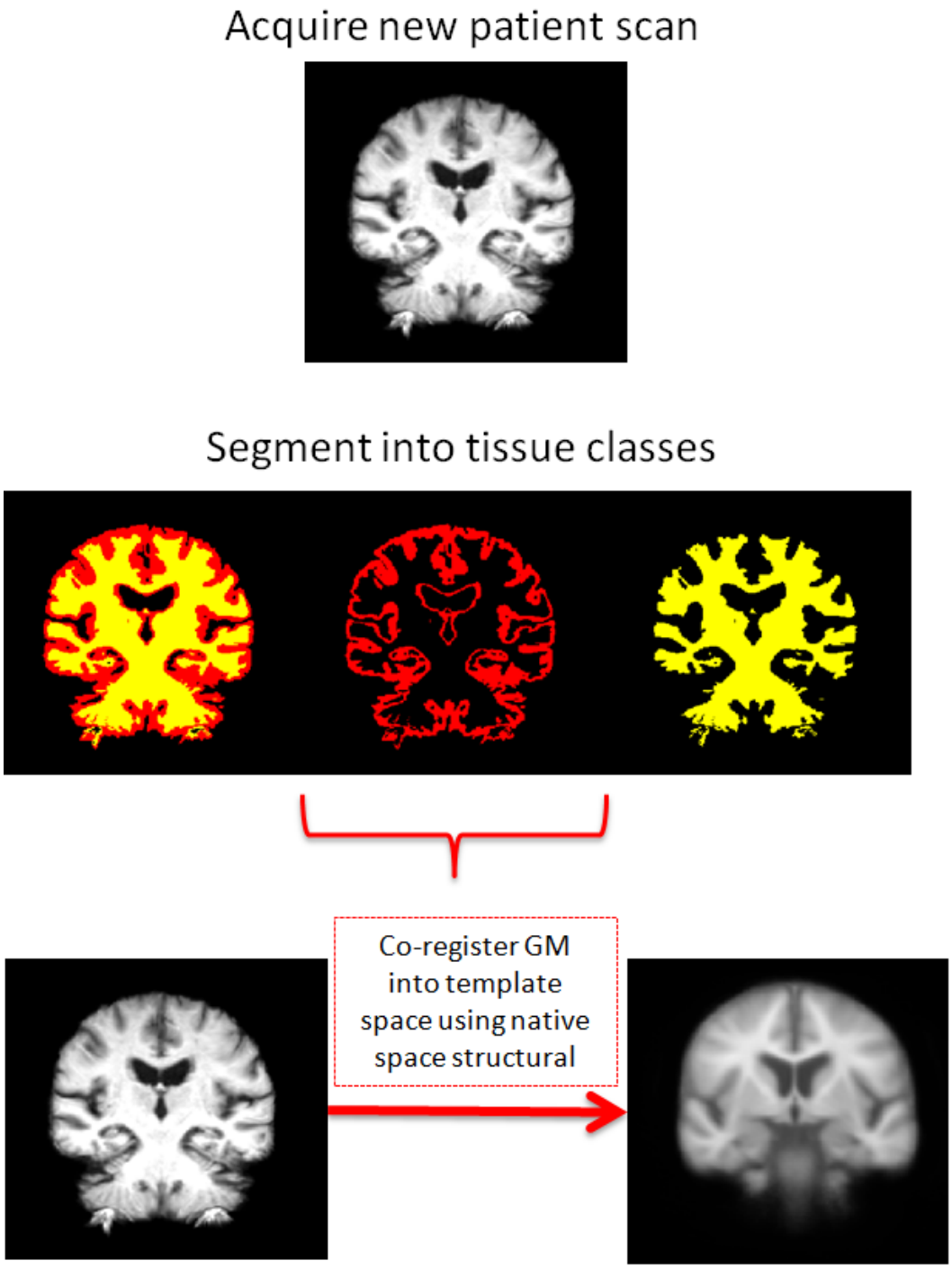

Figure 6-12: For a new patient to be analyzed, we acquire a new patient scan (isometric/isotropic structural T1 weighted image) and segment that into tissue classes. The middle panel shows the joined GM and WM tissue class segmentations joined (in red and yellow, respectively) and separated into grey and white, respectively, in the next two panes. The GM mask is then co-registered into the template space in which the statistical binarized mask. This uses the structural T1 image as the basis for transformation and applies that forward transformation to the GM mask.

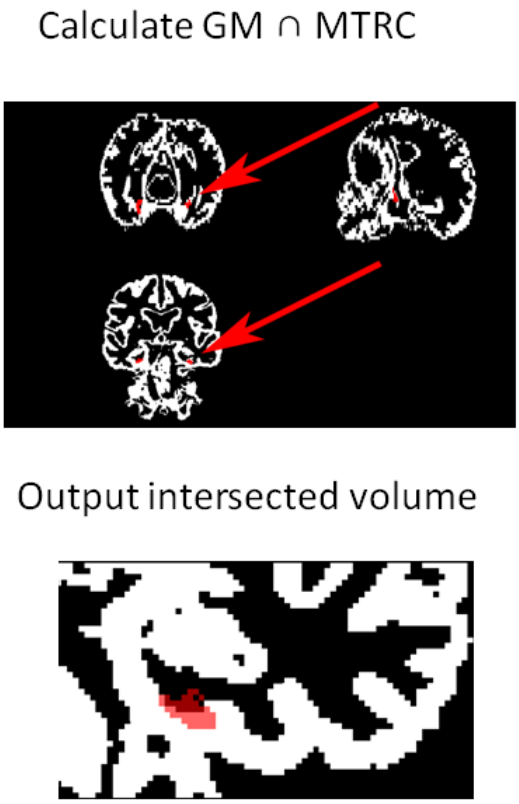

Figure 6-13: The intersection of the binarized mask and the gray matter mask is calculated. Although voxel size differences may occur, all images being in the same space indicate that all measures of volume are standardized by co-registering.

Appendix A

Supporting experimentation: Determination of vascular thresholding

A.1 Background

One of the requirements of ssCBV is the exclusion of epicortical vessels that do not directly feed arteriolar or capillary beds of cortical perfusion.[50] These large vessels may be impacted by natural variation and torturosity in patients in an MRA scan, however in ssCBV one limitation is that we assume an intact BBB as well as a normative macrocerebralvascular anatomy. However, depending on imaging modalities, all voxels or pixels are prone to representing more than one unique tissue class within a sampled space. This phenomenon is referred to as partial voluming and is an issue especially in large voxel imaging.[94, 89]

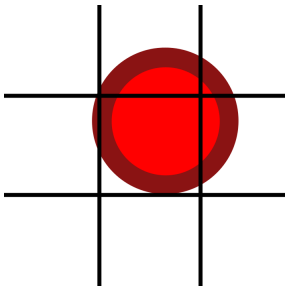

Figure A-1: This is an example of an image displaying the PV problems and window sampling limitations in both non and contrast enhanced MRI. The fraction of an isotropic pixel (or voxel) of size k will capture at most $.25\pi$ or approximately 78 percent of a 2 or 3 dimensional vessel space, assuming the path of the vessel is orthogonal to the plane of the voxel.

For voxels that are entirely within a voxel, however, one can safely exclude them from gray matter analysis. Previous methods of exclusion include a fixed cut-off of the top ten percent of gray matter vasculature.[50] However, this method assume similarly effective gray matter vessel classification, which was possible for animal studies of limited natural variation, but problematic in patient populations. Since the venous vasculature visible only through either TOF MRA or contrast-enhanced MR is not available when used as a prior for gray matter segmentation, a fixed cut-off based entirely on histogram analysis of tissue classes would not allow for any changes in the total volume of blood, dosage differences or denser vasculature.

An experiment was performed in order to adhere to the principle of large vessel exclusion while including a component that accounted for individual variation. A pre and post-contrast image pair were co-registered and a subtracted map was generated (the subtracted map is proportional to the CBV map prior to SSS blood normalization). The existing curve fitting procedure is described in Section 2.3. The following experiment expands on the feasibility and validation of this method compared to

anatomical identification, or a gold standard in venous outflow through contrast enhancement.

A.2 Methods

In order to test the accuracy of the vessel elimination 12 voxels were chosen in the subtracted image, five within an area known to contain large (diameter larger than a voxel) vessels and five firmly within the hippocampus, as visible through a subtracted CBV map. This was performed in six different age-matched patients to a trained rater blind to the exclusion mask.

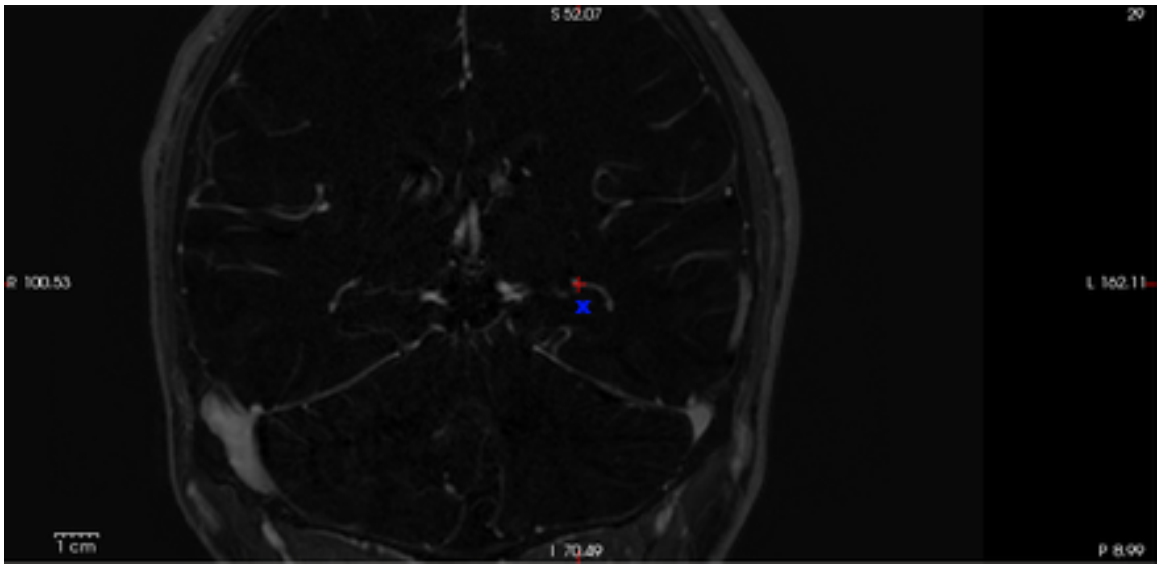

Figure A-2: Shown is a coronal slice. The left hippocampus is indicated by a blue "x" and the venous system is indicated by a red "+". Voxels were chosen in one slice near the middle of the hippocampal formation.

Several venous systems are clearly visible in the coronal (isometric) plane of the CBV acquisition parameters. These include the InfSS, SSI, ICVe and BVR. One venous outflow that is often included in the segmentation of the hippocampus is a

$$s = \frac{2\,|X_l \cap X_{nm}|}{|X_l| + |X_{nm}|} \tag{A.1}$$

Figure A-3: Here, s is the coefficient that measures overlap between manually labeled tissue, X_l and tissue preserved (not masked) during masking, X_{nm}

Table A.1: Overlap ratios for several subjects manually chosen values.

Region	DICE ($T_l \cap T_{nm}$)	DICE ($V_l \cap V_m$)
Subject 1	100%	83%
Subject 2	83%	100%
Subject 3	83%	100%
Subject 4	100%	100%
Subject 5	83%	83%
Subject 6	100%	100%
Mean	**91.5%**	**94.3%**

tributary of these systems, identifiable through high contrast differences lateral to the long axis of the hippocampus. This venous system was chosen as an area of identifiable blood, and the left hippocampus was chosen as a regional control. Voxels were chosen and characterized as either manually labeled tissue T_l, tissue not-masked (i.e. not removed by the automatic vascular filtering) T_{nm}, manually labeled vessel V_l or vessel masked V_m.

A.3 Results

Through this preliminary analysis we were able to show agreements in anatomical labeling and the aforementioned vascular exclusion criteria which is part of the CBV stream. Separately, we can also evaluate the physiological values of the mean CBV generated by looking at whole-region mean CBV values, as shown in A-4. Here we see the distribution of several subject's left hippocampus CBV values, which align with

existing literature and other CBV methods.[66, 50] Since there no gold standard for identifying epicortical blood vessels on non-enhanced structural MRI, visual identification is the closest analog to an absolute anatomic identification. Compared to this, the methods outlined performed with DICE coefficients of 91.5% for adequate segmentation and 94.5% for vessel exclusion. Since there are more voxels to contribute to the mean CBV value in the $T_l \cap T_{nm}$ regions, it is promising that this overlap was over 90%. As for the vascular segmentation, regions chosen to be clearly part of the venous tributary system abutting the hippocampus were chosen, and an even higher overlap ratio promises to exclude the bulk of this.

A.4 Conclusion

There are several limitations to this method, including variations in Gaussian models to the intensity distribution, as well as aberrant voxels of high signal located within the hippocampus (and unlikely to be non PV vascular). Future studies should address likelihood of vessels based on *a priori* atlases and morphological techniques and alternative approaches to voxel distribution voxels. However, despite these, the previously defined experiments supports the use of this method as an accurate way to sequester large epicortical vessels in ssCBV images.

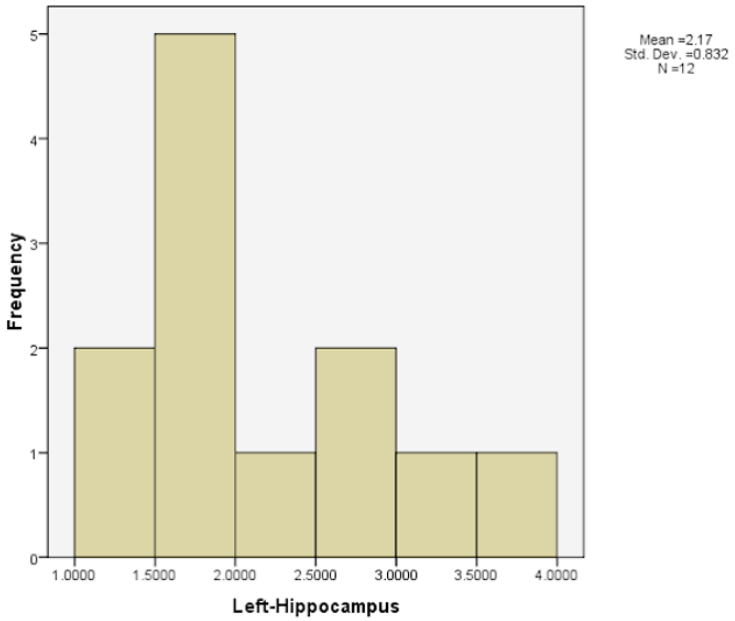

Figure A-4: Here is a histogram of 12 subject's CBV mean values. The mean and variance of these CBV values are within physiological limits, and can be used as a *post-hoc* exclusionary criteria for subjects that might have intravascular abnormalities or BBB breakage.

Appendix B

Supporting experimentation: Evaluation of SSS segmentation to manual segmentation

B.1 Methods

AIFs are known to vary greatly from GBCA perfusion study to study.[70] Some of the natural variation inherent in this technique can be attributed to scanner SNR differences and noise, physiological differences and computational limitations. Using several existing studies which had established a technique for the discovery of a mean value of 'pure blood' to be used in CBV studies, we performed an experiment to extract and isolate the SSS in subject post-contrast scans and compare that to an existing methodology.[68, 80] However, in wishing to compare this to previous studies (and evaluate differences), we must first understand the limitations of both methods,

due to the established variation in these methods.

Existing methods to identify a region of pure blood examined the top 4 voxels in a coronal slice of a post-contrast MRI image and taking the mean value of those voxels. In order to compare this mean value with the mean value generated from the segmentation technique described, we manually identified a coronal section anterior to the most superior arc of the SSS in six age-matched patients with no observable structural abnormalities.

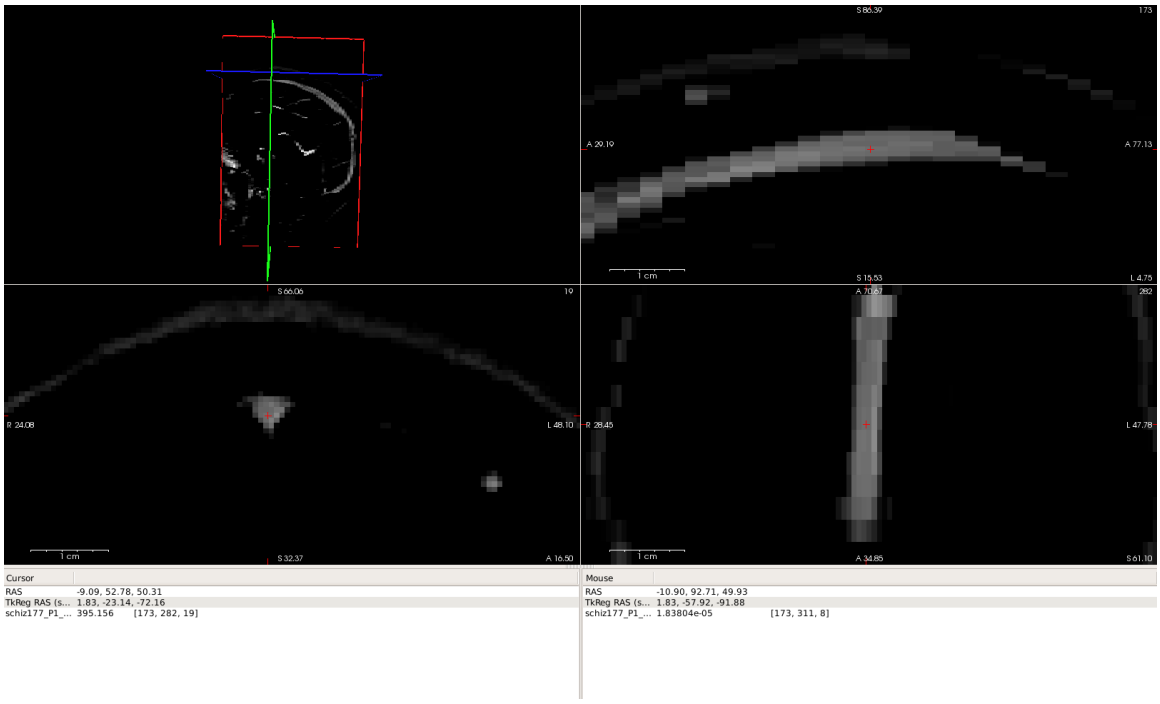

Figure B-1: This is an orthogonal section of a subtracted subject scan showing the venous structure elucidated from injection of a GBCA compared to the non-contrast image.

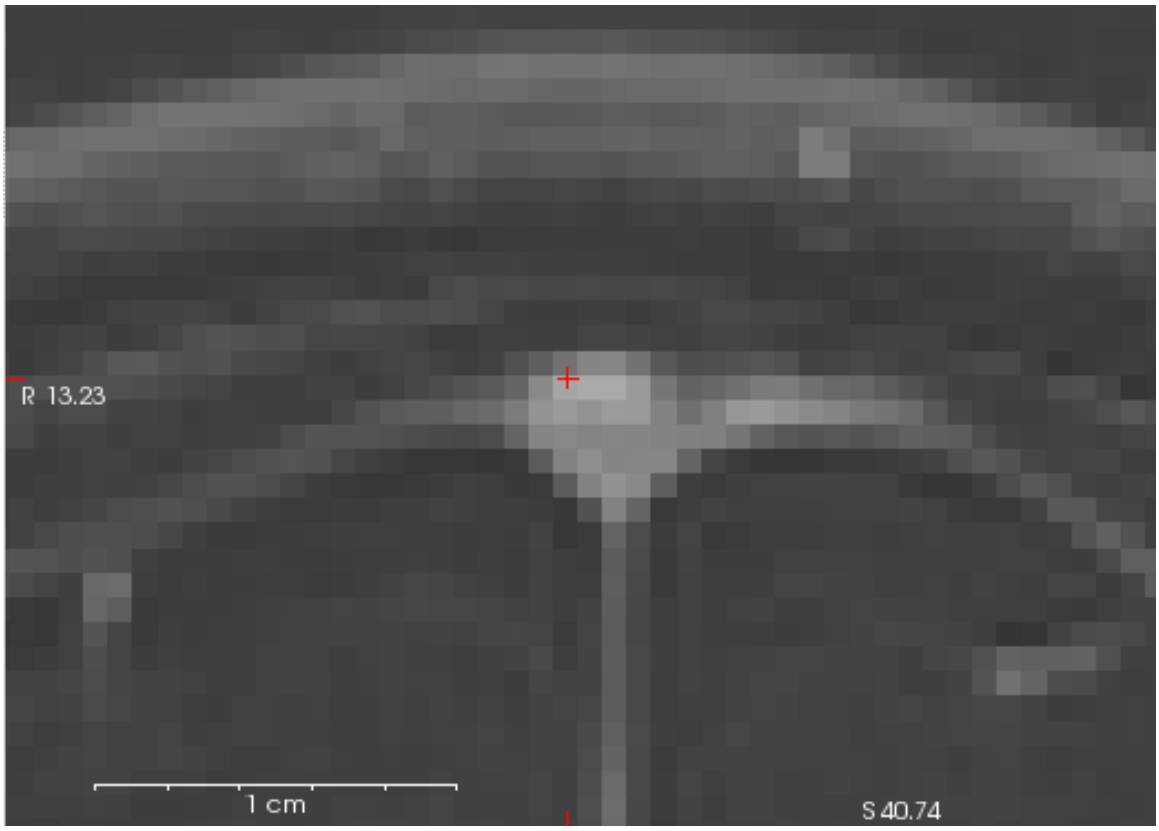

Figure B-2: This image shows a representative coronal slice onto which four voxels within the SSS have their intensities measured and the mean calculated.

B.2 Results

The results of the voxel-by-voxel statistics for this study are shown in B.1 for the six subject scans. The overal mean difference in values between the manual labeling and automated labeling was -1.11%. The units presented are arbitrary units constructed from identical signal reconstruction techniques in these images without any MRI receiver gain (in order to preserve intensity).

B.3 Conclusion

In most subjects, there was less than a 2% change between the manual method and the non-manual method. For two subjects, the expected mean value difference varied over 5%. Given that very high voxel values may not reflect pure blood value, a given slice may contain several voxels of aberrantly high intensity that may increase the variance in the signal detected. Since the SSS segmentation will almost always select a larger vessel mask, it is sampling more voxels and generating mean values from a greater n. One can see a large signal variance in subject 6, which could be indicative of the presence of non-blood voxels. Given these changes and the inherent uncertainty present with sampled voxels, this approach appears to be a fair

Table B.1: Table of individual voxel values and mean segmented voxel values

	Subject 1	Subject 2	Subject 3	Subject 4	Subject 5	Subject 6
Vessel Segmented Mean	424.234	406.927	435.902	481.851	416.891	437.849
voxel 1	425.263	417.727	445.177	503.175	379.990	424.207
voxel 2	439.023	399.897	442.57	490.567	370.071	498.692
voxel 3	406.207	388.536	431.255	478.151	372.675	497.276
voxel 4	395.156	393.245	432.031	469.707	368.416	477.101
Four Voxel Average	416.412	399.851	437.758	485.400	372.788	474.319
% Difference	**-1.89%**	-1.77%	0.424%	0.731%	-11.83%	7.68%
Mean % Difference	**-1.11%**					

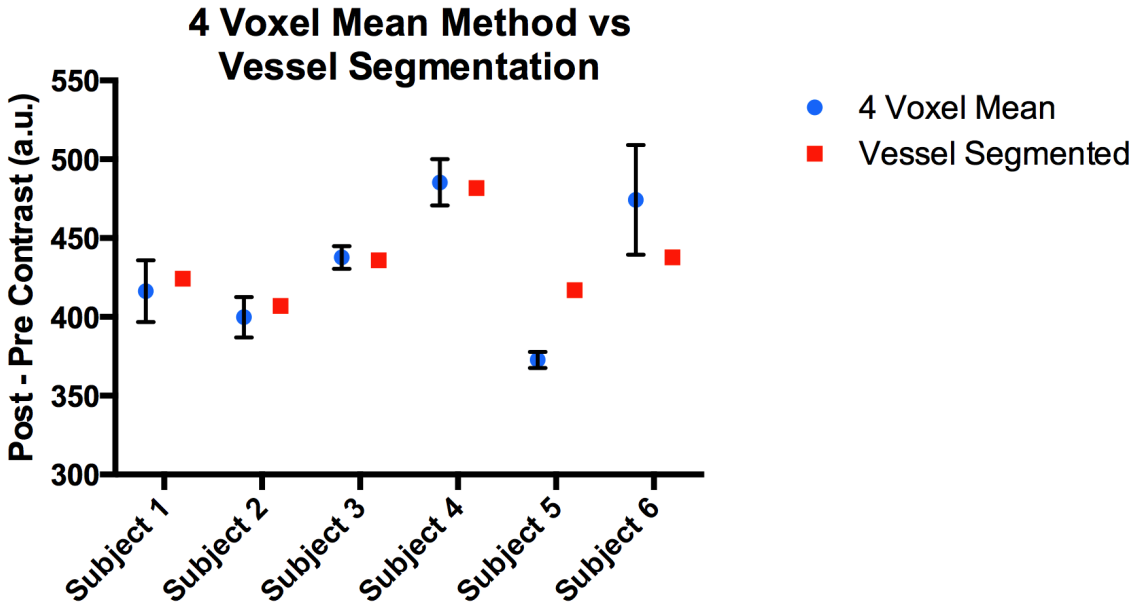

Figure B-3: Here is the distributions of voxel values from both the standard vessel extracted mean value (from the top 10% of vessel voxel values) and the mean of four independently chosen brightest voxel values in the coronal plane of an anterior slice of several images derived from subtracting pre-contrast MRI scans from post-contrast MRI scans. The ordinate is arbitrary MRI units, and the abcissa is different subjects. The mean of the four values as well as lines indicating standard deviation are reflected with blue circles, and the standard vessel extracted in red squares.